IRON ANODES FOR RECHARGEABLE ALKALINE BATTERIES

A Dissertation
Presented to
The Academic Faculty

by

Dong-Chan Lee

In Partial Fulfillment
of the Requirements for the Degree
Doctor of Philosophy in the
School of Materials Science and Engineering

Georgia Institute of Technology
May 2018

IRON ANODES FOR RECHARGEABLE ALKALINE BATTERIES

Approved by:

Dr. Gleb N. Yushin, Advisor
School of Materials Science and Engineering
Georgia Institute of Technology

Dr. Thomas F. Fuller
School of Chemical & Biomolecular Engineering
Georgia Institute of Technology

Dr. Faisal M. Alamgir
School of Materials Science and Engineering
Georgia Institute of Technology

Dr. Seung Woo Lee
School of Mechanical Engineering
Georgia Institute of Technology

Dr. Meilin Liu
School of Materials Science and Engineering
Georgia Institute of Technology

Date Approved: March 22, 2018

To the giants who offered me their shoulders

ACKNOWLEDGEMENTS

I want to first express my appreciation to Dr. Gleb Yushin, Dr. Faisal Alamgir, Dr. Meilin Liu, Dr. Thomas Fuller and Dr. Seung Woo Lee for the support, guidance and patience. I would also like to express my thanks to all the past and current group members for the shared experience. Last but not least, I would like to thank my friends for the help.

TABLE OF CONTENTS

LIST OF TABLES

LIST OF FIGURES

LIST OF SYMBOLS AND ABBREVIATIONS

C(0,t)	Concentration of Analyte at Electrode Surface
D	Diffusion Coefficient
E°	Standard Reduction Potential
t	Time
CV	Cyclic Voltammetry
EEI	Electrode/Electrolyte Interface
HER	Hydrogen Evolution Reaction
SEM	Scanning Electron Microscope
XRD	X-Ray Diffraction

SUMMARY

Rechargeable low-cost alkaline batteries may become attractive non-flammable alternatives to lithium-ion (Li-ion) batteries for applications where achieving the highest energy density is less critical than safety, environmental friendliness and low cost of energy storage. The broad abundance and extremely low price of iron (Fe) make it particularly attractive as rechargeable anode material for aqueous batteries. By conducting systematic studies on Fe anodes using cyclic voltammetry and a broad range of state of the art characterization tools, four distinct stages of Fe anode evolution were revealed: development, retention, fading and failure, where each stage is associated with very specific changes in the morphology and phase of Fe anodes. The particle fragmentation with the consequent gain in the surface area resulted in the increase in the Fe anode capacity during the initial cycles of deep charge-discharge. Most importantly, it was discovered that the irreversible formation of monocrystalline maghemite (γ-Fe_2O_3) with low reactivity is responsible for the eventual Fe anode capacity fading. Along with the base study on Fe anodes in alkaline conditions, the extended research observed how the individual factor in cell operation influences the electrochemical behavior, morphology evolution and phase transition of electrodes. A variety of components were independently adjusted: potential range, electrolyte concentration, scan rate, and additive content. The author hopes that this study will be a cornerstone for both the fundamental understanding of Fe anodes in alkaline conditions and the future development of low-cost rechargeable alkaline batteries for grid energy storage.

CHAPTER 1. INTRODUCTION

1.1 History and Motivation

Due to the pressing need to reduce pollution and combat climate change, the field of energy generation is evolving by developing systems to harvest energy from renewable sources, such as solar and wind. As their costs were reducing and implementations were expanding, a demand for large-scale energy storage systems significantly arose to store the excess energy during the electricity producing periods and release it during the electricity demanding periods. Although lithium-ion (Li-ion) batteries are now widely used due to their high energy density and efficiency, the simultaneous demands on improving cost, safety and durability aspects for the gird-scale applications present a challenge to the deployment of such systems.[1] Exploring aqueous battery systems is expected to bring the benefits of using low-cost, abundant materials and non-flammable electrolytes for cheaper battery construction.

Since nickel-iron (Ni-Fe) batteries were invented and commercialized by Waldemar Jungner and Thomas Edison in 1897 – 1902, respectively, they have been used in various stationary and mobile applications for over 70 years in the United States and Europe until the 1980s when the iron-based batteries were largely supplanted by sealed lead-acid batteries.[2] A renewed interest on them awoke due to their environmental friendliness, low cost, long life and robustness against harsh conditions as well as the compatibility with intermittent power sources such as wind power and photovoltaics.[3] Since Fe is the fourth most abundant element in the Earth's crust,[4-5] the shortage of Fe in the foreseeable future will never take place. This is also true for nickel and potassium hydroxide, raw material

for cathodes and salt for electrolytes, respectively.[6-7] Regarding the longevity of Ni-Fe batteries, it is reported that their cycle life exceeds 3000 cycles and calendar life reaches ~20 years.[8-10] In addition to these advantages, such cells also exhibit great tolerance to abuse such as overcharge, over-discharge, short-circuit and mechanical shock/vibration. The relatively high price of Ni in Ni-Fe cells may potentially be overcome by replacing the cathode with lower cost alternatives, such as air[11] or MnO_2[12] cathode among others.

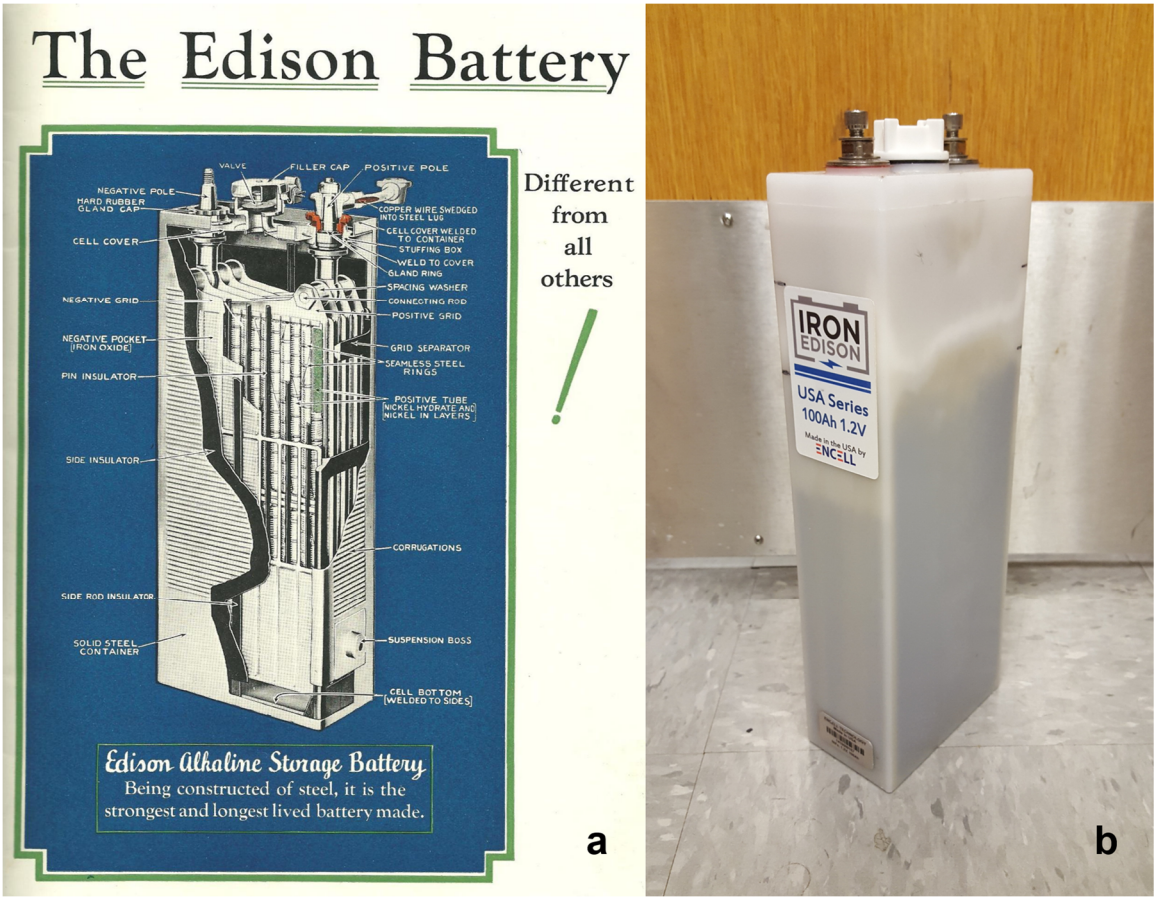

Figure 1. (a) Initial form of Ni-Fe batteries in 1920s (Edison Storage Battery Company)[13] and (b) commercial product in 2010s (Encell Technology).

1.2 Research Objectives

Additional challenges for improved rechargeable alkaline batteries, however, keep limiting their utilization for large-scale electrical grid applications: high self-discharge, poor cell efficiency, low capacity utilization and thus low energy/power densities (Figure 2).[3, 10, 14-17] Such drawbacks can be overcome by gaining a fundamental understanding on the behavior of electrode materials under cell reactions.

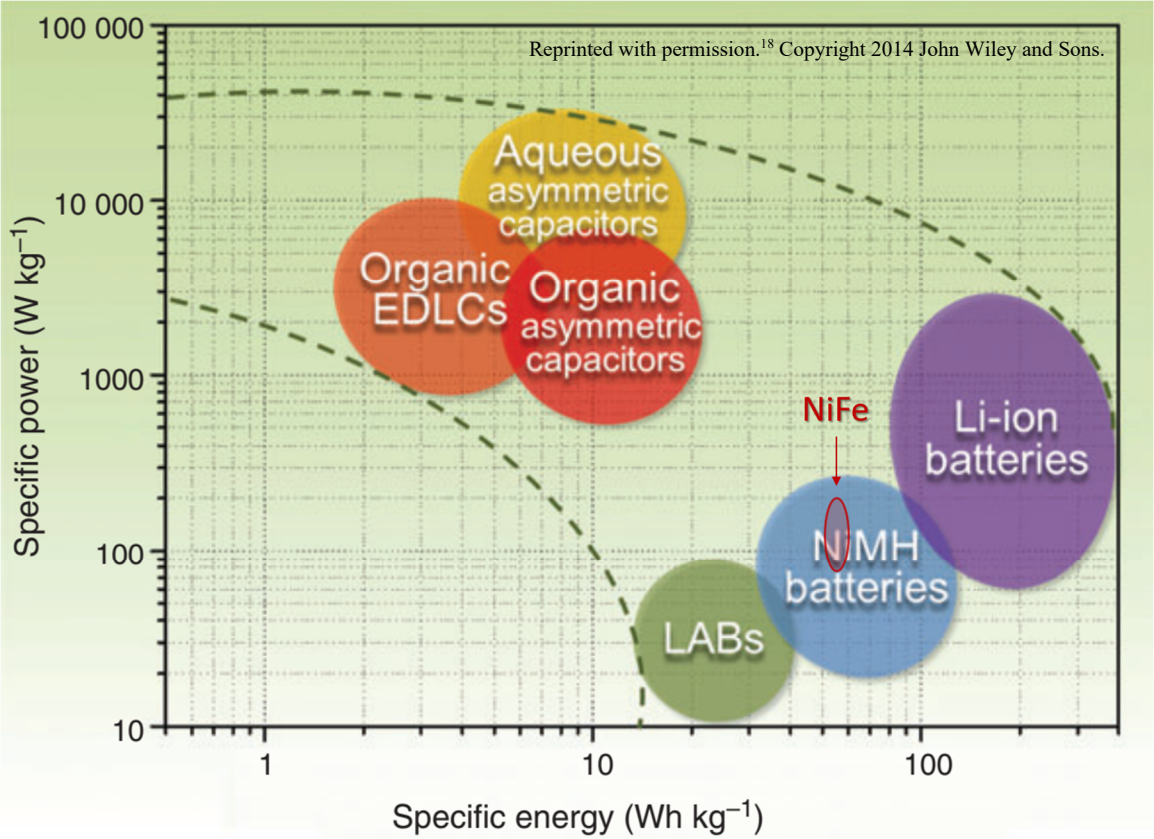

Figure 2. Ragone plot for various energy storage systems.[18] Note that LABs mean lead-acid batteries. The values for densities may have small variation by reporting groups.

Metallic Fe can electrochemically oxidize into iron hydroxide ($Fe(OH)_2$) in alkaline conditions, which is classically described as the first discharge reaction of iron anodes in Ni-Fe batteries (Reaction 1).

$$Fe + 2OH^- \leftrightarrow Fe(OH)_2 + 2e^- \qquad (E° = -0.98 \text{ V vs. Hg/HgO}) \quad (1)$$

In contrast to the above Fe-to-Fe(II) oxidation, various pathways have been suggested for the second discharge reaction of Fe anode, the Fe(II)-to-Fe(III) oxidation, which significantly contributes to the energy density of alkaline cells. Feroxyhyte (δ-FeOOH),[19-22] magnetite (Fe_3O_4)[23-25] or their mixture[26-29] was considered as the final product of the multiple reversible oxidation reactions (Reaction 2 and 3), while the direct electrochemical conversion from Fe was also proposed for both the former[15, 20, 30-31] and the latter.[32-35] Hematite (α-Fe_2O_3) was relatively recently reported to have its reversibility in alkaline condition[36-40] though the detailed electrochemistry was not revealed yet except for a thermodynamic presupposition (Reaction 4).[41]

$$Fe(OH)_2 + OH^- \leftrightarrow FeOOH + H_2O + e^- \qquad (E° = -0.65 \text{ V vs. Hg/HgO}) \quad (2)$$

$$3Fe(OH)_2 + 2OH^- \leftrightarrow Fe_3O_4 \cdot 4H_2O + 2e^- \qquad (E° = -0.76 \text{ V vs. Hg/HgO}) \quad (3)$$

$$2Fe_3O_4 + 2OH^- \leftrightarrow 3Fe_2O_3 + H_2O + 2e^- \qquad (E° = -0.70 \text{ V vs. Hg/HgO}) \quad (4)$$

The author believes that the study on phase changes in Fe anodes upon deep cycling should be accompanied by the exploration of morphology transformations to achieve complementary understanding on both physical and chemical changes in Fe anodes. Surprisingly, the research with visual characterization, such as scanning electron microscopy (SEM), is still mostly lacking. Several articles showed the microstructure

change in cycled Fe anode, but the results were either obtained under a particular condition[42-43] or quantitatively insufficient to establish any clear trends.[43-46] Although Öjefors drew the evidence for the dissolution-precipitation process of discharge from a series of SEM observation in 1976, his work lacked in some other types of critical characterizations.[19]

In order to overcome the limitations of the aforementioned studies, cyclic voltammetry (CV) was performed on Fe anodes under alkaline conditions and their electrochemical, morphological and chemical structural evolutions were systematically studied using SEM, X-ray diffraction (XRD) and Raman spectroscopy. The methodical investigation with post-mortem analysis revealed four distinct stages of Fe anode evolution: development, retention, fading and failure, where each stage is associated with very specific changes in the morphology and phase of Fe anodes. Most importantly, this study led the author to the conclusion that the irreversible formation of monocrystalline maghemite (γ-Fe_2O_3) with low reactivity was largely responsible for the Fe anode degradation. This new knowledge challenges the current understanding on the key mechanisms of Fe anode decay upon its high capacity utilization. It may open new avenues for overcoming the limitations of Fe anodes and lead to the development of enhanced low-cost Fe anodes based rechargeable alkaline batteries.

CHAPTER 2. THEORETICAL BACKGROUND

2.1 Electrochemistry of Iron Anodes in Nickel-Iron Batteries

The charge-discharge reactions of negative electrodes (Fe anodes) occur in two steps under the alkaline electrolyte conditions (Figure 3)[9, 31, 47] usually achieved by high molarity of potassium hydroxides in aqueous solution.

$$Fe + 2OH^- \leftrightarrow Fe(OH)_2 + 2e^- \qquad (E° = -0.98 \text{ V vs. Hg/HgO}) \quad (1)$$

$$Fe(OH)_2 + OH^- \leftrightarrow FeOOH + H_2O + e^- \qquad (E° = -0.65 \text{ V vs. Hg/HgO}) \quad (2)$$

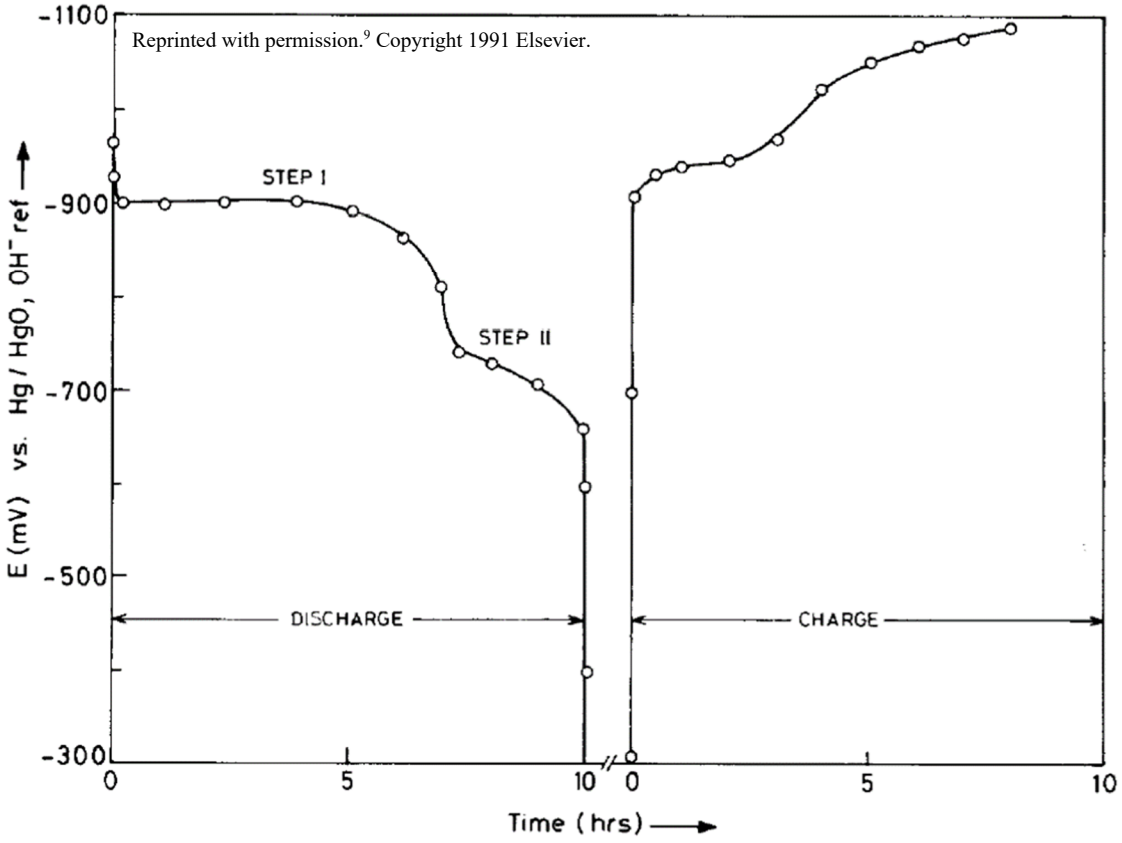

Figure 3. Typical charge-discharge potential curves of Fe anodes in Ni-Fe batteries.[9]

The detailed mechanism of Reaction 1 involves both solid and liquid phases (i.e., heterogeneous mechanism) with a soluble ferrite intermediate ($HFeO_2^-$) which converts to $Fe(OH)_2$ on further discharge.

$$Fe + 3OH^- \leftrightarrow HFeO_2^- + H_2O + 2e^- \quad (1\text{-}1)$$

$$HFeO_2^- + H_2O \leftrightarrow Fe(OH)_2 + OH^- \quad (1\text{-}2)$$

The first oxidation reaction (Fe to Fe(II) in Reaction 1) has more significance for practical cell operation than the second oxidation reaction (Fe(II) to Fe(III) in Reaction 2). This is because i) corresponding lower cell voltage makes the second reaction less attractive in terms of usable energy density and, more importantly, ii) the former reaction is highly reversible in alkaline electrolytes while the latter one does not accept charge readily.[10] Many articles have represented the theoretical specific capacity of Fe anodes as 962 mAh/g, which is based on the first charge-discharge reaction (Reaction 1) only.

The studies on kinetic behavior of Fe anodes have provided the evidence in favor of a dissolution-precipitation mechanism.[19, 30-31, 33, 48] During the prolonged discharge, Fe anodes have a diffusion of protons between the solid lattices of $Fe(OH)_2$ and δ-FeOOH, resulting in a continuous composition change from $Fe(OH)_2$ to δ-FeOOH which can be considered as a homogeneous reaction.[8, 21]

On the other hand, the charge-discharge reactions of positive electrodes (Ni cathodes) are accompanied by the redox reactions between nickel oxyhydroxides and nickel hydroxides.

$$NiOOH + H_2O + e^- \leftrightarrow Ni(OH)_2 + OH^- \qquad (E° = 0.39 \text{ V vs. Hg/HgO}) \quad (5)$$

Therefore, the overall charge-discharge reactions for full cells have two voltage plateaus if their cycling includes deep-discharge.

$$2NiOOH + Fe + 2H_2O \leftrightarrow 2Ni(OH)_2 + Fe(OH)_2 \qquad (E_{cell}° = 1.37\ V) \qquad (6)$$

$$NiOOH + Fe(OH)_2 \leftrightarrow Ni(OH)_2 + FeOOH \qquad (E_{cell}° = 1.05\ V) \qquad (7)$$

The characteristics of Ni-Fe batteries are presented in Table 1 and Figure 4, which are usually manifested under the desired operating conditions: avoiding deep-discharge, cycling at room temperature, and adding water regularly.

Table 1. Cell characteristics of Ni-Fe batteries

Nickel-Iron Batteries	
Working Voltage	1.0 – 1.2 V [10]
Energy Density	50 – 60 Wh/kg [9]
Power Density	75 – 110 W/kg [9]
Coulombic Efficiency	50 – 60% [3, 14]
Cycle Life	> 3000 [8-10]
Calendar Life	15 – 20 years [10]

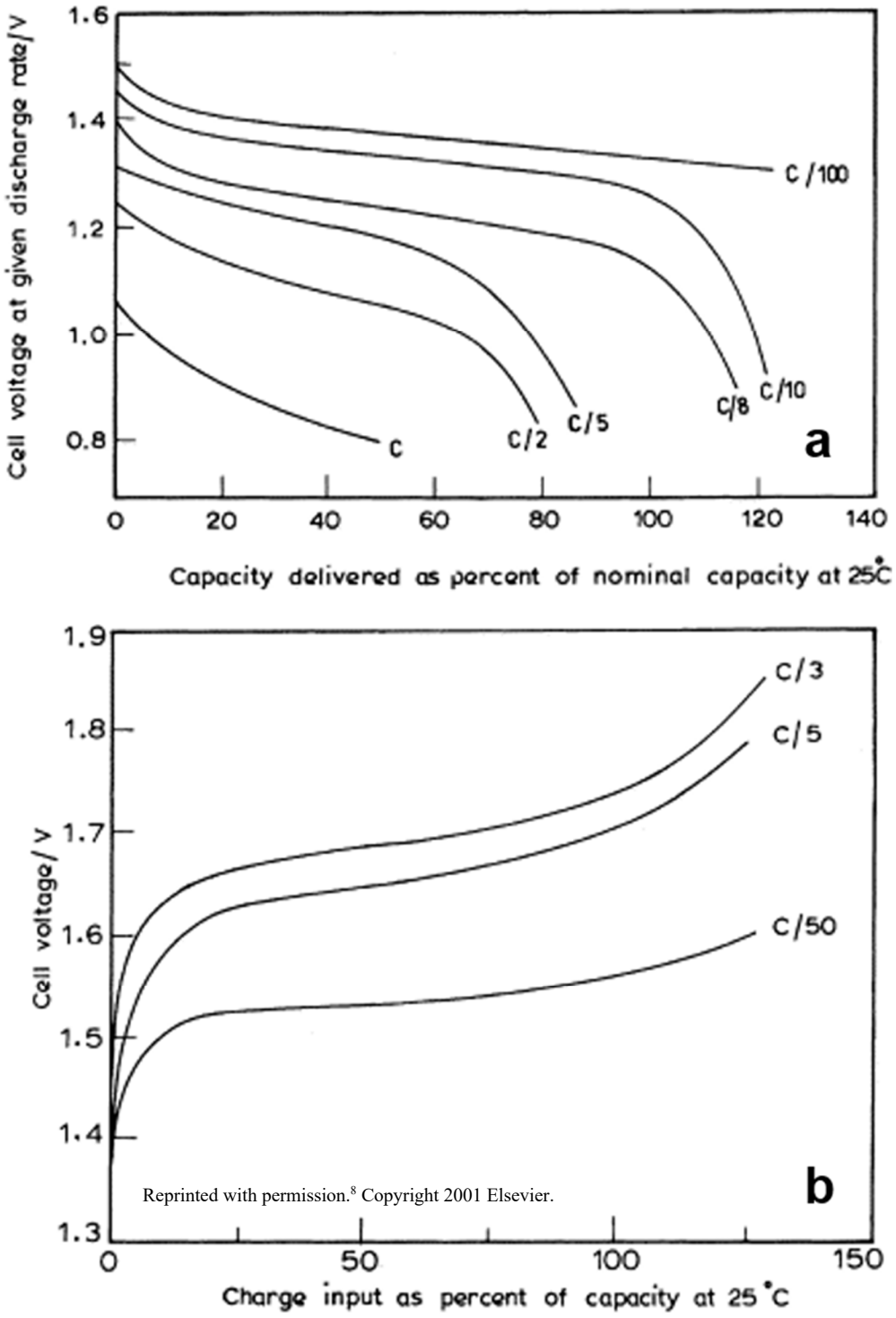

Figure 4. Voltage curves for Ni-Fe batteries upon (a) discharge and (b) charge at various current densities.[8] Note that C-rates are based on the nominal capacity of cells rather than theoretical capacity.

2.2 Hydrogen Evolution Reaction (HER)

$Fe(OH)_2 + 2e^- \leftrightarrow Fe + 2OH^-$ ($E° = -0.98$ V vs. Hg/HgO) (1)

$2H_2O + 2e^- \rightarrow H_2 + 2OH^-$ ($E° = -0.93$ V vs. Hg/HgO) (8)

Since the standard reduction potential of hydrogen in alkaline solution is close to (and more positive than) that of iron, hydrogen evolution reaction (HER) is competitive against the charging reaction of Fe anodes and thermodynamically inevitable during charge. Indeed, HER is a parasitic side reaction bringing the following negative effects on cell cycling:

i) Consume a certain amount of electrical charge from charging current, making charging efficiency low.

ii) Accumulate hydrogen bubbles on anode surface, inducing higher polarization.

iii) Cause rapid loss of electrolytes, necessitating a frequent addition of water.

Consequently, 30 – 45% of electrical energy is unrecoverable and wasted.[9, 49-52] Moreover, batteries have to be overcharged by 60 – 100% to achieve full capacity.[2] Increasing the overpotential of HER, however, can help kinetically resolve such problem. When the overpotential of hydrogen evolution is much higher than that of iron anode reduction (i.e., negatively higher reduction potential), the rate of HER can be significantly reduced at the charging potential of anodes. Several additives in either electrodes or electrolytes have i) the components whose HER overpotential is inherently high and/or ii) those which help increase HER overpotential by modifying iron surface. The type and effect of additives will be discussed in detail in another section.

2.3 Self-Discharge

HER also occurs as a participant in the corrosion of iron when cells lie idle. The open-circuit potential of charged Fe anodes is always more cathodic than the potential of hydrogen evolution in the same solution. In consequence of its low HER overpotential, thermodynamically unstable iron suffers corrosion (oxidation) which is conjugated with HER as counterpart (reduction).

$$Fe + 2OH^- \leftrightarrow Fe(OH)_2 + 2e^- \qquad (E° = -0.98 \text{ V vs. Hg/HgO}) \qquad (1)$$

$$2H_2O + 2e^- \rightarrow H_2 + 2OH^- \qquad (E° = -0.93 \text{ V vs. Hg/HgO}) \qquad (8)$$

$$Fe + 2H_2O \rightarrow Fe(OH)_2 + H_2 \qquad (1) + (8) \qquad (9)$$

On the other hand, corrosion can also be combined with oxygen reduction by either of dissolved oxygen in alkaline media or produced one from overcharged cathodes.

$$O_2 + 2H_2O + 4e^- \rightarrow 4OH^- \qquad (E° = 0.29 \text{ V vs. Hg/HgO}) \qquad (10)$$

$$2Fe + 2H_2O + O_2 \rightarrow 2Fe(OH)_2 \qquad (1) + (10) \qquad (11)$$

Owing to the above corrosion reactions, Fe anodes undergo self-discharge losing approximately 1 – 2% of their nominal capacity per day at room temperature. When operating temperature increases to 40°C, the capacity loss caused by self-discharge becomes formidable, 8 – 10% per day (Figure 5).[8]

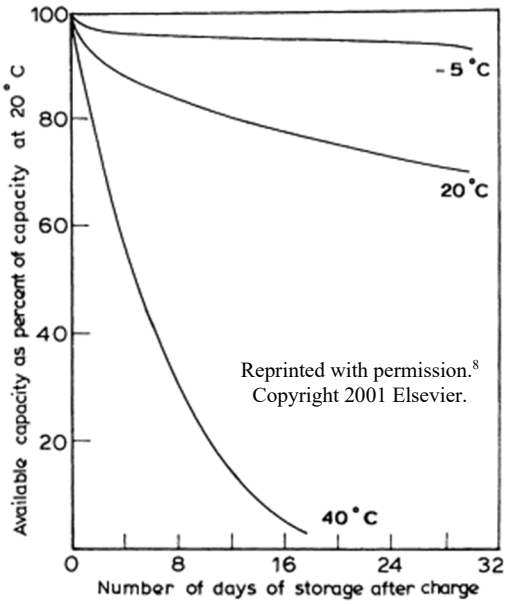

Figure 5. Self-discharge of Ni-Fe cells as function of temperature.[8]

2.4 Available Reactions for Iron Anodes in Alkaline Conditions

Although FeOOH was described as a product of the second oxidation reaction of Fe anodes (Reaction 2 in Chapter 2.1), the final product phase of this Fe(II)-to-Fe(III) oxidation is not easily identifiable. In contrast to the first oxidation reaction of Fe anodes (Fe-to-Fe(II) transition), a broad range of the reaction pathways and product phases have been proposed or claimed for the Fe(II)-to-Fe(III) oxidation over the last 50 years of study on Ni-Fe batteries.[15, 19-35] Based on the prior art studies, feroxyhyte (δ-FeOOH),[19-22] magnetite (Fe_3O_4)[23-25] or their mixture[26-29] can be considered as the final product of the Fe(II)-to-Fe(III) oxidation.

A further oxidation of $Fe(OH)_2$, the product of the first oxidation reaction of Fe anodes, forms Fe_3O_4 via electrochemical route.

$$3Fe(OH)_2 + 2OH^- \leftrightarrow Fe_3O_4 \cdot 4H_2O + 2e^- \qquad (E° = -0.76 \text{ V vs. Hg/HgO}) \quad (3)$$

Since the stability region of $Fe(OH)_2$ is well within that of Fe_3O_4 in Pourbaix diagram of iron (Figure 6), thermodynamically unstable $Fe(OH)_2$, when compared to magnetite, can transform into Fe_3O_4 with a conjugated HER like the corrosion of iron in Chapter 2.3.

$$2H_2O + 2e^- \rightarrow H_2 + 2OH^- \qquad (E° = -0.93 \text{ V vs. Hg/HgO}) \quad (8)$$

$$3Fe(OH)_2 \rightarrow Fe_3O_4 + 2H_2O + H_2 \qquad (3) + (8) \qquad (12)$$

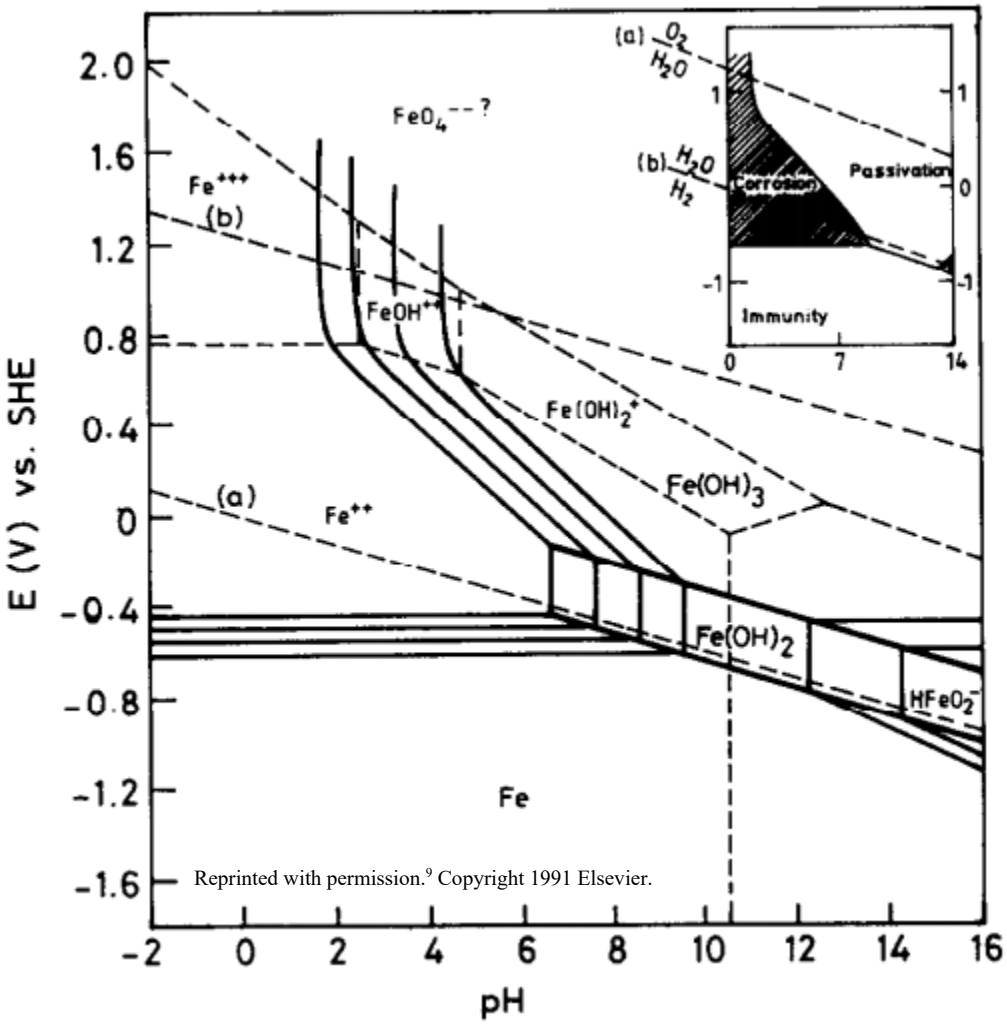

Reprinted with permission.[9] Copyright 1991 Elsevier.

Figure 6. Pourbaix diagram for Fe/H_2O system.[9]

Metallic Fe can also undergo a direct electrochemical conversion into Fe_3O_4 near the potential region of the Fe-to-Fe(II) transition (Reaction 13)[30, 32-34] with a simultaneous oxidation into the main product, $Fe(OH)_2$ (Reaction 1). Similarly, a direct oxidation of Fe into FeOOH was briefly mentioned in a few articles.[20, 35]

$$3Fe + 8OH^- \leftrightarrow Fe_3O_4 + 4H_2O + 8e^- \qquad (E° = -1.01 \text{ V vs. Hg/HgO}) \quad (13)$$

By voltammetric studies and X-ray diffraction analysis on Fe anodes in alkaline media, the details of Fe_3O_4 evolution was revealed that the oxidation of iron involves the formation of soluble ferrate (FeO_2^-) intermediates of which precursor is ferrite ($HFeO_2^-$).[10]

$$Fe + 3OH^- \leftrightarrow HFeO_2^- + H_2O + 2e^- \quad (1\text{-}1)$$

$$HFeO_2^- + OH^- \leftrightarrow FeO_2^- + H_2O + e^- \quad (14)$$

$$2FeO_2^- + HFeO_2^- + H_2O \leftrightarrow Fe_3O_4 + 3(OH)^- \quad (15)$$

Through a calculation based on the standard Gibbs free energy, the combination reactions of different iron compounds were proposed for possible routes of Fe_3O_4 formation rather than electrochemical reactions.[28, 32, 50]

$$Fe(OH)_2 + 2FeOOH \rightarrow Fe_3O_4 + 2H_2O \qquad (\Delta G° = -74.9 \text{ kJ}) \quad (16)$$

$$Fe + 8FeOOH \rightarrow 3Fe_3O_4 + 4H_2O \qquad (\Delta G° = -271.4 \text{ kJ}) \quad (17)$$

Such a calculation demonstrated that $Fe(OH)_2$ or $HFeO_2^-$ can be a precursor for the formation of Fe_3O_4 when coupled with the oxygen in electrolytes. As discussed in Chapter 2.3, it is either the dissolved oxygen in alkaline solution or the produced one from overcharged cathodes (oxygen evolution reaction, OER). Since Reaction 19 can take place

in electrolyte bulk, Fe_3O_4 may be deposited on the surface of separator and/or the inside of cell container.[32]

$$6Fe(OH)_2 + O_2 \rightarrow 2Fe_3O_4 + 6H_2O \qquad (\Delta G° = -275.0\ kJ) \qquad (18)$$

$$6HFeO_2^- + O_2 \rightarrow 2Fe_3O_4 + 6OH^- \qquad (\Delta G° = -348.8\ kJ) \qquad (19)$$

As a stoichiometric oxide for Fe(III), hematite (α-Fe_2O_3) was relatively recently reported to have its reversibility in alkaline condition[36-40] though the detailed electrochemistry was not revealed yet except for a thermodynamic presupposition.[41]

$$2Fe_3O_4 + 2OH^- \leftrightarrow 3Fe_2O_3 + H_2O + 2e^- \qquad (E° = -0.70\ V\ vs.\ Hg/HgO) \qquad (4)$$

Figure 7 summarizes all the aforementioned reaction pathways for Fe anodes in alkaline condition. It is noticeable that most of species are highly intertwined with each other acting as reactants, products or both.

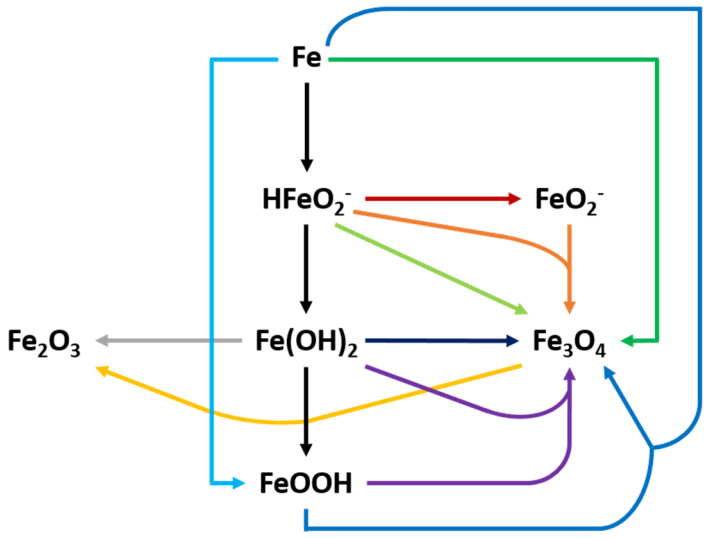

Figure 7. Available reaction pathways for Fe anodes in alkaline conditions. Note that the direction of arrows follows oxidation (discharge).

2.5 Additives

The major purpose of additives is to enhance electrochemical performance of batteries by bringing benefit to charge-discharge processes and/or restraining harmful side reactions such as HER and passivation. Various classes of materials have been studied so far for use as additives in either electrodes or electrolytes: Cu, Hg, S,[10, 15] Se, $Ni(OH)_2$, $Co(OH)_2$,[10] FeS,[51, 53-58] Bi_2O_3,[55-56] Na_2S,[22, 37, 46, 56] K_2S,[54, 57-60] PbS,[16] Bi_2S_3,[2, 46, 55-60] organo-sulfur species,[1, 61] etc. As for the forepart of examples, Cu and Hg were generally used to increase the HER overpotential, S and Se were added to reduce the ionization potential, and $Ni(OH)_2$ and $Co(OH)_2$ were known to reduce the charge-discharge overpotential.[10] While such traditional attempts subsided, comprehensive and continuous studies on sulfide materials made them the most popular and reliable additives for Ni-Fe batteries. Although there is no full consent, they have been known to improve the performance of Fe anodes through one of the following effects (Adapted with permission.[37] Copyright 2016 American Chemical Society.)

i) The adsorption of S^{2-} ions on the iron surface suppresses HER by preventing that of hydrogen atoms.[62-65]

ii) The reaction of S^{2-} ions with iron oxides produces iron sulfides that have high electronic conductivity.[46, 50-51, 55-56]

iii) S^{2-} ions dissolve a thin layer of iron oxides/hydroxides delaying the onset of iron passivation.[46, 66]

iv) S^{2-} ions are incorporated into the bulk of iron oxides causing structural deficiency and higher ionic conductivity.[53, 67]

For the additive in electrolytes, Na_2S or K_2S can be a good choice considering their solubility and harmlessness of cations in/for alkaline electrolytes. Manohar et al. reported that Na_2S increased the critical passivation current density of electrodes[46] (the third effect above) so that it helped a recovery of faded capacity[56] (Figure 8). It is interesting that K_2S only worked as an additive in electrolytes[54, 57, 60] but not in electrodes.[58-59]

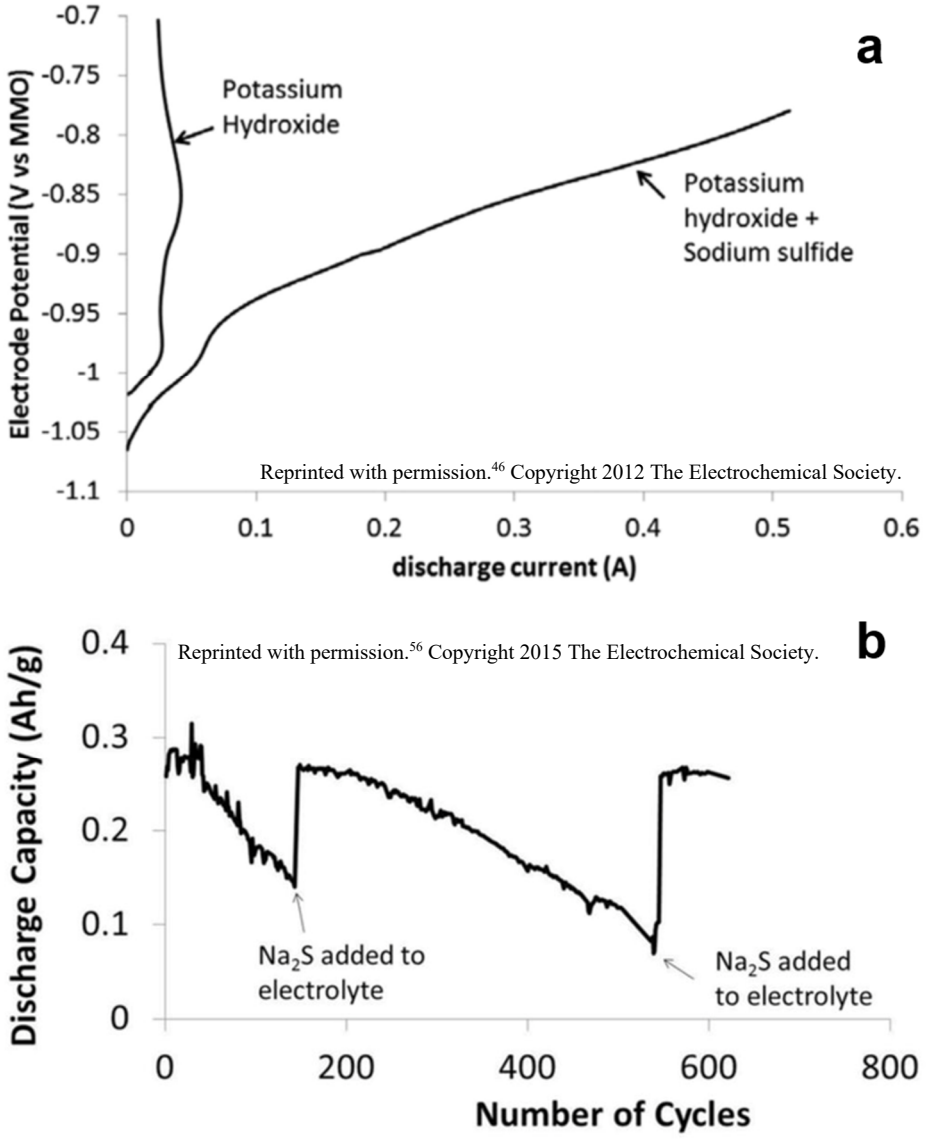

Figure 8. Effect of Na_2S on (a) anodic polarization behavior[46] and (b) capacity recovery of Fe anodes.[56]

Regarding the additives in electrodes, Bi_2S_3 can be considered as the best one among various metal sulfides because it is electrically conductive and, more importantly, bismuth has much lower hydrogen evolution reactivity (i.e., much higher HER overpotential) than iron (Figure 9). Such a property of Bi (or the group it belongs to) originates from unfavorable energetics for the electro-sorption of surface-bonded hydrogen intermediates.[68]

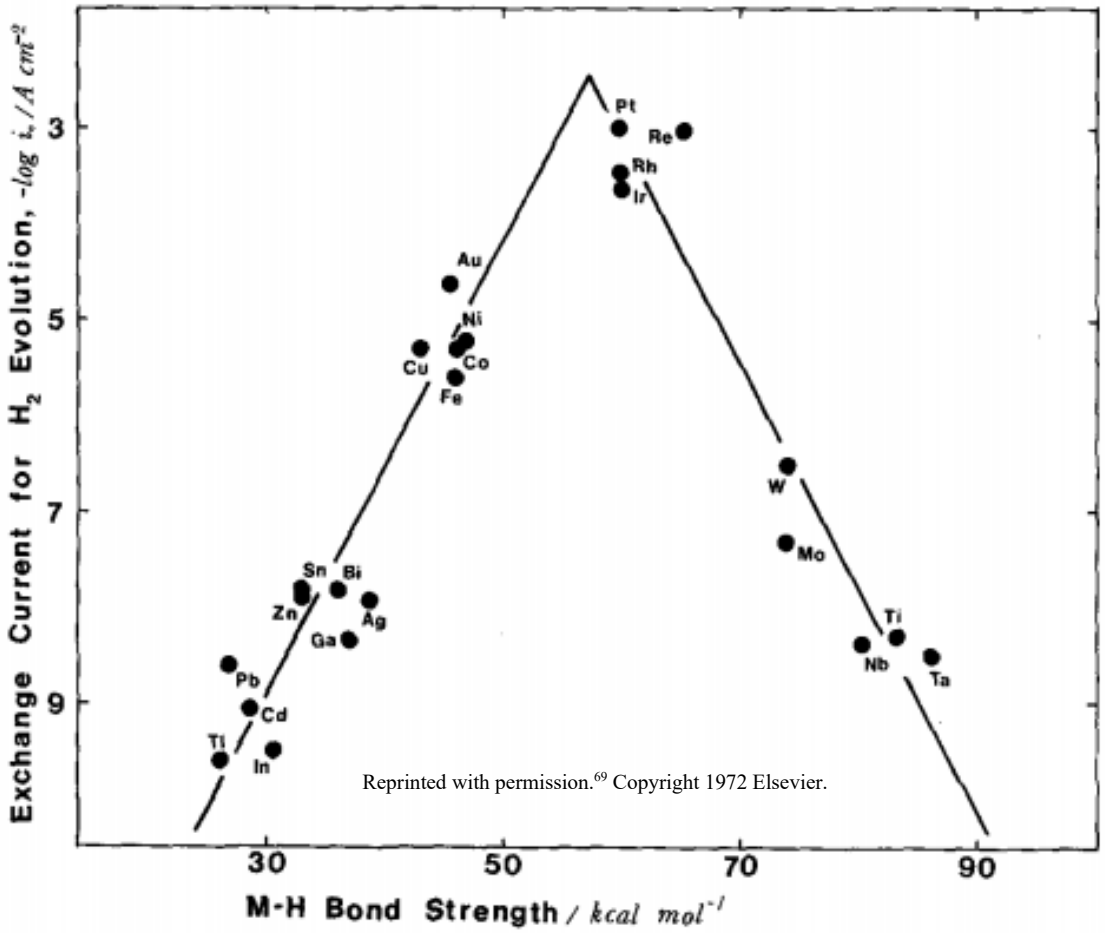

Figure 9. Volcano plot: exchange current density of metals for HER.[69]

Manohar et al. showed that Bi_2S_3 helped enhance cell performance by ten-fold reduction in hydrogen evolution rate (Figure 10a,b,c). Along with positive effect from

sulfides, they suggested that such enhancement is due to in situ electrodeposition of elemental bismuth on electrodes during cycling (Figure 10d) by the following reaction:[2]

$$Bi_2S_3 + 6e^- \leftrightarrow 2Bi + 3S^{2-} \qquad (E° = -0.92 \text{ V vs. Hg/HgO}) \quad (20)$$

Posada et al., however, did not give credit for elemental Bi by comparing the performance of Bi-containing electrode to that of Bi_2S_3-containing one. One can deduce that the effect of sulfides has higher impact than its coupled metal cations as the components of additive.[58-59]

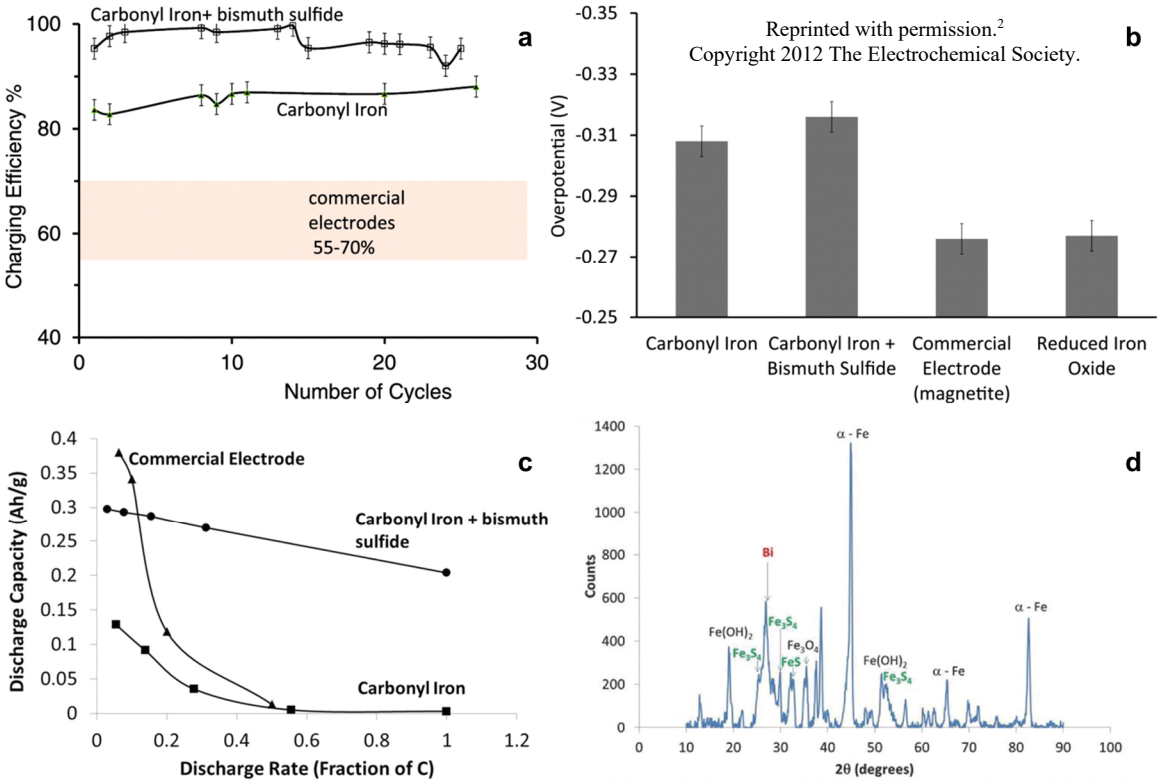

Figure 10. Bi_2S_3-containing Fe anodes: (a) charging efficiency, (b) HER overpotential, (c) discharge capacity as function of discharge rate, and (d) XRD patterns of cycled electrode.[2] Note that discharge rate in panel c was based on nominal capacity.

Later, Manohar et al. proposed FeS + Bi_2O_3 couple as improved additives enabling the sustainable supply of sulfides to Fe anodes.[55] They claimed that it prevents the accumulation of magnetite which results in eventual loss of electrode capacity (Figure 11).[56] In addition, they (Malkhandi and Yang et al. in the same group) demonstrated the positive effect of organo-sulfur additives, such as thiols and thioethers, contributing to the reduction of hydrogen evolution (Figure 12).[61] Figure 13 implies that the effect of some species closely reached that of bismuth sulfides.[1]

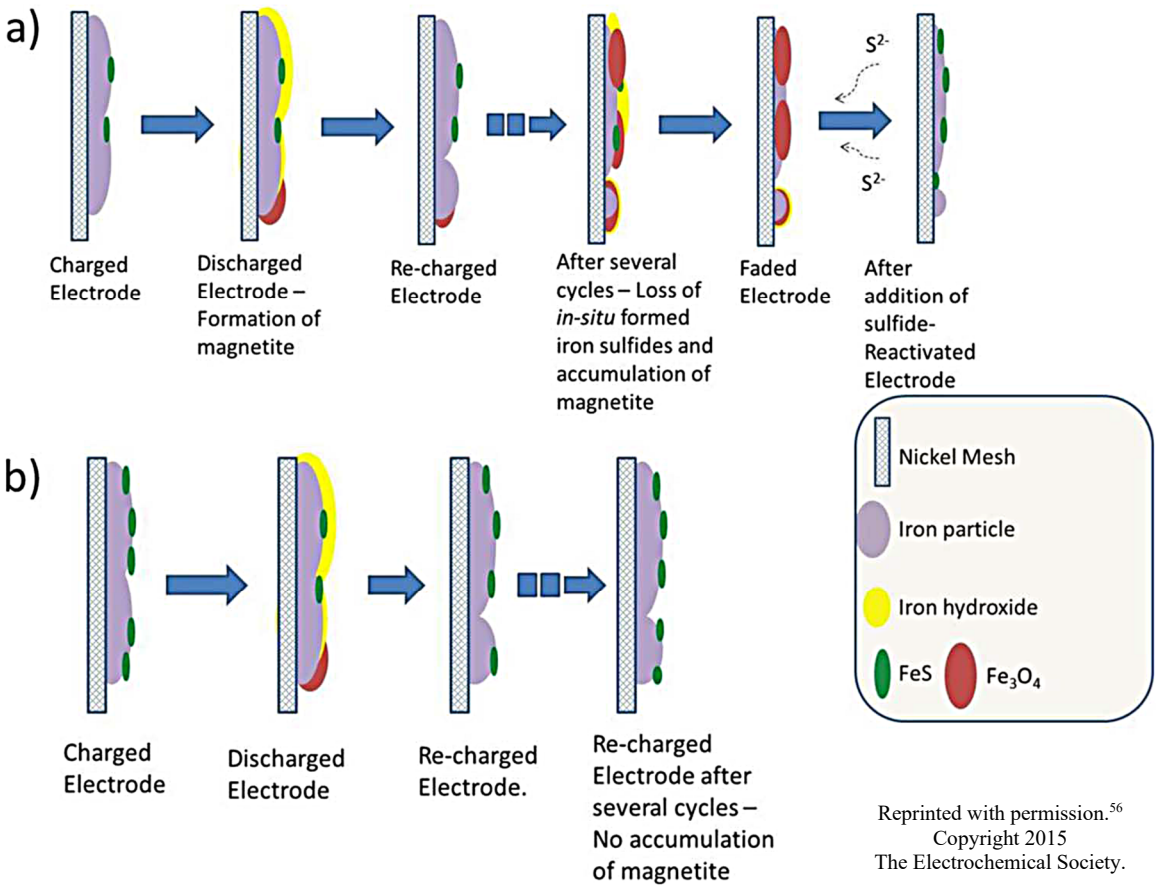

Figure 11. Schematic of Fe anode evolution with (a) Bi_2S_3 and (b) FeS + Bi_2O_3 additives upon cycling.[56]

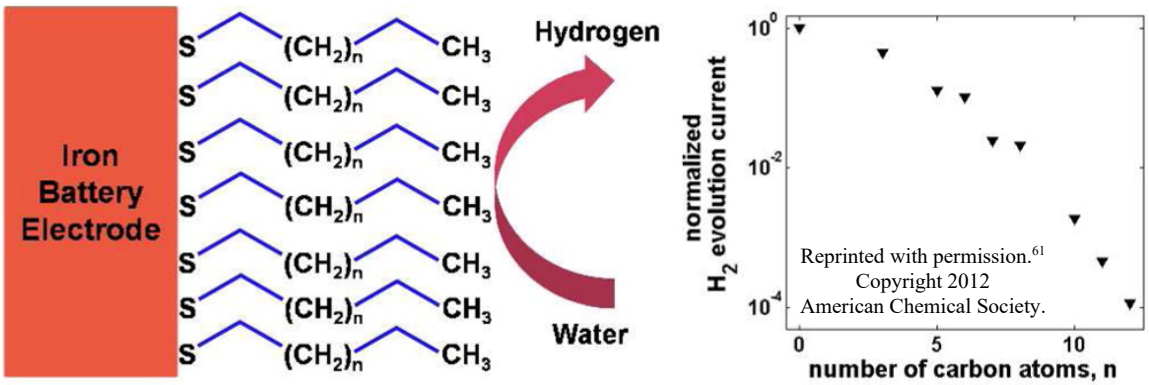

Figure 12. Schematic of self-assembled monolayer of alkanethiols on Fe anodes and its suppressing effect on hydrogen evolution as function of chain length.[61]

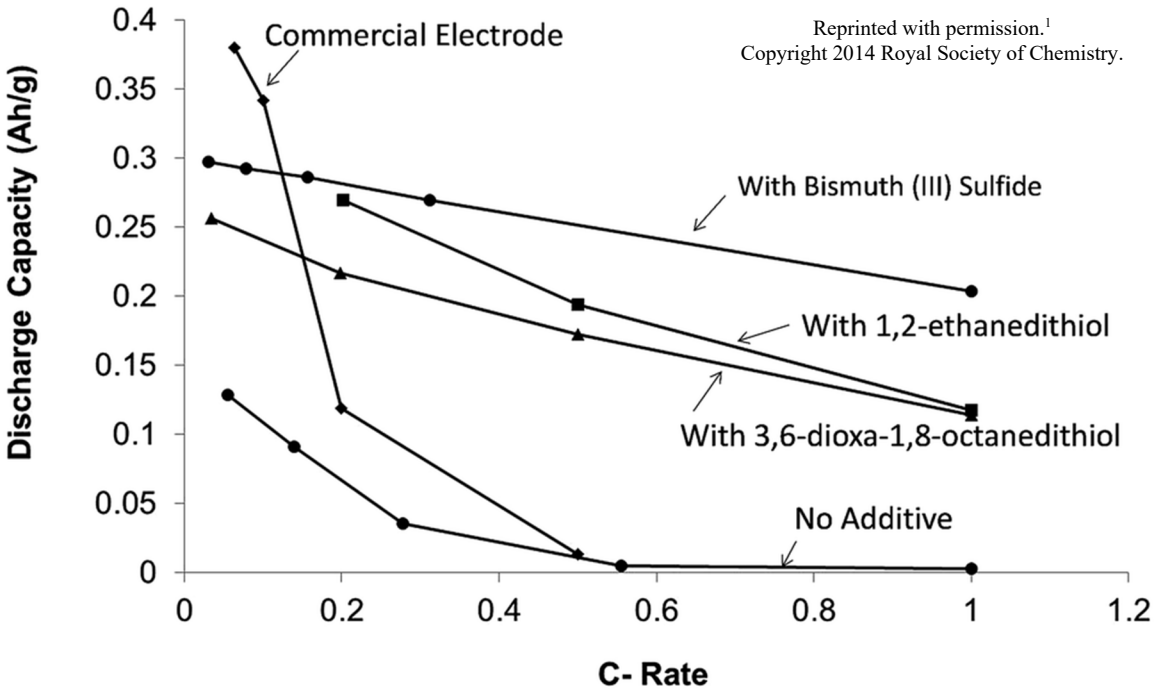

Figure 13. Effect of organo-sulfur additives on discharge capacity of Fe anodes as function of discharge rate.[1] Note that discharge rate was based on nominal capacity.

Some additives play different roles from the aforementioned species. Pore-formers provide electrodes enough porosity to improve capacity utilization and high-rate performance. Several non-sulfide additives were introduced as suitable pore-makers: PhCOONa, NaCl,[10] $(NH_4)_2CO_3$[53] and K_2CO_3.[58] These compounds are either dissolved into water or decomposed by heat-treatment. Triton X-100 once used as a wetting agent to reduce the hydrophobicity of electrode surface[46] and PbS was reported to resolve the self-discharge of Ni-Fe cells.[16]

2.6 Electrode Design

Traditional electrodes for Ni-Fe batteries had pocket or tubular shape which was first introduced by Edison. A mixture of iron and iron oxide powder was blended with additional agents and put into pockets or tubes which were made from perforated steel sheet plated with nickel (Figure 14).

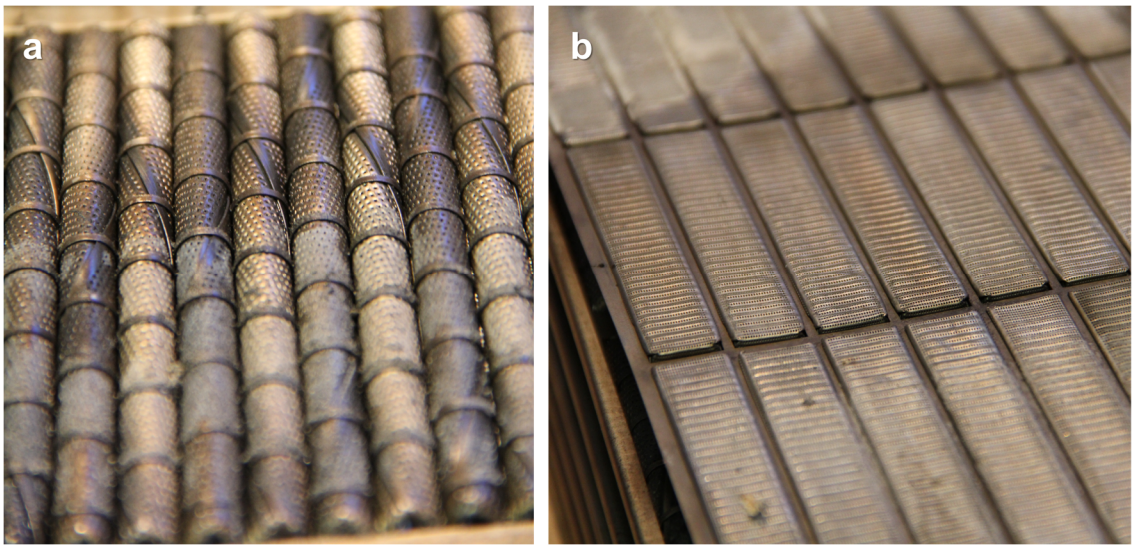

Figure 14. (a) Tubular and (b) pocket shape of electrodes for Ni-Fe batteries.[13]

While showing better performance than pocket or tubular electrodes, pressed or roll-compacted ones have a polymeric binder such as polytetrafluoroethylene (PTFE) or polyethylene (PE). Active materials are blended with binder, conducting agent and additives. The resulting mixture, or paste, is pressed into a plate/film with desired thickness by hydraulic press or rolling mill; it may require simultaneous heating. Various forms of current collectors such as plate, mesh and foam can be pressed together with electrode materials, if necessary. To provide enough porosity to electrodes, additives may include a pore-former such as sodium benzoates or potassium carbonates which are leached out by boiling water or heat treatment, respectively.

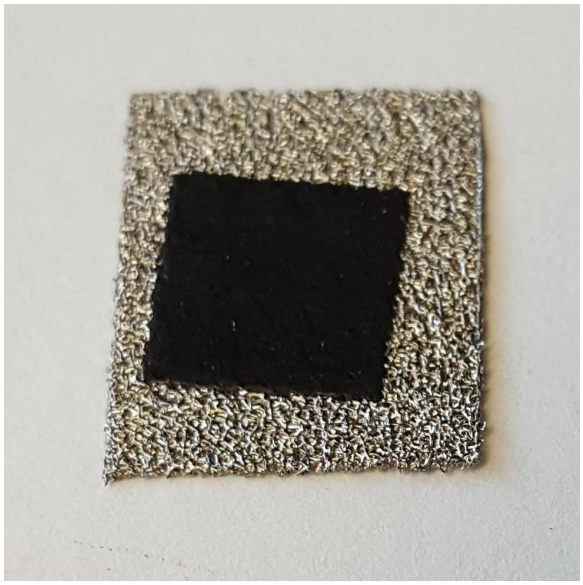

Figure 15. Electrode film pressed into Ni foam.

Iron powder can be converted into a porous thin plate by sintering over nickel or nickel-plated steel foil/mesh at 700 – 800°C in hydrogen atmosphere.[10] The matrix in sintered electrodes serves as both active materials and current-conducting grid. Despite their high conductivity, sintered electrodes exhibit the limitations for use due to i) high cost

for process, ii) rapid passivation of surface and iii) high temperature causing undesired deformation of iron particles. Although the last one is a core principle of sintering, it is not applicable for nano-sized iron with particular structures which is currently reported to bring enhanced electrochemical performance.[36, 42, 44-45, 70-71]

Regarding other components for cells, electrolytes contain high molarity of potassium hydroxides making them alkaline. The addition of lithium hydroxides is also favored because it is known that Li^+ ions bring benefit to the improvement of kinetic parameters though the proposed mechanisms vary. Giles and Hampson et al. reported that the structure of oxide/solution interface changed at low Li^+ concentration, causing the hindrance to HER.[72-73] Hills et al. proposed a delay in the onset of iron passivation at the presence of Li^+,[74] which was experimentally substantiated by Guzman et al.[75] Casellato et al. suggested that lithium ions help the reduction of iron oxides by forming Li^+-intercalated iron oxides as readily-reducible intermediates.[35] The materials for porous separator can be polyvinyl chlorides (PVC), polyethylenes (PE), polyamides (PA) or polypropylenes (PP). Cell cases usually have vents to permit the escape of gases produced in cells.

CHAPTER 3. MORPHOLOGY AND PHASE CHANGES IN IRON ANODES

This study aimed to correlate the changes in the electrochemical behavior of micro-scale Fe upon deep cycling in alkaline conditions with the changes in its morphology and phase. CV identified that Fe anodes undergo four stages classified by the capacity and efficiency changes during the charge-discharge cycling: development (Stage I), retention (Stage II), fading (Stage III) and failure (Stage IV). By conducting the analyses using SEM, XRD and Raman spectroscopy, it was found that each stage is associated with very specific changes in the morphology and phase of Fe anodes.

3.1 Experimental Details

Micro-scale high-purity carbonyl iron (Sigma-Aldrich, US, > 99.5%, 5 – 9 μm, Figure 16) was chosen as an active material. The electrode paste was prepared by blending active material, conducting agent, binder and additive in ethanol with a designated weight percentage: 70% of Fe, 17% of PureBLACK® (Superior Graphite, US), 10% of PTFE (Aldrich, 60% suspension) and 3% of Bi_2S_3 (Sigma-Aldrich). A roll-milled wet film was cut and impregnated into Ni foam current collector (Novamet, US, thickness 1.4 mm, pore size 590 μm) under 3 atm for 30 s by a hydraulic press. The electrodes were dried at 80°C in vacuum overnight. The reference samples for Raman spectroscopy and CV were made

with commercial γ-Fe_2O_3 (US Research Nanomaterials, US, 20 – 40 nm) or Fe_3O_4 (Sigma-Aldrich, < 5 μm) powder while everything else was the same.

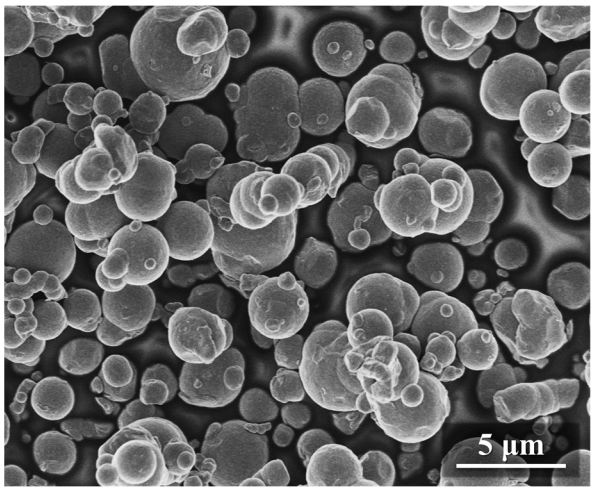

Figure 16. SEM image of pristine micro-scale Fe particles.

Three-electrode beaker cells were fabricated with Fe electrode, Pt plate (Alfa Aesar, US) and Hg/HgO electrode (Koslow, US) for working, counter and reference electrodes (WE, CE and RE), respectively, in order to eliminate any possible effects from NiOOH cathode and thus to focus on the study of Fe anodes. 8M KOH + 1M LiOH (Alfa Aesar) alkaline solution was prepared for electrolytes. CV was performed in the potential range of -1.3 – -0.3 V vs. Hg/HgO with 0.5 mV/s of scan rate by a potentiostat (SI1480, Solartron Analytical, US). All the measurement was conducted at room temperature 2 h after the cell fabrication.

Cycled electrode samples for post-mortem analysis were obtained from the cell containing multiple working electrodes. Each sample was removed from the cell immediately after its designated cycle, washed by DI water several times and dried at 80°C in vacuum overnight. X'Pert PRO Alpha-1 (PANalytical, Netherlands) and SU8010

(Hitachi, Japan) were used for XRD and SEM characterization, respectively. Raman spectrum was acquired by confocal Raman microscope (alpha300, WITec, Germany) with a 532 nm laser source. The resolution of the instrument was 1 cm^{-1} with 1800 grooves/mm. Under 5 mW of laser power, the spectrum was collected 20 times with 10 s of acquisition time for each to prevent undesirable oxidation of samples.[76-84]

3.2 Electrochemical Behavior upon Charge-Discharge Cycling

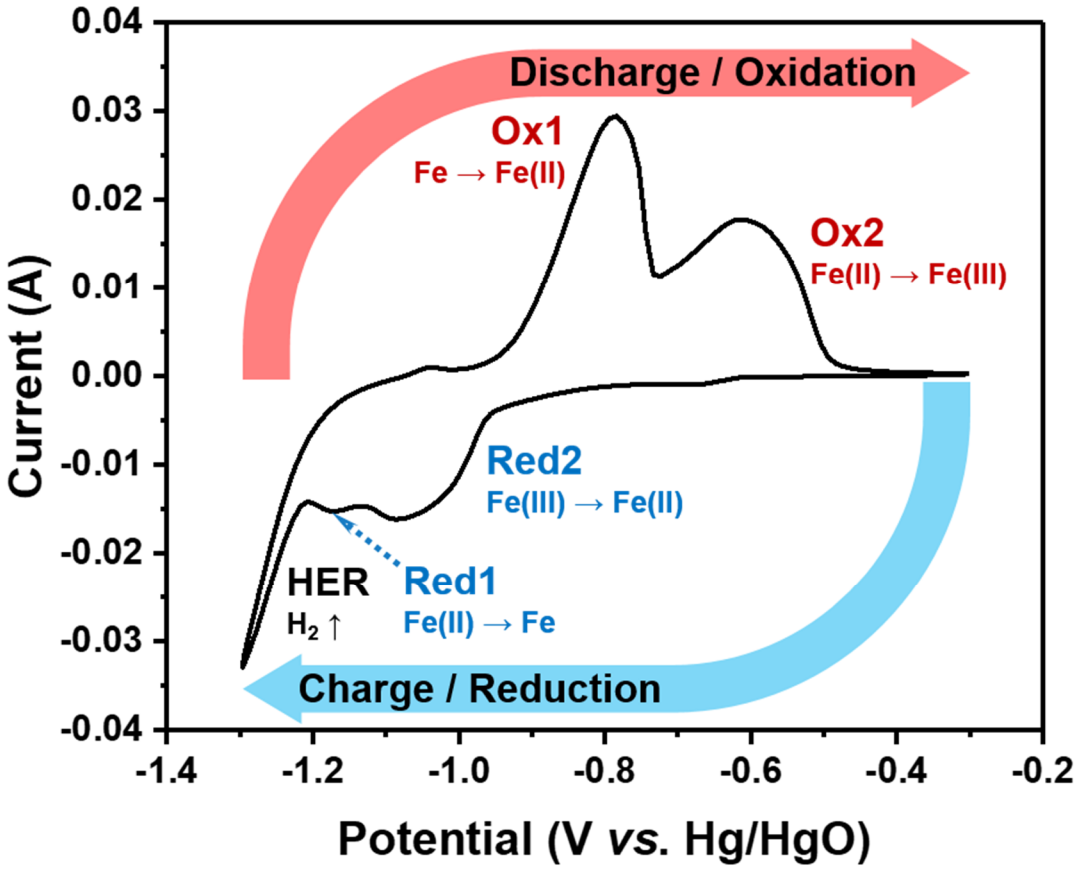

Figure 17. Explanatory CV curve with redox peaks assigned to corresponding reactions. The 50th cycle was chosen due to its maxima in capacity and efficiency.

A representative CV curve in Figure 17 shows electrochemical reactions occurring on Fe electrode within a broad potential range (from -1.3 to -0.3 V vs. Hg/HgO). It is considered as a "deep" cycling regime, where all the oxidation and reduction processes have sufficient driving forces to proceed. The position and the intensity of the prominent peaks in Figure 17 correspond to the potential and the rate of reactions, respectively. A major anodic peak at around -0.79 V is assigned to the oxidation of Fe into $Fe(OH)_2$ as the first discharge reaction (Reaction 1). The detailed mechanism of this reaction (Ox1 peak in Figure 17) is based on a dissolution-precipitation process with a soluble ferrite intermediate ($HFeO_2^-$) previously described in several important publications:[26, 29, 31, 48, 85]

$$Fe + 2OH^- \leftrightarrow Fe(OH)_2 + 2e^- \qquad (E° = -0.98 \text{ V vs. Hg/HgO}) \quad (1)$$

$$Fe + 3OH^- \leftrightarrow HFeO_2^- + H_2O + 2e^- \quad (1\text{-}1)$$

$$HFeO_2^- + H_2O \leftrightarrow Fe(OH)_2 + OH^- \quad (1\text{-}2)$$

The subsequent second oxidation reaction (Ox2) is observed at around -0.62 V (Figure 17). The reaction pathway(s) and both the final and intermediate product phase(s), however, are not easily identifiable. Indeed, over the last 50 years of study on Ni-Fe batteries, a broad range of the reaction pathways and product phases have been proposed or claimed for this Fe(II)-to-Fe(III) transition.[15, 19-35] Based on the prior art studies, one can hypothesize that the final product of Ox2 should likely be feroxyhyte (δ-FeOOH),[15, 19-22, 30-31, 34] magnetite (Fe_3O_4)[23-25, 32-35] or hematite (α-Fe_2O_3).[36-40] The in-depth phase identification for this reaction will be examined and discussed later in this chapter.

$$Fe(OH)_2 + OH^- \leftrightarrow FeOOH + H_2O + e^- \qquad (E° = -0.65 \text{ V vs. Hg/HgO}) \quad (2)$$

$$3Fe(OH)_2 + 2OH^- \leftrightarrow Fe_3O_4{\cdot}4H_2O + 2e^- \qquad (E° = -0.76\ V\ vs.\ Hg/HgO) \quad (3)$$

$$2Fe_3O_4 + 2OH^- \leftrightarrow 3Fe_2O_3 + H_2O + 2e^- \qquad (E° = -0.70\ V\ vs.\ Hg/HgO) \quad (4)$$

The reduction reaction Red2, corresponding to Ox2, takes place at around -1.09 V as the first charge. Then the subsequent reduction to metallic Fe (Red1) starts to arise at around -1.17 V. A significant portion of the Red1 peak, however, is buried in a steep cascade of hydrogen evolution reaction (HER), which implies that a full charge of Fe anodes is inevitably accompanied by hydrogen evolution. Such a competition at a relatively high negative potential is in expectation because HER has a similar redox potential in alkaline media to that of Red1 (Reaction 1 vs. 8). As a parasitic side reaction against the charging reaction of Fe anode, HER consumes electrical charge from the current for charging and induces the hydrogen accumulation on anode surface, which causes low cell efficiency and high electrode polarization.

$$2H_2O + 2e^- \rightarrow H_2 + 2OH^- \qquad (E° = -0.93\ V\ vs.\ Hg/HgO) \quad (8)$$

By integrating the area under the current curves in CV, the capacity and efficiency were calculated for each cycle to discern the overall change in the electrochemical behavior of iron anodes over cycling. The calculations for specific capacity and discharge/charge efficiency are given as the followings:

$$Anodic\ (Cathodic)\ Specific\ Capacity\ [mAh/g]$$
$$= \frac{Area\ under\ positive\ (negative)\ current\ [A \cdot V]}{Fe\ mass\ [g]\ \cdot\ Scan\ rate\ [mV/s]} \times \frac{10^6}{3600}$$

$$Discharge/Charge\ Efficiency\ = \frac{Anodic\ Specific\ Capacity}{Cathodic\ Specific\ Capacity}$$

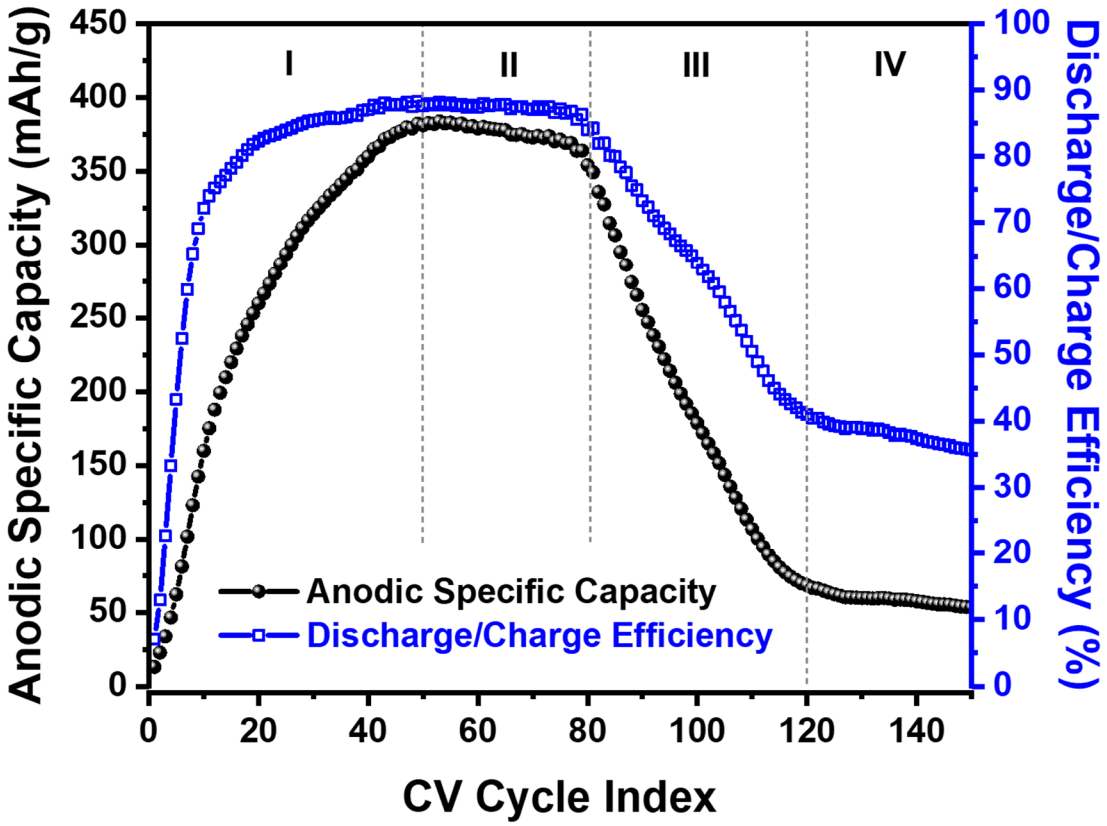

Figure 18. Evolution of anodic specific capacity and discharge/charge efficiency over charge-discharge cycling by CV. The specific capacities were calculated by integrating the areas under the CV curves and normalizing them with Fe mass.

Dynamic changes were observed in capacity and efficiency over 120 cycles (Figure 18). The author subdivided the evolution of Fe anodes into four distinct stages: both discharge capacity and discharge/charge efficiency gradually increase and reach their maxima at the 50th cycle (Stage I: Development, Figure 19a and b), stay nearly constant during cycles 50 – 80 (Stage II: Retention, Figure 19c), undergo rapid fading to their minima at the 120th cycle (Stage III: Fading, Figure 19d), and then remain small (Stage IV: Failure). Note that the capacity fading in Stage III was more substantial than what is

typically observed in commercial cells because the anode was cycled in a broader potential range for the research purpose.

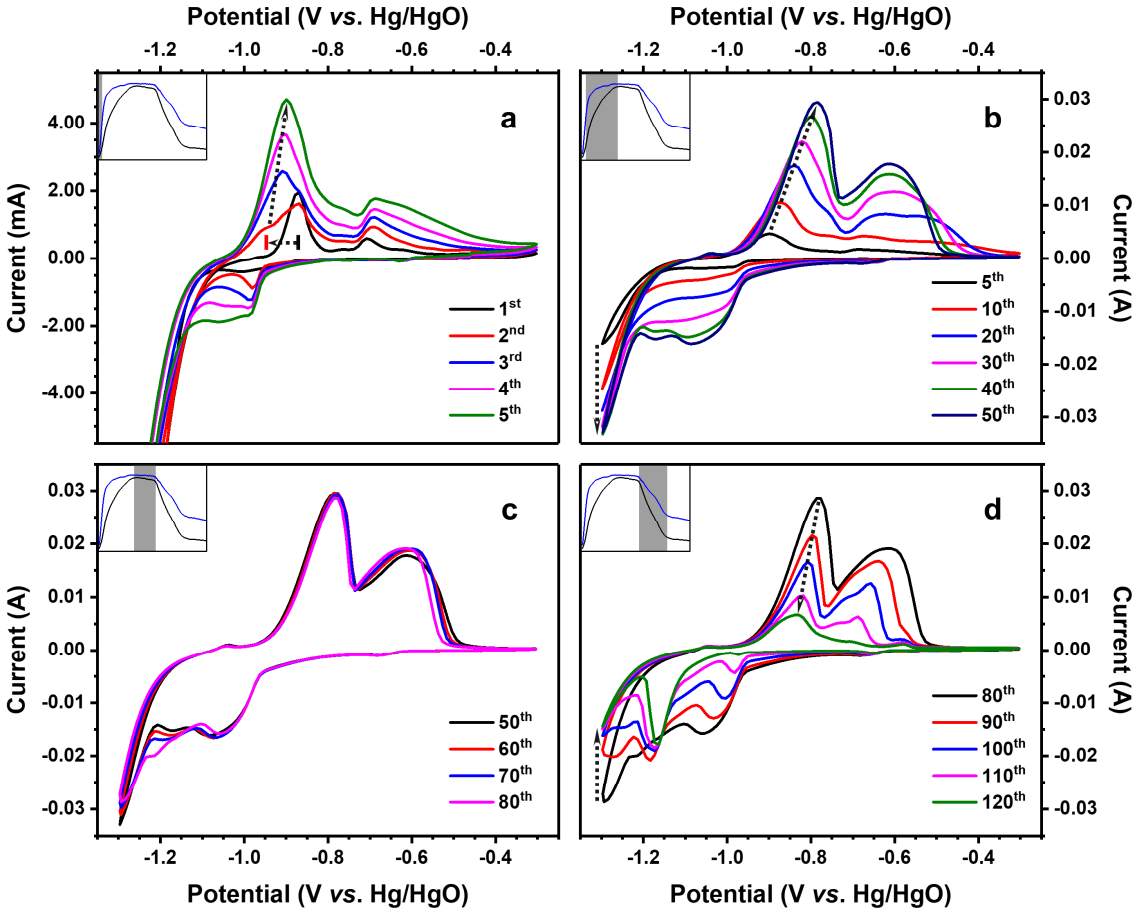

Figure 19. CV curves for (a) early Stage I, (b) Stage I, (c) Stage II, and (d) Stage III. Stage IV showed no significant change in CV curves after the 120th cycle. Note that the scale of the current axis in panel a is smaller than that in the other panels. Figure 18 is simplified into the insets to represent the capacity and efficiency change for each corresponding stage. The arrows help follow the discussion, and their direction indicates the progress of cycling.

3.3 Post-Mortem Analysis for Morphology and Phase Changes

3.3.1 Stage I: Development

Post-mortem analysis enabled the author to connect the electrochemical response of Fe electrodes to their morphological and structural changes during CV cycling. Despite that the starting electrode materials were pristine metallic iron particles, the 1st charge exhibited a small Red2 peak in Figure 19a, which was likely from preformed oxidized surface by exposure to air. As its reduced products, Figure 20a showed nano-sized granules on the Fe particle surface which were not observed in the pristine particles in Figure 16. The subsequent discharge made them oxidized inducing their volume expansion and further roughening of surface, but the individual particles maintained the shape (Figure 20b). The 2nd charge removed the granule-containing oxide layer and disclosed a fresh surface which lay beneath it at previous cycle (Figure 20c). A series of SEM observations in Figure 20 suggests that the charge-discharge reactions of iron particle are surface-limited. This can be attributed to the dissolution-precipitation mechanism of iron anodes (Reaction 1-1 and 1-2) as well as the slow mass transfer of hydroxide anions through the solid-state phase of particles.[37]

After the preformed surface oxide layer vanished via the dissolution-precipitation process (transition from Figure 20b to c), the reaction sites become determined by i) the degree of lattice mismatch at grain boundary and the corresponding interfacial energy, and ii) the diffusion distance of hydroxide anion from the electrode/electrolyte interface (EEI). The charge-discharge reactions can now start taking place at both the Fe particle surface and the near-surface grain boundary region inside particles. In the same manner of the

initial dissipation of surface (Figure 20b to c), the charge-discharge reactions occurring at the grain boundary inside particles make the reacted volume dissolve away from the grain boundary (and precipitate elsewhere). Some groups of grain lumps, therefore, are expected to break away from the core of particles, which preferably happens first at the near-surface grain boundary due to a short diffusion distance.

Such speculation was confirmed by the subsequent SEM observations; at the 2nd discharge, Fe particles exhibited the beginning of rupture from its inside (Figure 20d). Then the particles gradually crumbled from their surface during the early cycling (Figure 20e to h), which eventually led to pulverizing the initial micro-scale Fe into much smaller fragments and making them porous. Consequently, an increase in the surface area of Fe raised the rates of charge-discharge reactions which are surface-limited. The growth for all redox peaks in Stage I (Figure 19a,b) reflected such a microstructure change bringing about the capacity increase in Figure 18. The CV peaks also showed their shift into larger overpotential during Stage I, which was representatively observed at Ox1 in Figure 19a and b. It can be attributed to the Fe anodes becoming more porous, introducing more reaction sites but with longer diffusion distance to hydroxide anions. Ox1 peak showed the opposite shift exceptionally for the initial discharge reactions (1st and 2nd in Figure 19a), revealing that the preformed surface layer was in more readily-oxidizable condition, with shorter diffusion distance, than bulk Fe particles.

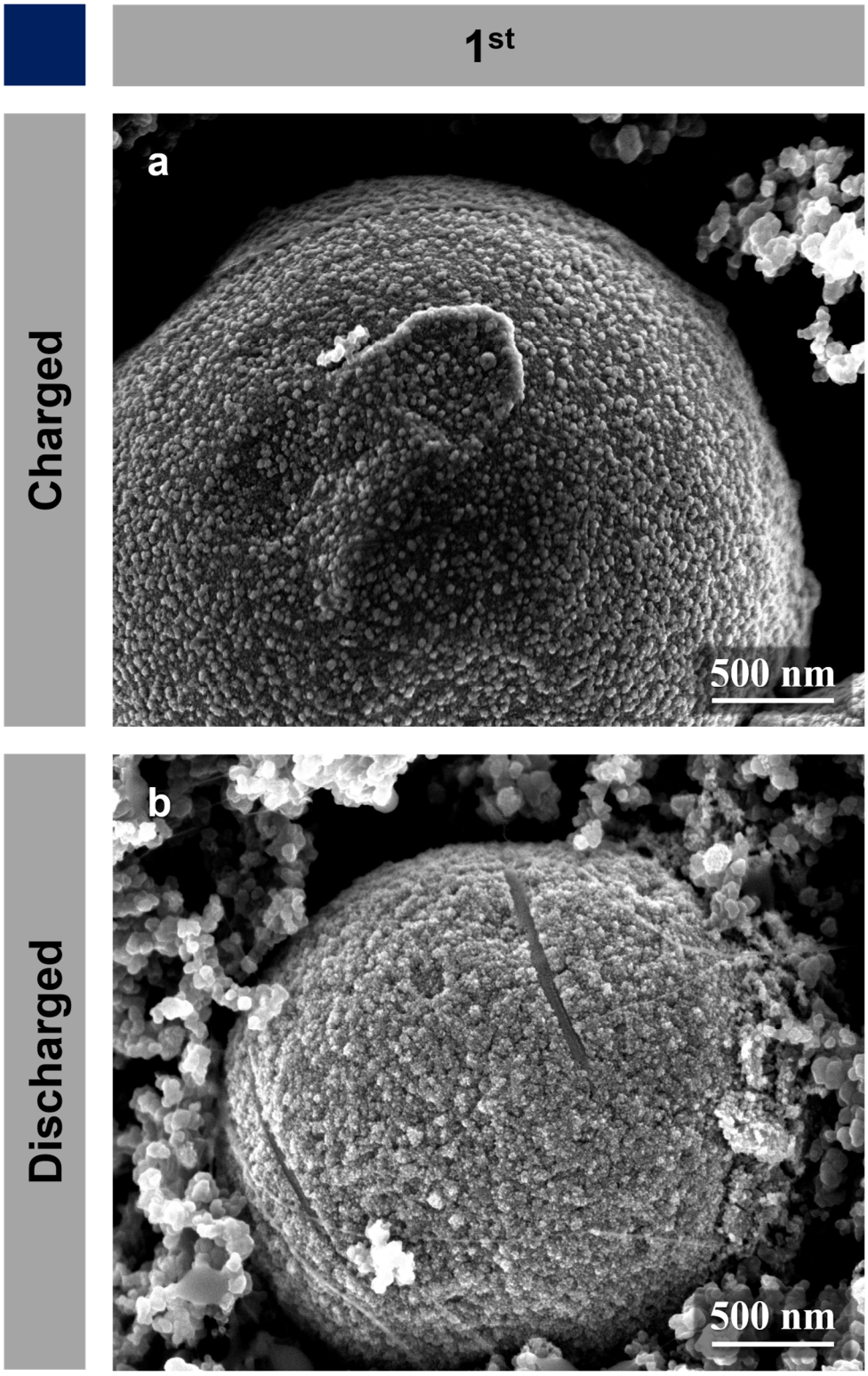

Figure 20. SEM images of Fe particles after the (a) 1st charge and (b) 1st discharge.

Note that the small nanoparticles around Fe are carbon black powder.

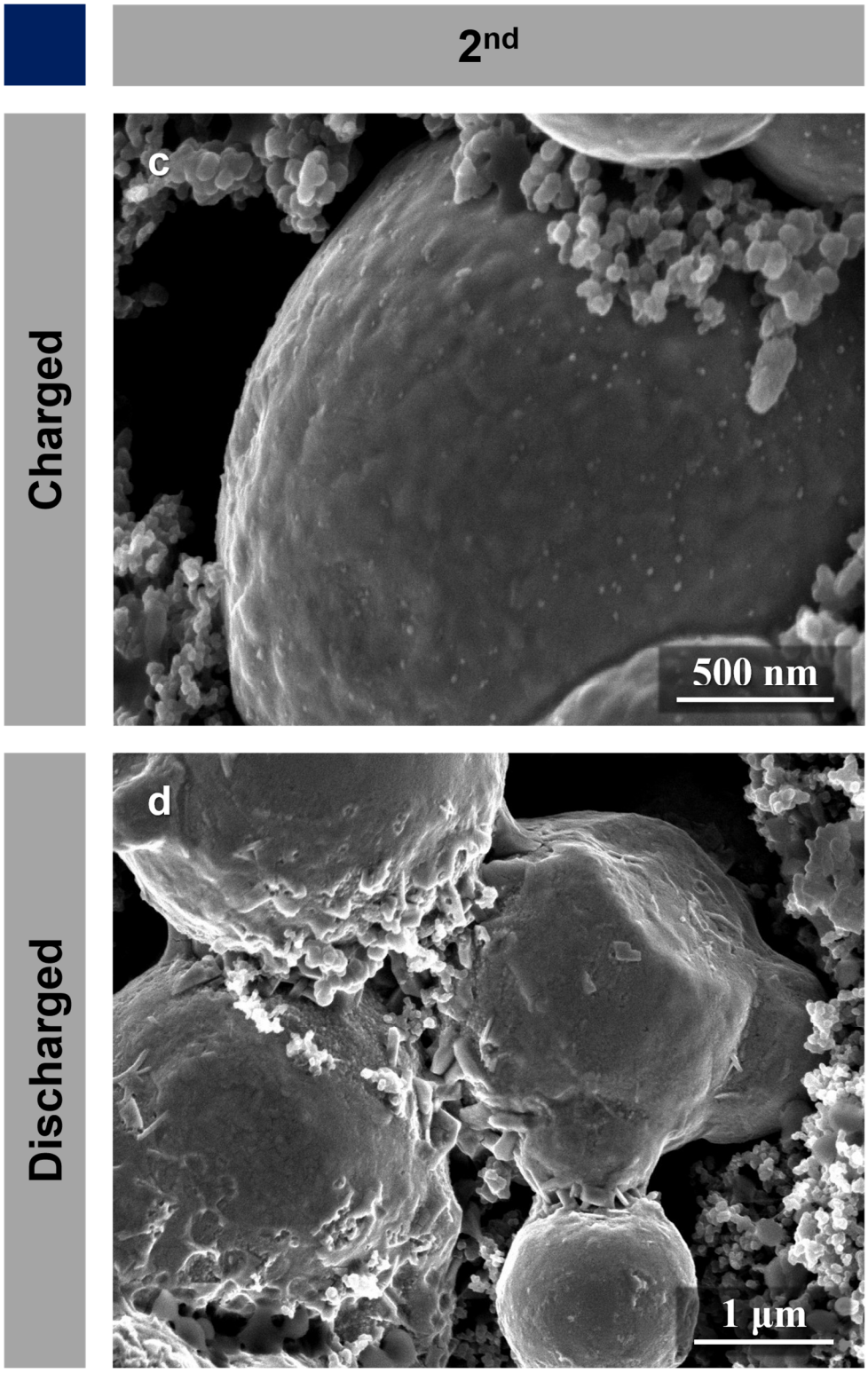

Figure 20 (ctnd.). SEM images of Fe particles after the (c) 2nd charge and (d) 2nd discharge. Note that the small nanoparticles around Fe are carbon black powder.

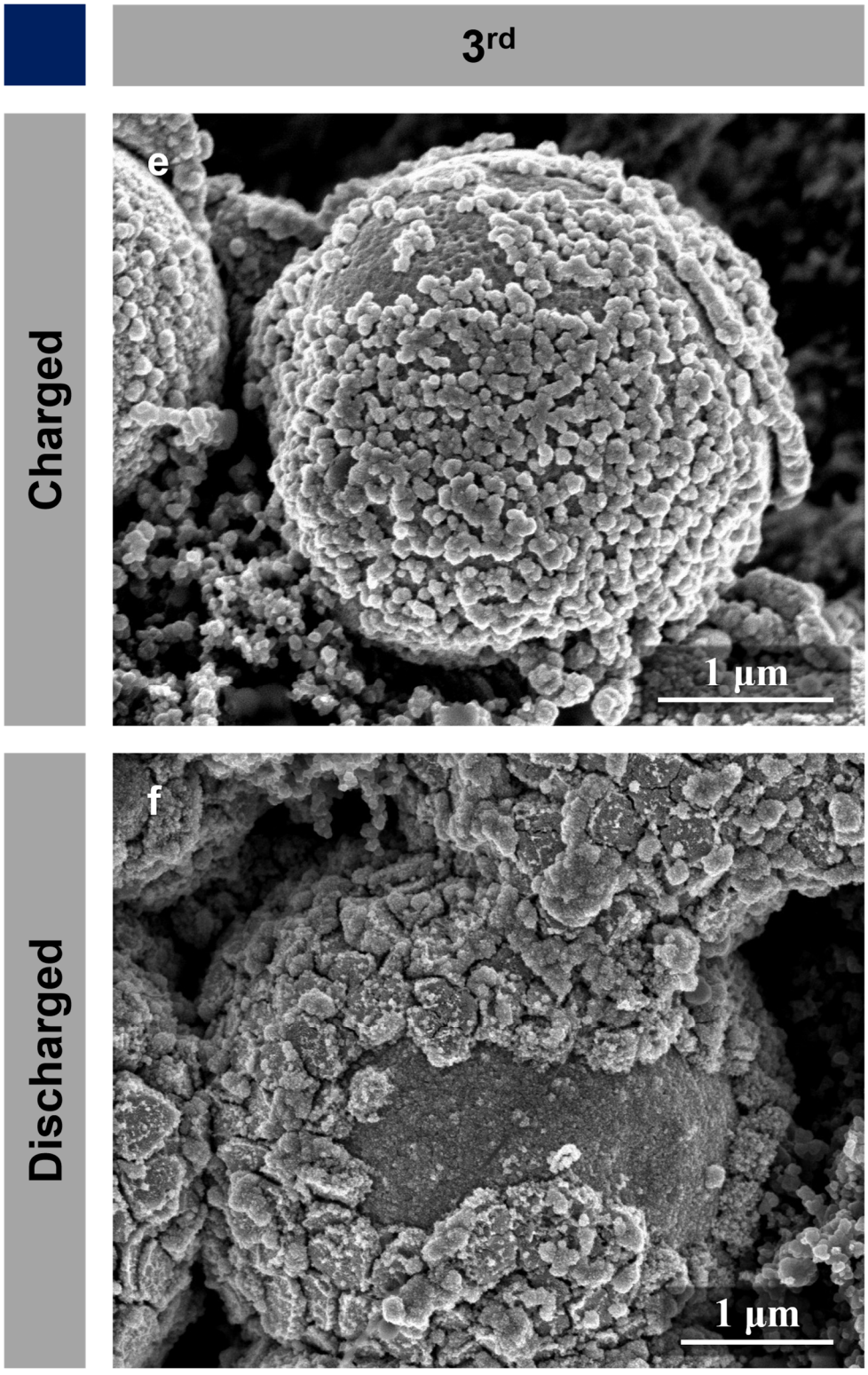

Figure 20 (ctnd.). SEM images of Fe particles after the (e) 3rd charge and (f) 3rd discharge. Note that the small nanoparticles around Fe are carbon black powder.

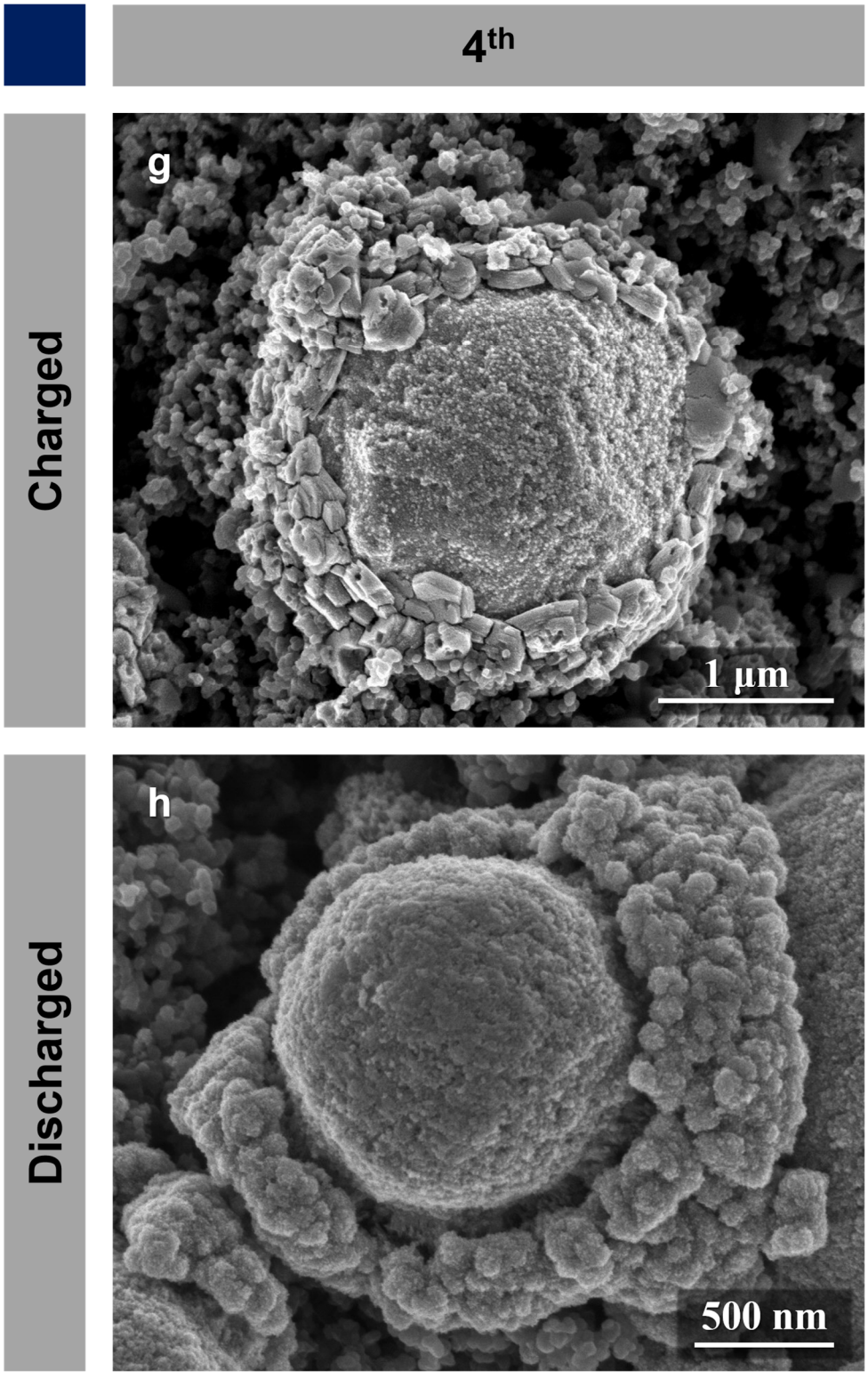

Figure 20 (ctnd.). SEM images of Fe particles after the (g) 4th charge and (h) 4th discharge. Note that the small nanoparticles around Fe are carbon black powder.

Since the major portion of cathodic current was consumed by HER rather than charging (i.e., poor charging efficiency in Stage I), a gain in discharge/charge efficiency during Stage I originated from the increase in discharge capacity (Figure 18). The augmentation of HER in Figure 19b not only demonstrates that the particle fragmentation caused the increase in surface area but also implies that the surface preserved its metallic state at negatively high potential over Stage I. The accumulation of hydrogen at the surface might also contribute to the overpotential increase during the cycling of Fe anodes.

XRD analysis of the anode in charged state revealed that pure metallic phase (α-Fe) remained dominant during Stage I (Figure 21), suggesting that the whole anode could be effectively reduced (i.e., highly reversible) after the oxidation in each cycle. No significant amount of electrically/electrochemically isolated oxide phases was detected until the end of Stage I.

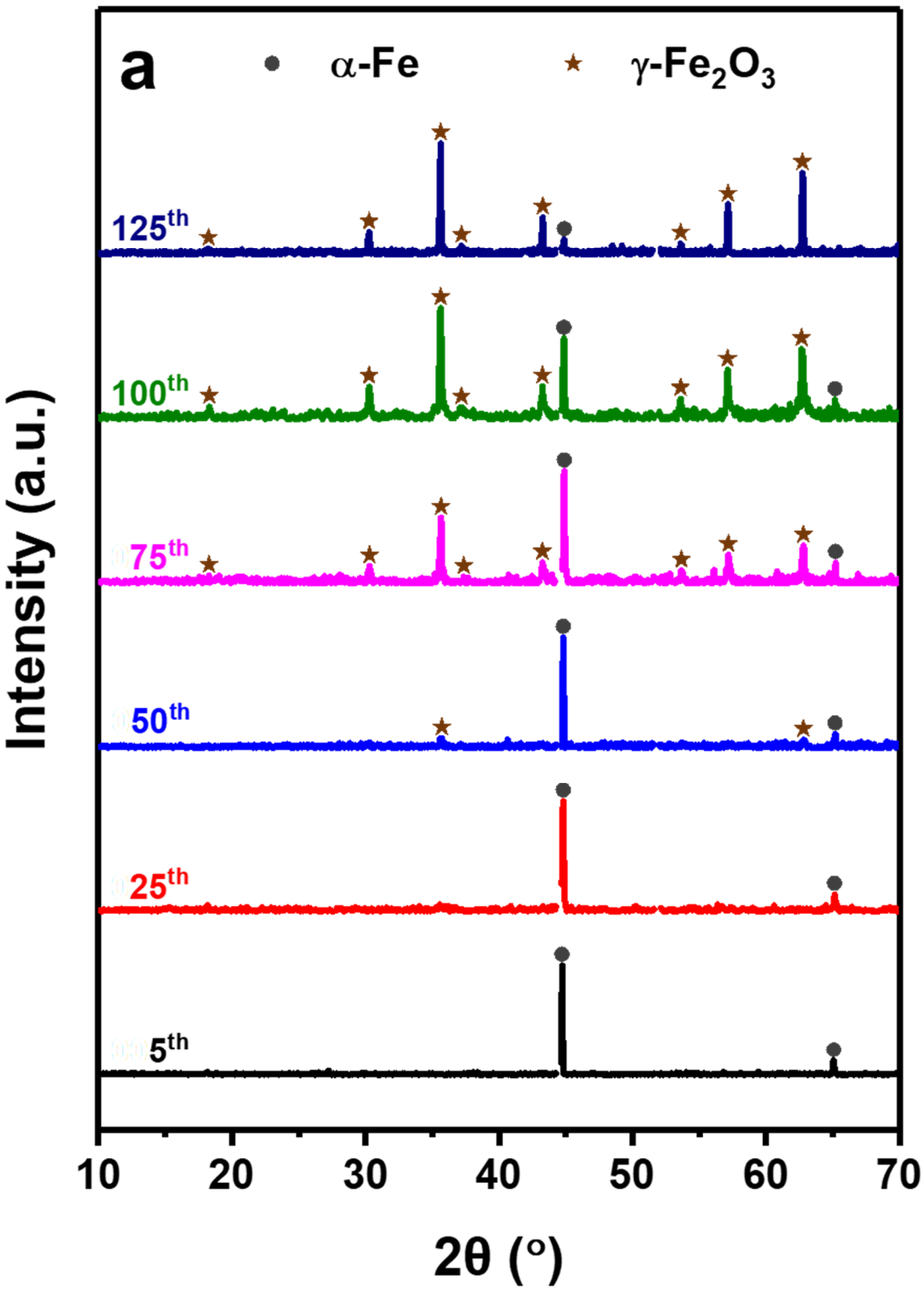
a
α-Fe
γ-Fe2O3
125th
100th
75th
50th
25th
5th
Intensity (a.u.)
10
20
30
40
50
60
70
2θ (°)

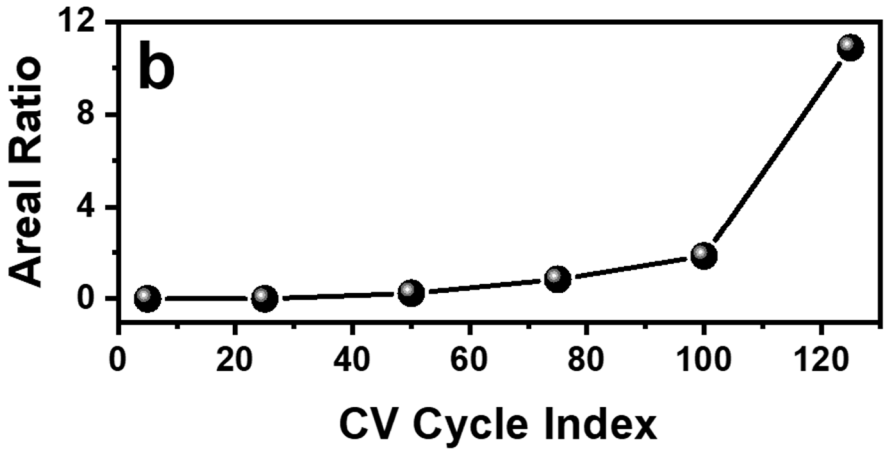

Figure 21. (a) Evolution of XRD spectra over charge-discharge cycling of Fe anodes. The carbonyl iron originally used has α-Fe phase. Note that the spectra of Ni current collectors were removed to improve legibility. (b) Areal ratio of γ-Fe_2O_3 (311) peak to α-Fe (110) peak in XRD spectra.

3.3.2 Stage II: Retention

At the 50th cycle, nearly all particles lost the initial spherical shapes (Figure 22). Due to the insignificant further change in electrode surface area expected during Stage II, the maxima in capacity and efficiency were maintained till the 80th cycle while the electrode kept exhibiting the same electrochemical behavior (Figure 19c). SEM observations, however, revealed the formation of octahedra which can be considered as the monocrystalline morphology of the crystals with $Fd\bar{3}m$ space group (Figure 23a).[77, 86] At the same time, XRD detected initially small but growing signal of either magnetite (Fe_3O_4) or maghemite (γ-Fe_2O_3) phase (Figure 21a). Note that γ-Fe_2O_3, a cation-deficient form of Fe_3O_4, has the same crystal structure and corresponding space group as those of Fe_3O_4

when the cation vacancies are randomly distributed over the octahedral interstitial sites (cubic inverse spinel belonging to $Fd\bar{3}m$).[87-88] Consequently, nearly identical XRD spectra exist for γ-Fe_2O_3 and Fe_3O_4,[77, 82, 89-92] where only an insignificant peak shift (JCPDS# 39-1346 vs. 88-0315) and very minor additional peaks for γ-Fe_2O_3 ((110), (210) and (211)) may distinguish one phase from the other (commonly under the noise level for small particles). To the best of the author's knowledge, nearly all prior studies claimed this phase, a product of Fe(II)-to-Fe(III) oxidation (Ox2), to be Fe_3O_4.[23-29] We, however, believe that those conclusions had been premature and such crystals are γ-Fe_2O_3; while no reasons were given to rule out either, the author found that the assumed accumulation of Fe_3O_4, a phase reported to deliver a reversible capacity,[42, 47, 93] could hardly bring a cell failure in the last cycling stages which will be discussed later in this chapter.

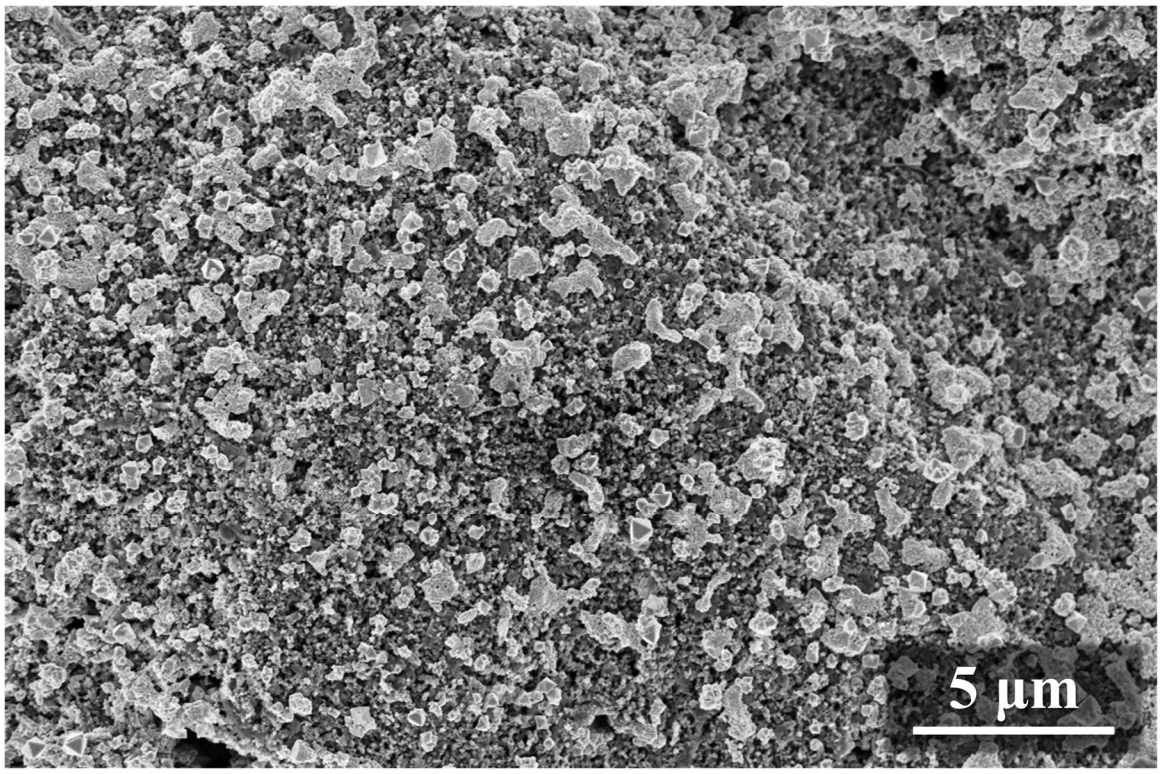

Figure 22. SEM image of cycled Fe anode after 50 cycles.

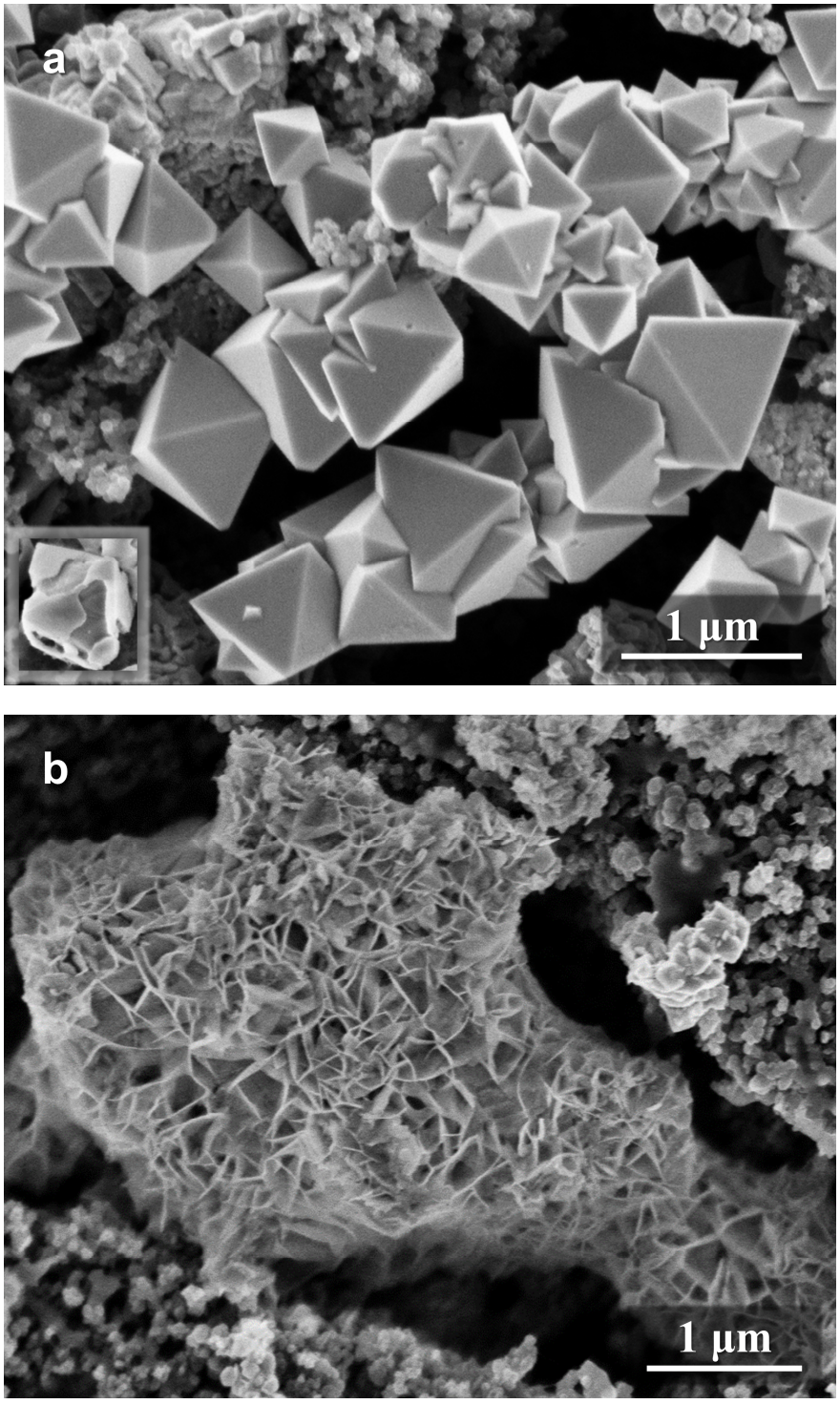

Figure 23. (a) Octahedral maghemite particles and (b) basalt-like iron fragment observed in cycled Fe anode after 75 cycles. The inset in (a) shows an incompletely-formed octahedron found from another region of the same electrode.

Since XRD results were not satisfying, Raman spectroscopy was employed for further phase identification. By presenting the a_{1g} band at 705 cm^{-1} (Figure 24), Raman spectroscopy studies confirmed that the octahedral crystals, which accumulate in the cycled anode, are indeed γ-Fe_2O_3 rather than Fe_3O_4 with its a_{1g} band at 670 cm^{-1}.[76-84] A narrower peak of the cycled electrode than that of commercial maghemite is attributed to a higher crystallinity of octahedra, individually composed of a single domain. A weak laser power (5 mW) did prevent the particles from an undesirable oxidation into hematite as the author intended, but precluded the detection of minor bands for all samples. Along with the octahedral crystals, the spherical particles with similar size (~500 nm) also started to appear in Stage II (Figure 25). This is due to the different growth mechanism caused by a local inhomogeneity of surrounding ions at EEI when oxidizing $Fe(OH)_2$ particles.[77, 94] If the surface has the excess of Fe^{2+} dissolved, the local pH can be close to the isoelectric point of iron oxides allowing the aggregation of minuscule primary particles into spheres. In contrast, the excess of OH^- results in higher local pH inducing the surface of growing particles to be charged. It eventually enables the particle growth by molecular addition, which was confirmed by the incomplete form of octahedra found in the inset of Figure 23a. Raman spectroscopy on spherical particles gave the same results except for higher peak broadness, as expected.

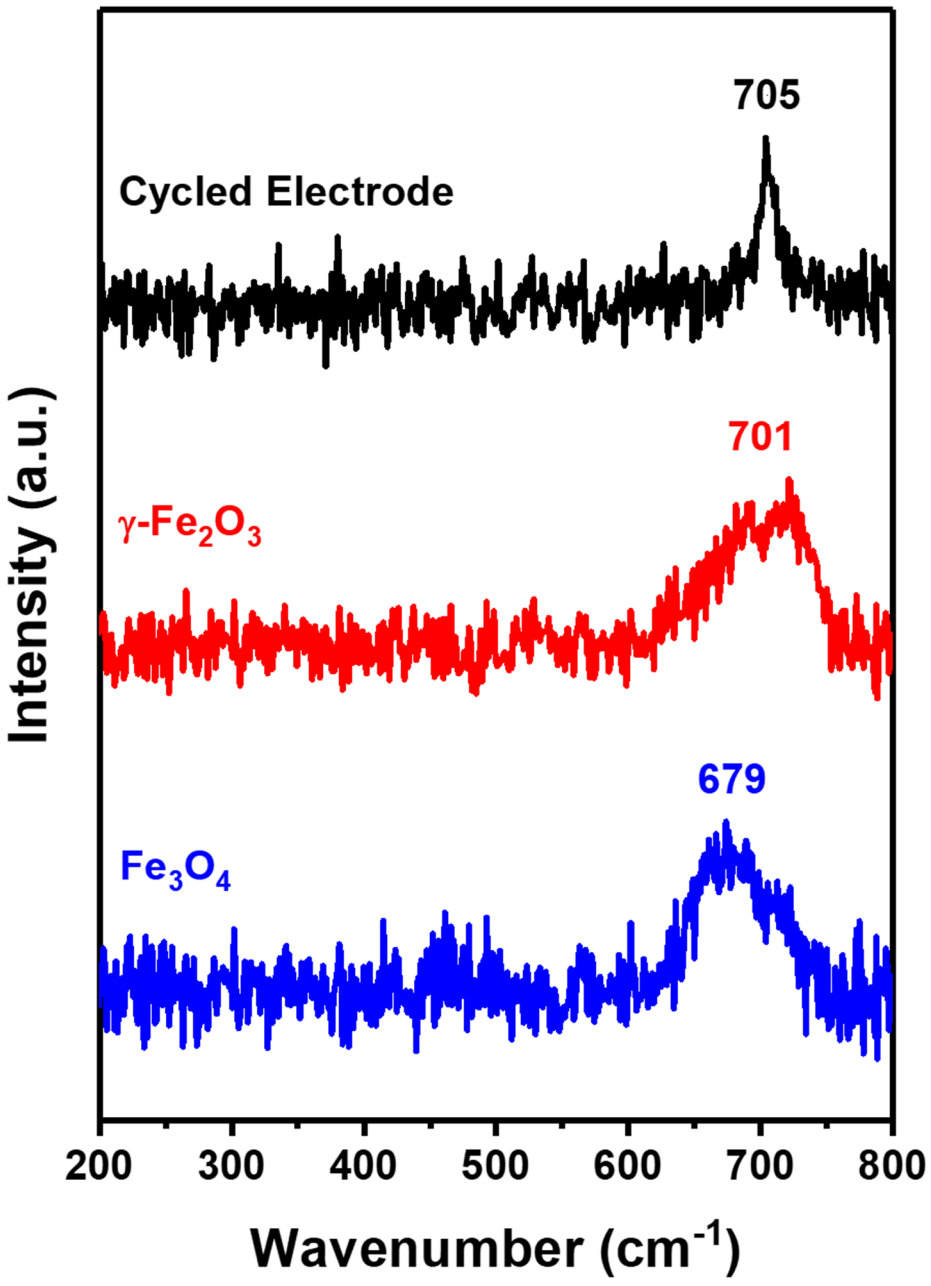

Figure 24. Raman spectra of cycled Fe anode after 125 cycles. Commercial powders were also examined for the comparison purpose. The obtained signals were processed for the background removal and peak normalization. A weak laser power did prevent an undesirable oxidation into hematite but precluded the detection of minor bands for all samples.

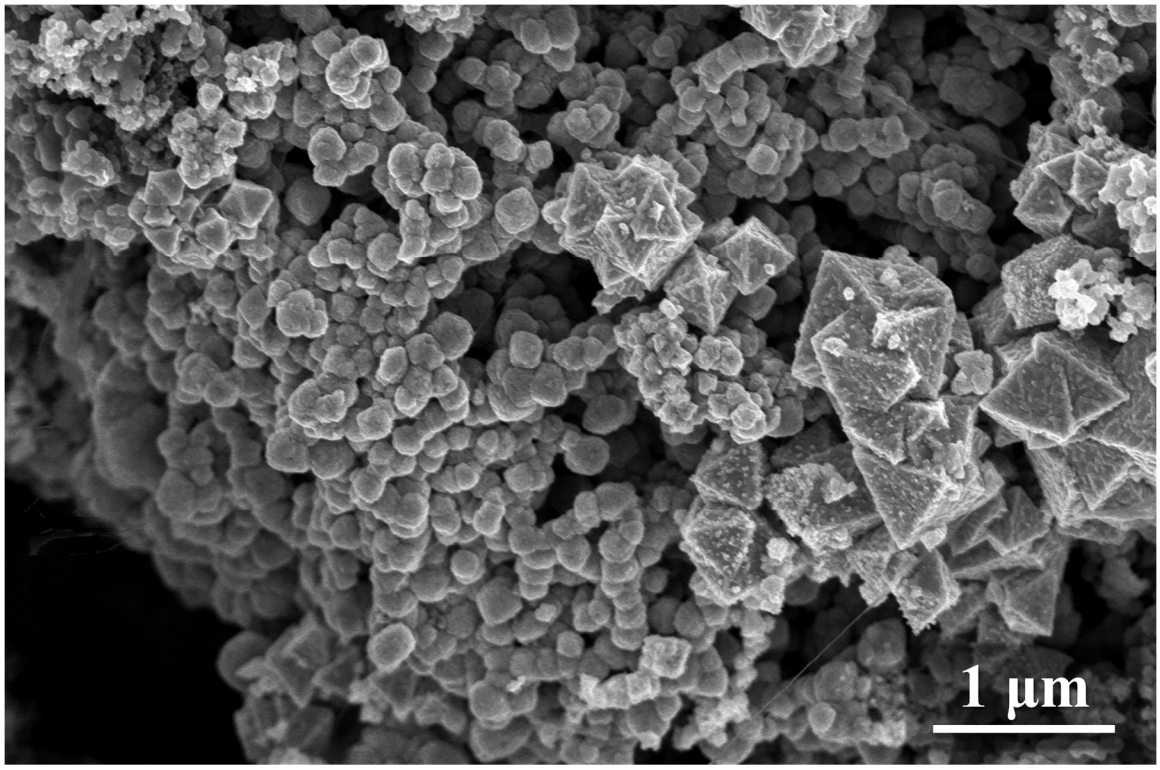

Figure 25. SEM image of cycled Fe anode after 75 cycles: another region in the same electrode of Figure 23a.

Although Stage II was represented by the initiation of γ-Fe_2O_3 formation, the retention of capacity and efficiency came from the remaining Fe accounting for a major portion of electrode (Figure 21). Figure 23b shows another interesting morphological feature appearing in the cycled electrode – a host particle which underwent the dissolution. As previously discussed, the anode oxidation is largely based on the dissolution-precipitation process, where Fe first dissolves and forms the soluble ferrite anions ($HFeO_2^-$ in Reaction 1-1) which can diffuse to the favorable sites for precipitation as $Fe(OH)_2$ (Reaction 1-2). Since $Fe(OH)_2$ dissolves in highly concentrated alkali,[20, 31] the precipitated $Fe(OH)_2$ can be dissolved again and then re-precipitated into γ-Fe_2O_3, with a possible diffusion process of dissolved intermediates between such dissolution and precipitation

(Ox2). These diffusion-involved processes explain the disappearance of the reacted volume from the original Fe particles observed in Figure 20c or Figure 23b. The weak detection of γ-Fe_2O_3 at the 50th cycle (Figure 21a) indicates that such multi-step processes constantly occurred from the outset of cycling, but it did not become dominant until the beginning of Stage II at which the processes can be facilitated by the maximized surface area.

3.3.3 Stage III: Fading

From the 80th cycle, Fe anodes exhibited the abrupt capacity fading (Figure 18) coming from the diminishing redox peaks over Stage III (Figure 19d). The accelerated anode degradation in Stage III correlates very well with the accumulation of γ-Fe_2O_3 which likely exceeded its threshold at the end of Stage II. Figure 26 provides the phenomenological evidence for this statement by demonstrating very low capacity achievable in γ-Fe_2O_3 particles under the same alkaline condition used in this study. In contrast, Fe_3O_4 delivered a comparable capacity in line with the literature,[42, 47, 93] which supports the phase identification results for the product of Ox2 again. Such poor performance of γ-Fe_2O_3 in alkaline conditions might originate from its far lower electronic conductivity (1.8×10^{-8} S/cm)[95-96] than magnetite's (250 S/cm)[97-98] at room temperature.

SEM observations presented the detailed aspect of γ-Fe_2O_3 accumulation (Figure 27). Since XRD confirmed the minor existence of Fe in Stage III (Figure 21a), the agglomeration of γ-Fe_2O_3 octahedra is considered to clog the surface of remaining Fe fragments while their gradual irreversible oxidation into γ-Fe_2O_3 simultaneously takes place. A decrease in overpotential (Figure 19d) can be explained by reversing the

previously discussed mechanism for Stage I as the reactive surface/pores became blocked during Stage III. The reduction of HER current also supports this hypothesis, accounting for the slower fading of discharge/charge efficiency compared to that of anodic capacity during Stage III (Figure 18). While the formation of γ-Fe_2O_3 octahedra spread over the entire region of anode during Stage II, their precipitation on already existing γ-Fe_2O_3 crystals in Stage III might be attributed to i) more favorable heterogeneous nucleation than homogeneous one and/or ii) fully occupied sites for precipitation at the end of Stage II.

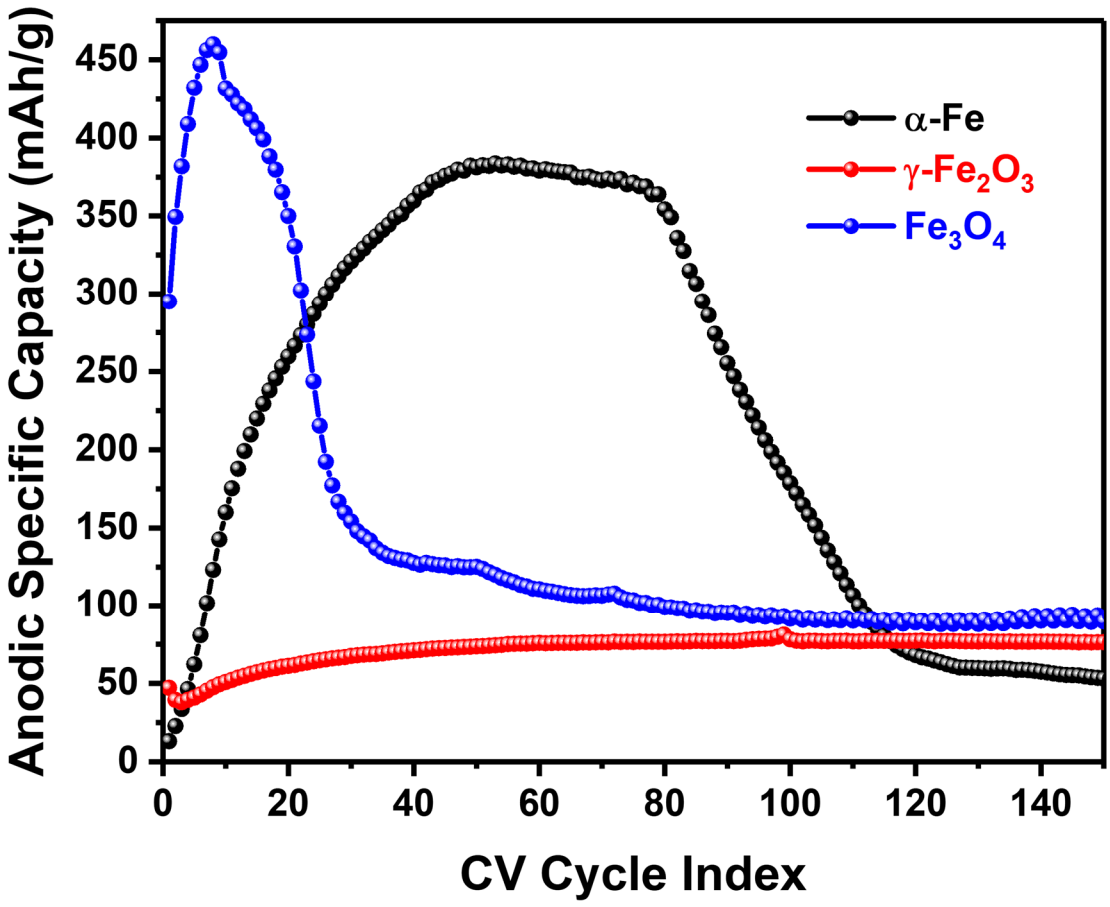

Figure 26. Electrochemical performance comparison for different starting phases.

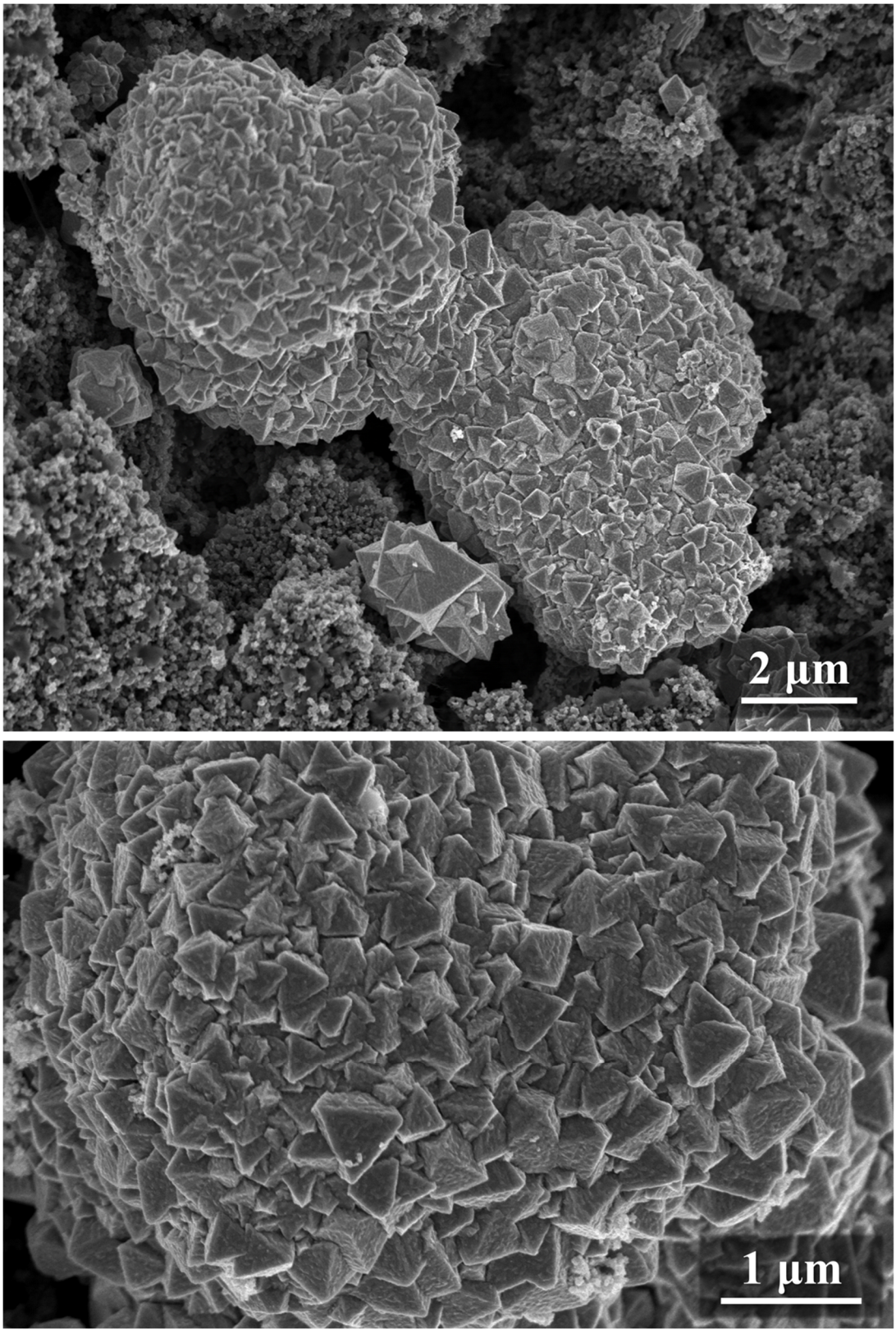

Figure 27. SEM images of particles in cycled Fe anode after 125 cycles.

3.3.4 Stage IV: Failure

Fe anodes in Stage IV remained with only one redox couple (Ox1 and Red1 in Figure 19d) and maintained the same electrochemical response for the rest of cycles. It is deduced that the Fe passivation by less-reactive species, γ-Fe_2O_3, hinders a further diffusion of hydroxide anions to the remaining components of anode and suppresses Ox2 as well as the corresponding Red2.

3.4 Model for Fe Anode Evolution

Caused by the surface-limited charge-discharge reactions, Fe particle fragmentation was observed from the initial cycles. The gradual increase in surface area led to developing capacity, which was maximized at the end of Stage I. During Stage II, the capacity decay was very slow while the initiated formation of γ-Fe_2O_3 octahedral monocrystalline particles was observed. The accumulation and aggregation of γ-Fe_2O_3 led to the subsequent rapid capacity fading (Phase III) and eventual failure (Phase IV). Electrochemical tests confirmed low electrochemical activity of γ-Fe_2O_3 in alkaline media. Overall, the electrochemical reactions on Fe anodes were composed of multi-step redox processes, involving the dissolution and precipitation of evolving phases as well as the diffusion of dissolved intermediates.

Figure 28 summarizes the morphological and structural changes in iron anodes over the deep charge-discharge cycling. It helps interpret multi-stage electrochemical behavior in terms of the morphology and phase changes discussed above. Although multiple events

simultaneously take place within each stage, it can be represented by its main characteristic phenomenon: particle fragmentation (Stage I), initiated γ-Fe_2O_3 formation (Stage II), accelerated γ-Fe_2O_3 accumulation (Stage III), and passivation by γ-Fe_2O_3 (Stage IV). The new insights obtained in this study suggest that future research efforts should be directed towards the suppression and, if possible, complete elimination of the γ-Fe_2O_3 nucleation and growth.

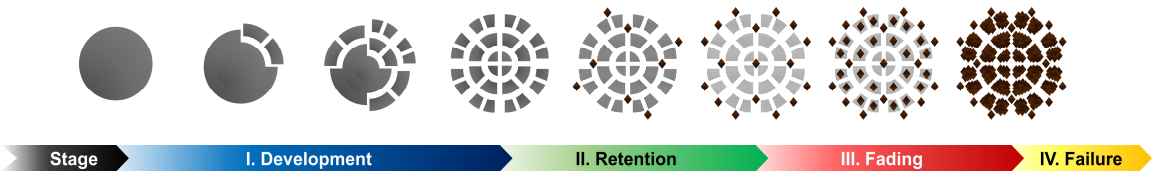

Figure 28. Morphological and structural changes in iron anodes over deep charge-discharge cycling. Iron and maghemite are painted with gray and brown, respectively, as their own colors. Stage IV (Failure) maintains the terminal condition of Stage III (Fading).

CHAPTER 4. ADJUSTMENT OF CELL OPERATING CONDITIONS

As an extension of previous research in Chapter 3, this study aimed to observe how the individual factor in cell operation influences the electrochemical behavior, morphology evolution and phase transition of Fe anodes. On the basis of experimental conditions applied in previous study, a variety of components were adjusted independently: potential range, electrolyte concentration, scan rate, and additive content. By analyzing the changes in CV results, SEM images and XRD spectra, the effect of each factor on cell operation was examined, which drew a conclusion for the performance optimization for Fe anodes in rechargeable alkaline batteries.

4.1 Potential Range

Chapter 3 revealed that the formation and accumulation of γ-Fe_2O_3 cause the capacity fading of Fe anodes followed by cell failure. One of the simplest strategies for suppressing its formation is to limit the discharge cut-off potential of Fe anodes, or the bottom cut-off voltage of cells, upon discharge (i.e., shallow discharge). In this case, the contribution of Fe(II)-to-Fe(III) transition to total capacity delivery becomes lost, but the improved stability of cell cycling can be expected.

A new discharge cut-off potential for CV cycling was determined as -0.75 V based on Figure 19 in which the results were obtained with -0.3 V. While this adjustment limits the development of Fe(II)-to-Fe(III) oxidation, -0.75 V is also deep enough (negatively low

enough in terms of potential) to gain high capacity utilization of Fe-to-Fe(II) oxidation. In addition, it takes the observed overpotential change (peak shift in Figure 19) into consideration.

Adjustment: -1.3 – -0.3 V vs. Hg/HgO → -1.3 – -0.75 V vs. Hg/HgO

Figure 29 exhibits only one couple of redox peaks, Ox1 and Red1 (+ HER), indicating that the shallow discharge successfully suppressed the Fe(II)-to-Fe(III) oxidation of Fe anodes. Overall, the results follow the basic model presented in Chapter 3.4: development (Figure 29a), retention (Figure 29b), and fading which is negligible though (Figure 29c). More detailed discussion on CV curves will be brought combined with other analyses later.

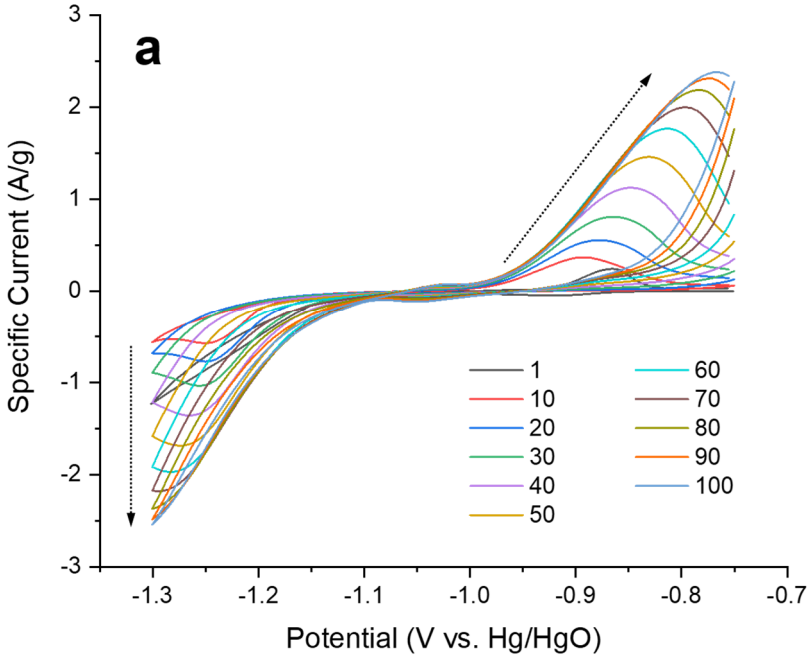

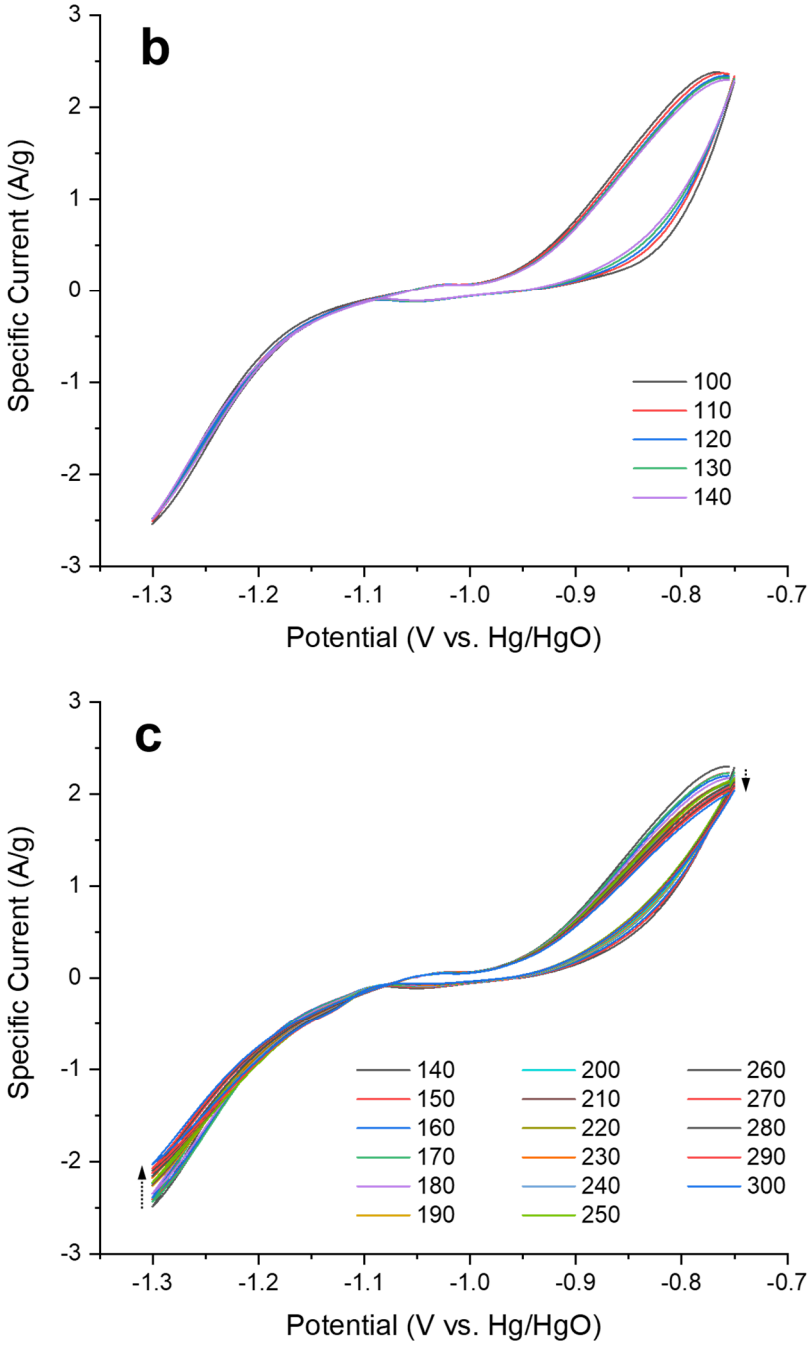

Figure 29. CV curves with -0.75 V as discharge cut-off potential (scan rate 0.5 mV/s): (a) 1st – 100th, (b) 100th – 140th, and (c) 140th – 300th. The first and every tenth cycles were presented. The direction of arrows indicates the progress of cycling.

As a consequence of the inhibition of Ox2, the cyclability of Fe anodes was remarkably improved (Figure 30). The sample examined in Chapter 3 (hereinafter referred to as "Ch3Ref") underwent rapid capacity fading from the 80th cycle and eventually became dead at 120th cycle. In contrast, the shallow discharge sample maintained its capacity with little loss over 200 cycles after the development stage terminated, which made the cell viable even at the 300th cycle (Figure 30a). The disappearance of drastic fading and failure stages supports the conclusion of Chapter 3 that the Fe(II)-to-Fe(III) oxidation reaction and its product γ-Fe_2O_3 are the culprit behind cell death.

Regarding capacity utilization, Ch3Ref could draw 375 mAh/g from deep discharge (before cell failure) while the shallow discharge sample delivered approximately 225 mAh/g (60%). Since the capacity contribution ratio between Ox1 and Ox2 is 2:1, based on their charge transfer (Fe/Fe(II) vs. Fe(II)/Fe(III)), the expected capacity from shallow discharge (Ox1 only) is 67% of that from deep discharge (Ox1 + Ox2). Considering a little capacity cut-off of Ox1 at -0.75 V (Figure 29), the observed capacity difference well fits the math, which implies that the exclusion of Ox2 does not influence the implementation of Ox1.

As discussed in Chapter 3, the formation of γ-Fe_2O_3 is irreversible, which additionally reduces the discharge/charge efficiency previously deteriorated by HER. Figure 30b demonstrates that the discharge/charge efficiency issue of Fe anodes can be resolved by the shallow discharge forming no irreversible species.

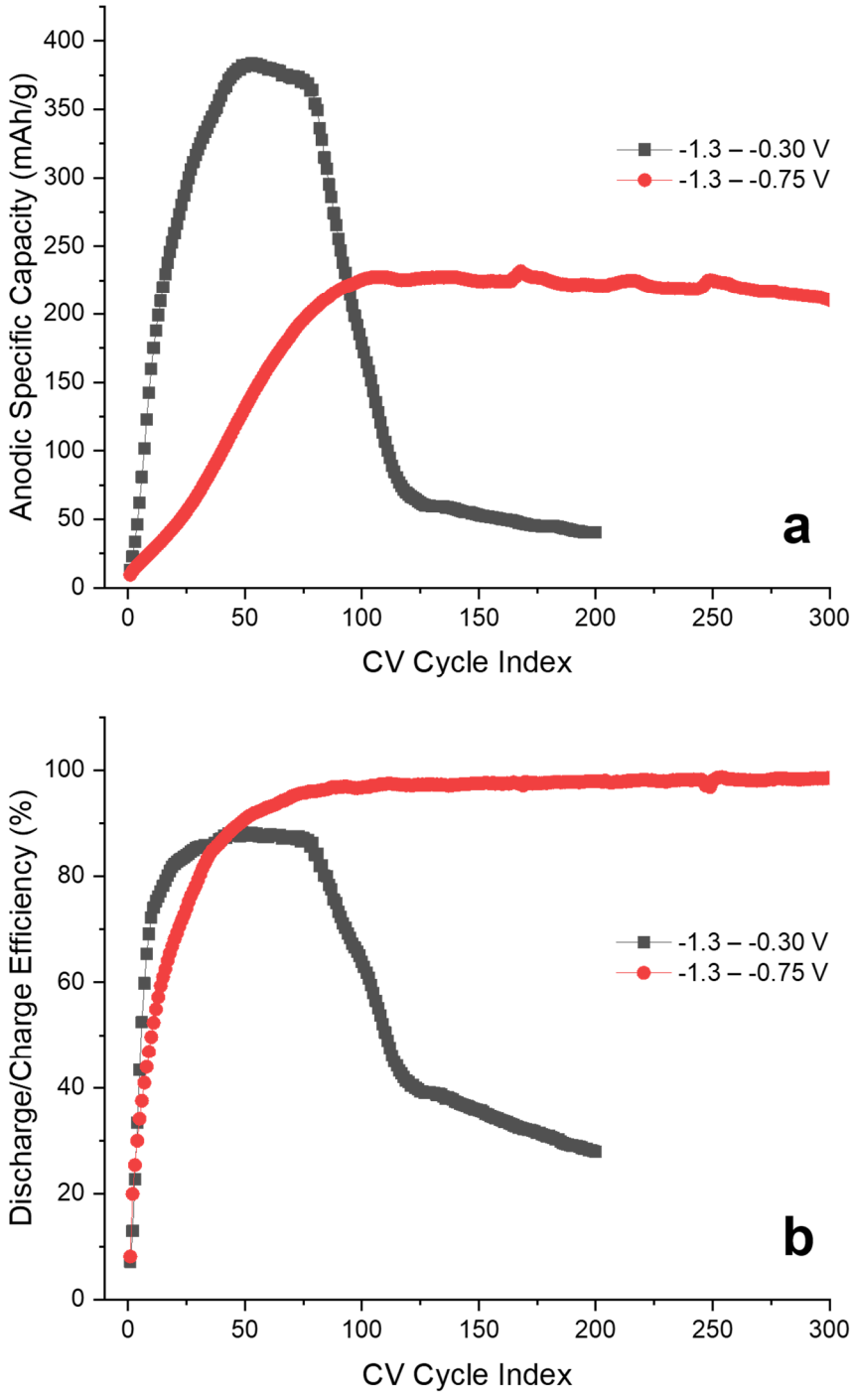

Figure 30. Shallow discharge vs. Ch3Ref: (a) anodic specific capacity and (b) discharge/charge efficiency.

XRD results did not show any phases other than α-Fe (Figure 31), which was expected by Figure 29 with no Ox2 peak. Coupled with Figure 30b, they also tell that Fe-to-Fe(II) transition is highly reversible. Moreover, Figure 31 can be the evidence showing that the sample preparation method for post-mortem analysis, including washing and drying, was free from the possible oxidation problem of Fe anodes.

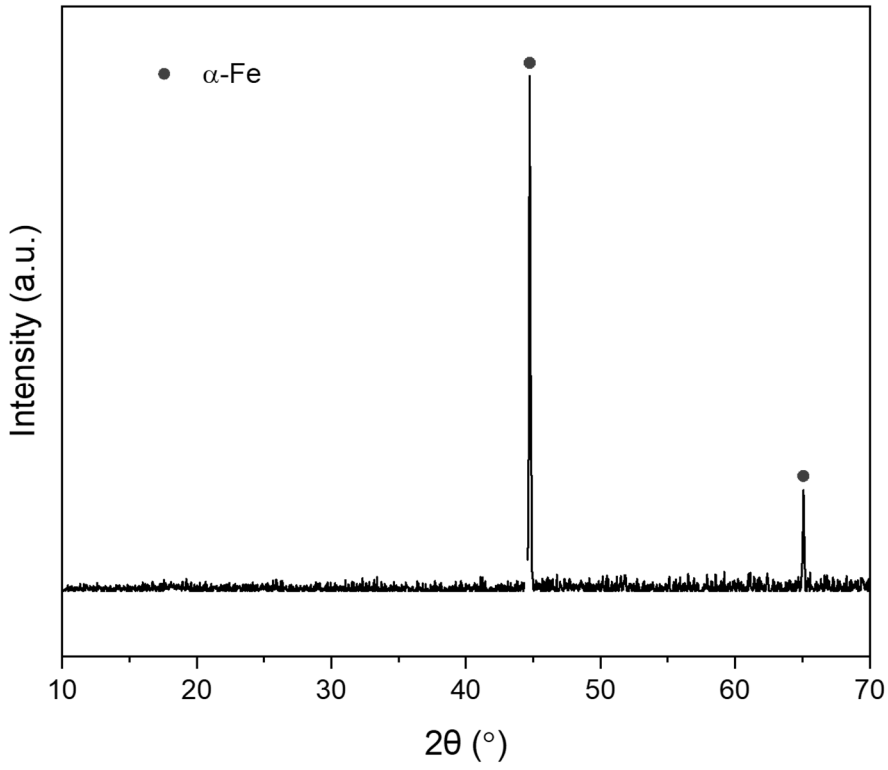

Figure 31. XRD spectra of cycled Fe anode with -0.75 V as discharge cut-off potential after 300 cycles. Note that the spectra of Ni current collectors were removed to improve legibility.

As confirmed in XRD results, the characteristic octahedral shape of γ-Fe_2O_3 particles was not observed in the cycled electrode. Along with the unchanged phase, the morphology of Fe particles maintained the original spherical shape even after 300 cycles (Figure 32a).

SEM observations also confirmed that the shallow discharge formed a colony of grains at the entire particle surface. They are the iron grains into which the original surface of mother particles turned, rather than the deposition or precipitation newly formed, because i) no evolution of new phase(s) was confirmed in XRD results and ii) the same structure was found inside the particles as well (Figure 32b). Considering the capacity growth with increasing discharge overpotential and HER current during the initial stage (Figure 29a), the following conclusions are drawn for the case of shallow discharge:

i) The "particle division" gradually takes place from surface to core during the development stage, which increases the active surface area of Fe electrode.

ii) The more the cycling progresses, the deeper the hydroxide anions diffuse inside of Fe particle, which turns whole volume of particle into nano-sized grains.

iii) After the particle is fully segmented (i.e., maximized surface area), the redox reactions occurring at the grain surface/boundary delivers a constant capacity with no significant changes in phase and morphology.

More importantly, SEM observations revealed certain information on different diffusion processes involved in Ox1 and Ox2. In contrast to the drastic particle fragmentation Ch3Ref showed from the initial stage (Figure 20), the grains formed by shallow discharge did not fall apart maintaining the integrity of particle (Figure 32a). In addition, the electrode surface of Ch3Ref was entirely covered by the precipitation including γ-Fe_2O_3 octahedra, whereas the shallow discharge sample showed most of Fe particles buried in the electrode matrix, which is the same as the condition of pristine Fe anodes before cycling (50 cycles, Figure 22 vs. 300 cycles, Figure 32c). Since the nature

of both Fe-to-Fe(II) and Fe(II)-to-Fe(III) transitions is founded on the dissolution-precipitation mechanism, a diffusion process of dissolved species may take place in the middle of either or both. Based on the aforementioned observations, one can deduce that Ox1 does not involve the diffusion of dissolved species in the two-step reaction (dissolution-precipitation), whereas Ox2 consists of three processes: dissolution-diffusion-precipitation. It is plausible that the diffusion of ferrite intermediates of Ox1 ($HFeO_2^-$ in Reaction 1-1 and 1-2) is kinetically limited by their adsorption and/or electro-sorption at the surface of electrodes. The precipitation observed in Chapter 3 is believed to be done by diffused intermediates of Ox2 though further study is required to comprehensively identify them. Such intermediates may have minor contribution to the capacity loss Ox2 brings if they unfavorably form the precipitates that do not participate in electrochemical reactions or that show extremely small capacities.

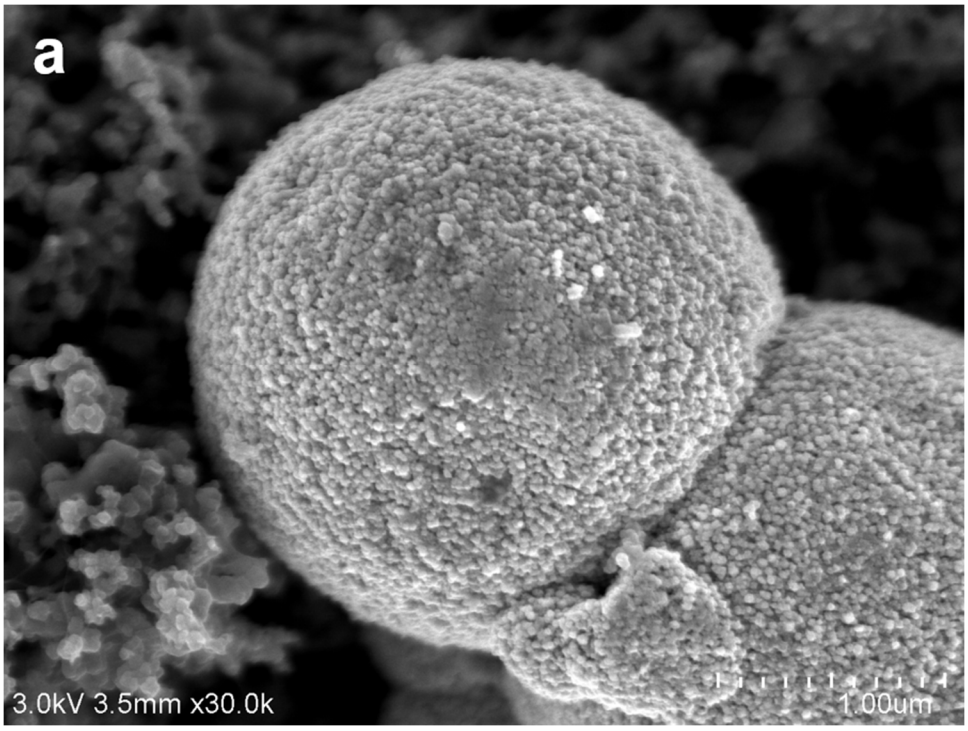

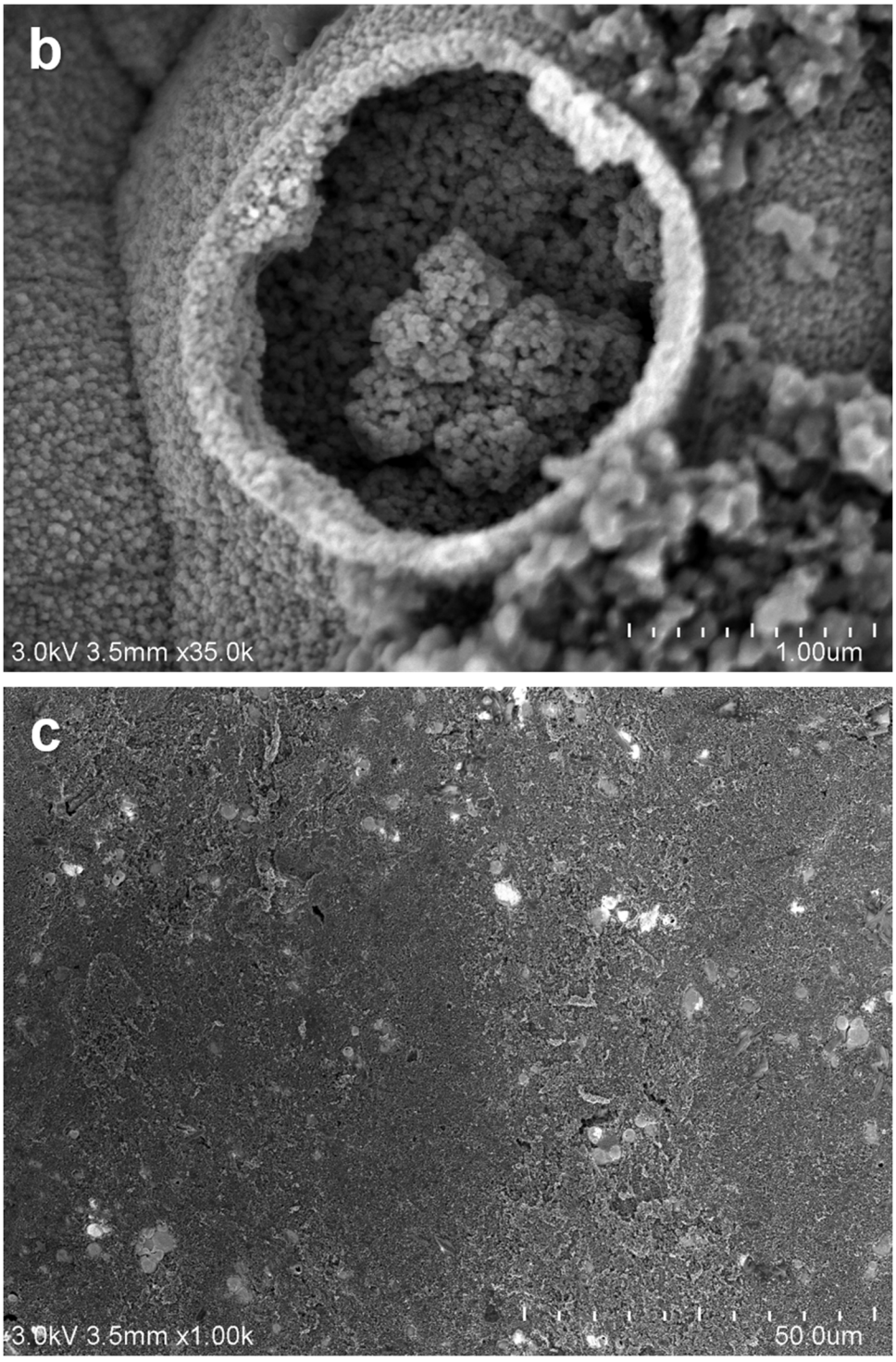

Figure 32. SEM images of cycled Fe anode with -0.75 V as discharge cut-off potential after 300 cycles. All panels were acquired from the same electrode. The structure in panel b was obtained from the breakage of oligomer-shaped Fe particle.

4.2 Electrolyte Concentration

High concentration of electrolytes brings benefit to rechargeable alkaline batteries: higher conductivity and reduced hydrogen evolution. The latter is achieved by the Nernst equation for Reaction 8.

$2H_2O + 2e^- \rightarrow H_2 + 2OH^-$ ($E° = -0.93$ V vs. Hg/HgO) (8)

$$E = E° - \frac{RT}{F}\log[OH^-]$$

High molarity of hydroxide anions makes the potential for hydrogen evolution more negative, which lowers the HER current at the potential range for charging Fe anodes. Consequently, a certain amount of electrical charge, which was supposed to be consumed by HER becomes, can be supplied to the charge reaction of Fe anodes (Red1), making charging efficiency higher.

As nearly saturated electrolytes were used in Chapter 3 (8M KOH + 1M LiOH), lower concentration but the same composition was studied to investigate the impact of electrolyte concentration on Fe anodes in alkaline conditions. Compared to the case of Ch3Ref, the concentration was scaled down to an eighth and an eightieth.

Adjustment: 8M KOH + 1M LiOH → 1M KOH + 0.125M LiOH ("1M sample")

Adjustment: 8M KOH + 1M LiOH → 0.1M KOH + 0.0125M LiOH ("0.1M sample")

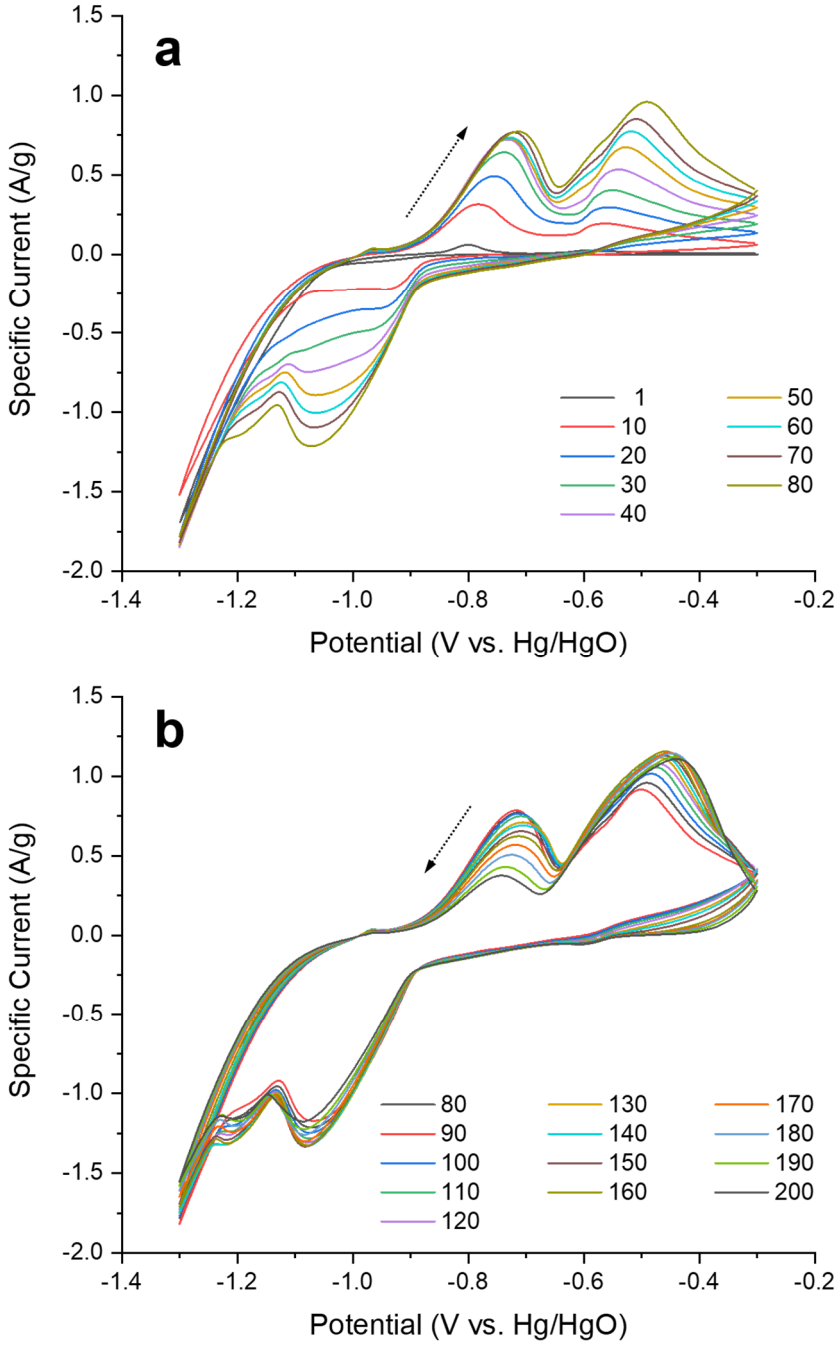

Figure 33. CV curves with 1M KOH + 0.125M LiOH: (a) 1st – 80th and (b) 80th – 200th. The first and every tenth cycles were presented. The direction of arrows indicates the progress of cycling.

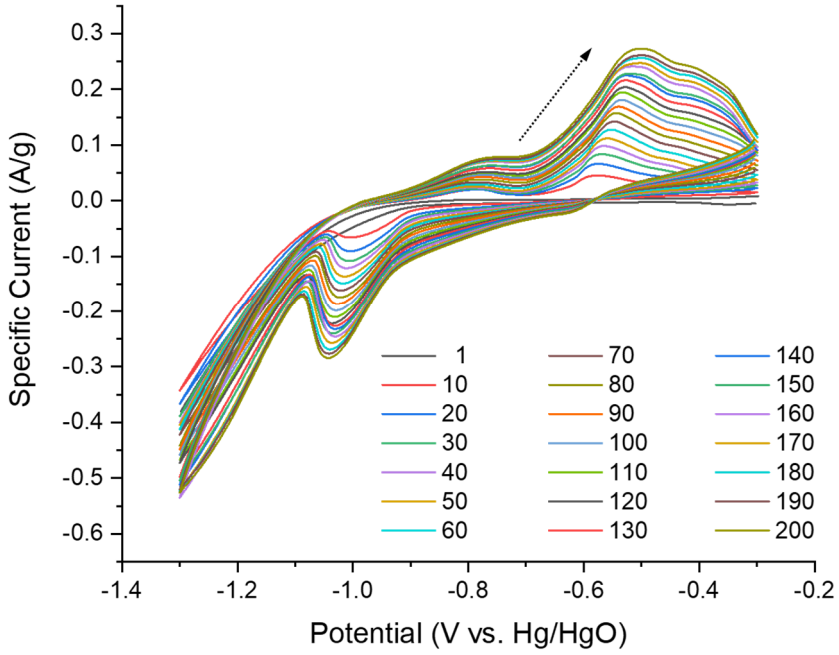

Figure 34. CV curves with 0.1M KOH + 0.0125M LiOH. The first and every tenth cycles were presented. The direction of arrows indicates the progress of cycling.

Compared to 8M sample (Ch3Ref), 1M sample exhibited the limited growth of Ox1 and its early decline from the 80th cycle while Ox2 remained active (Figure 33). Such a phenomenon was intensified for 0.1M sample showing more suppressed Ox1 than that of 1M sample (Figure 34). In addition, when comparing Figure 33 with Figure 34, it was found that the lower the electrolyte concentration is, the less the current is drawn by CV. Therefore, some conclusions about electrolyte concentration can be reached:

i) The availability of hydroxide anions influences the overall reactivity of Fe anodes in respect of their capacity in alkaline batteries.

ii) The effect of electrolyte concentration on the Fe anode reactivity is stronger for Ox1 than Ox2.

The impact of electrolyte concentration on the overall capacity of Fe anodes is presented in (Figure 35a). The lower the electrolyte concentration was, the lower the delivered capacity was and the slower the evolution of Fe anodes was. If the same model of Ch3Ref can be applied to other samples, 1M sample is regarded to undergo the development, retention and fading stages over 200 cycles while 0.1M sample is still in the development stage.

Reaction 1-1 may be the reason why Ox1 is more sensitive to the electrolyte concentration effect than Ox2. If the formation of ferrite intermediates ($HFeO_2^-$) demands high concentration of hydroxides more than any other reaction does, it can be limited under the low alkali condition.

Interestingly, HER current was reduced at lower electrolyte concentration (Figure 33 vs. Figure 34), which is contrary to the expectation of Nernst equation. In this system, the effect of conductivity is considered to be stronger than that of HER potential shift.

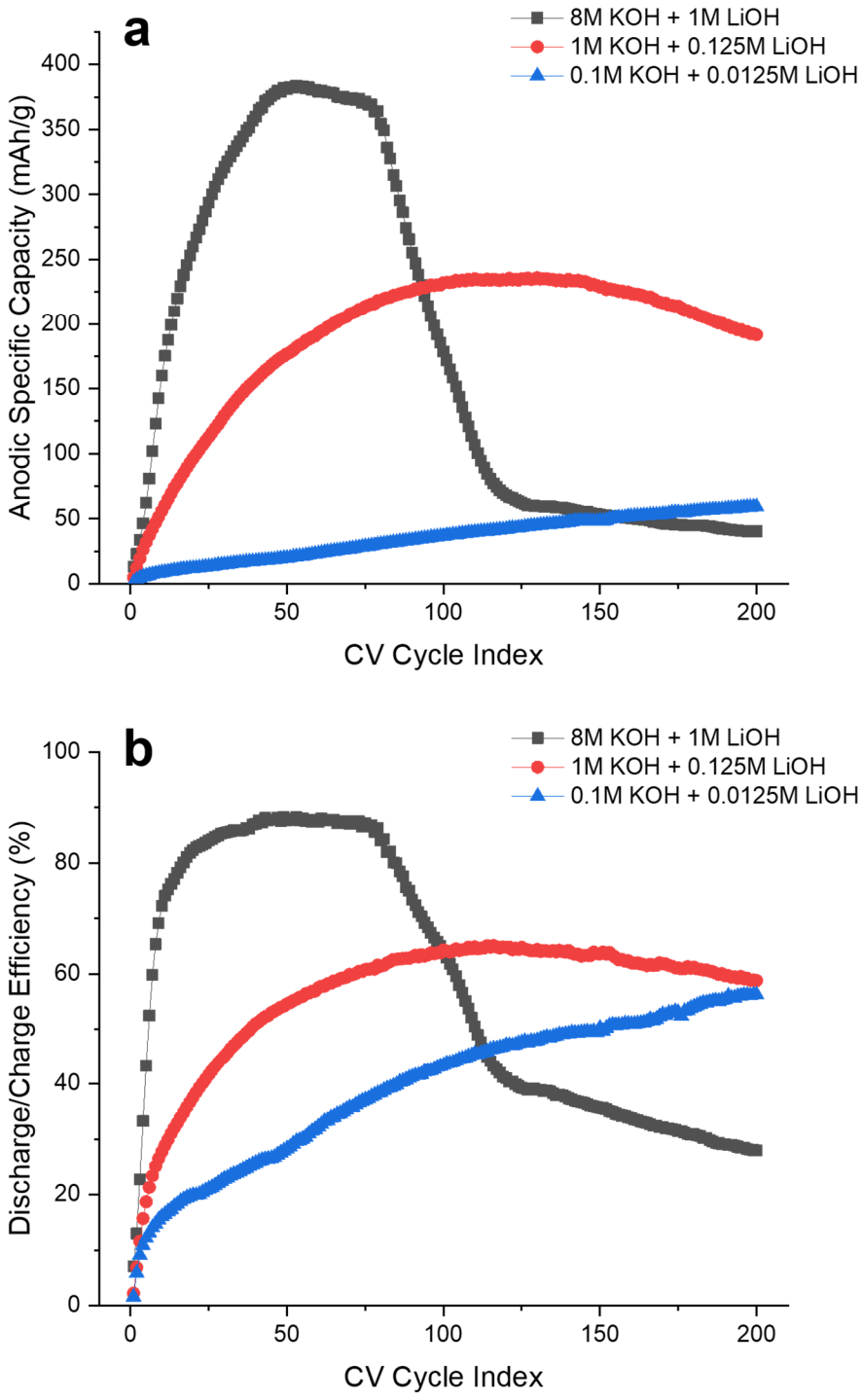

Figure 35. Effect of electrolyte concentration on (a) anodic specific capacity and (b) discharge/charge efficiency.

Under the situation of suppressed Ox1, the formation of $Fe(OH)_2$ may lead to a short supply of the reactants for Ox2. Figure 33 and Figure 34, however, refute it by showing larger Ox2 peaks regardless of the evolution condition of Ox1 peaks. This implies that one of the sources of Ox2 might be Fe-to-Fe(III) oxidation reaction (i.e., direct oxidation from metallic Fe), which was discussed in Chapter 2.4. Although other reagents can be suggested for Ox2, it is clear that the formed $Fe(OH)_2$ by Ox1 becomes further oxidized into γ-Fe_2O_3 because the XRD could not detect $Fe(OH)_2$ (or any new phase other than α-Fe and γ-Fe_2O_3) from the cycled anodes (Figure 36).

XRD results also tell that more metallic Fe remained when cycled in lower concentration of electrolytes. Such results follow the previous discussion made with Figure 35a. Compared to 1M sample, 0.1M sample delivered far less capacity at each cycle and exhibited more sluggish evolution of electrodes, leading to the slow consumption of starting electrode materials.

SEM observations showed an insignificant difference between 1M and 0.1M samples at the 200^{th} cycle (Figure 37). Most of particles display an amorphous shape but in part possessing the octahedral structure. This can be explained by the different local conditions at EEI when oxidizing Fe anodes.[77, 94] The excess of OH^- (provided by 8M sample) results in higher local pH inducing the surface of growing particles to be charged. It eventually enables the particle growth by molecular addition (Figure 23a). In contrast, if the surface has the excess of Fe^{2+} dissolved (provided by 1M or 0.1M sample, relatively), the local pH can be close to the isoelectric point of iron oxides allowing the aggregation of minuscule primary particles into spheres (Figure 37).

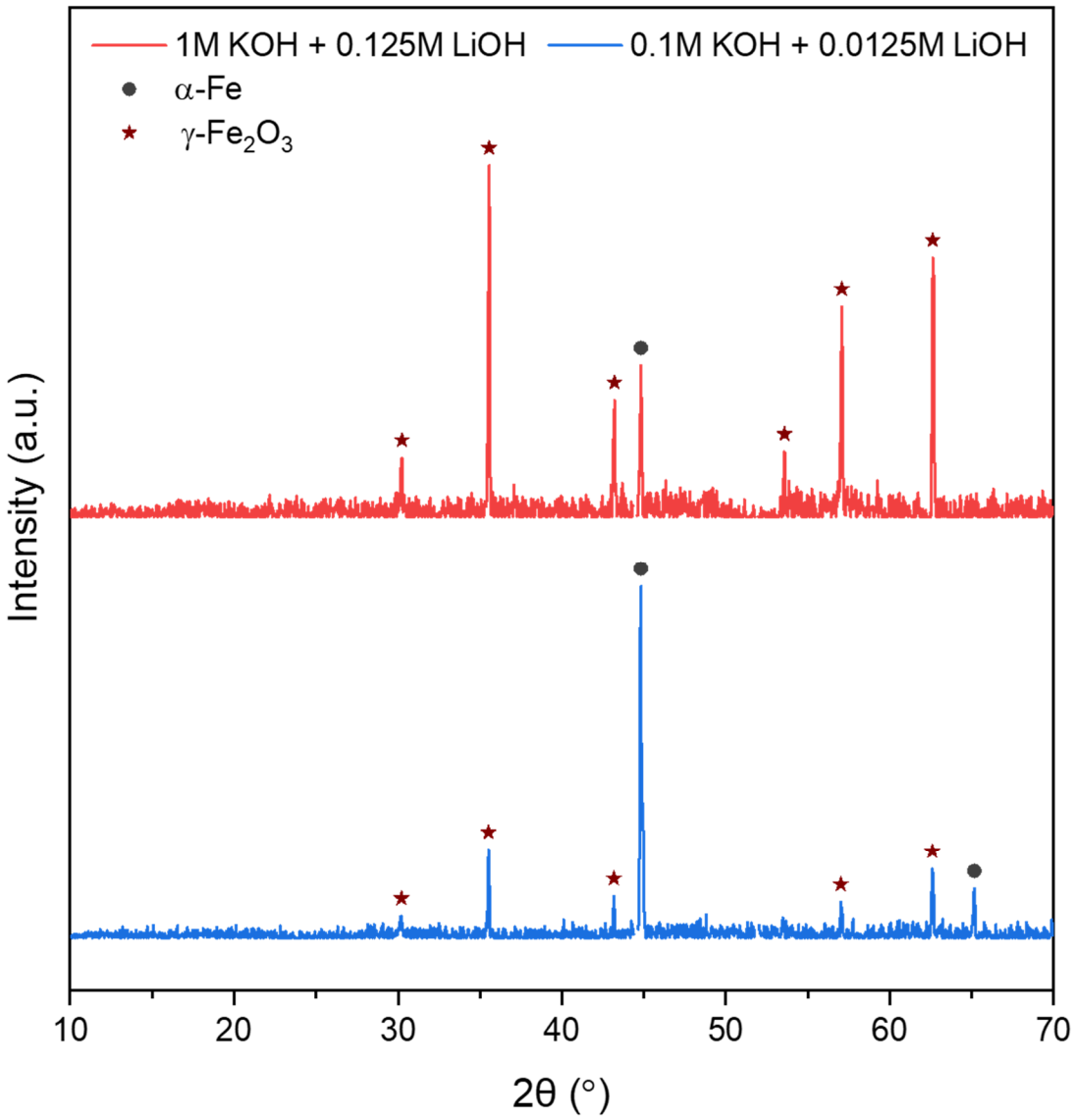

Figure 36. XRD spectra of cycled Fe anodes in 1M KOH + 0.125M LiOH (red) and 0.1M KOH + 0.0125M LiOH (blue) after 200 cycles. Note that the spectra of Ni current collectors were removed to improve legibility.

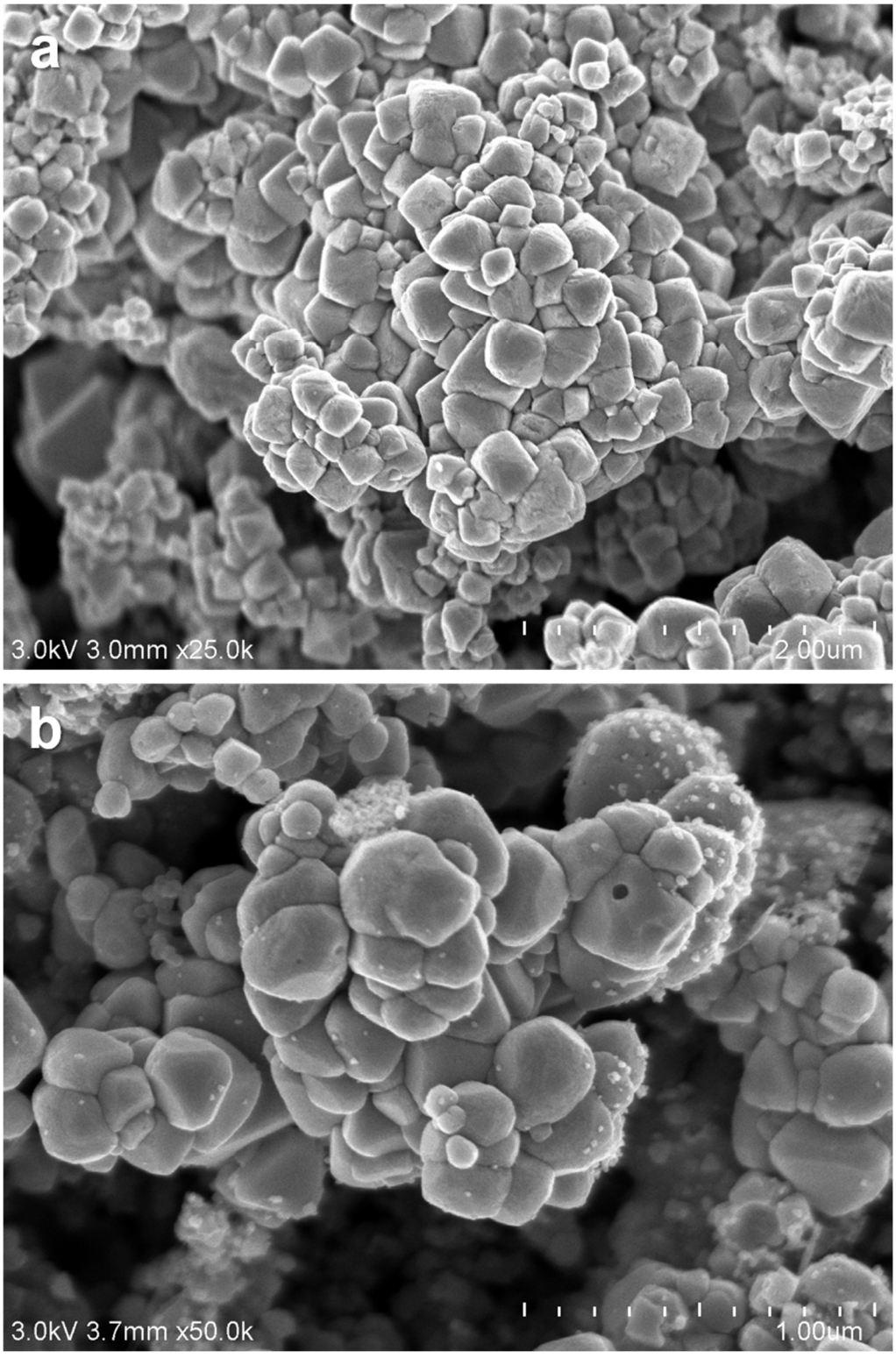

Figure 37. SEM images of cycled Fe anodes in (a) 1M KOH + 0.125M LiOH and (b) 0.1M KOH + 0.0125M LiOH after 200 cycles.

4.3 Scan Rate

In the potential sweep experiments such as CV, concentration gradient, which determines faradaic current, depends on the expansion rate of diffusion layer (thickness = $\sqrt{2Dt}$) and the concentration of analyte at electrode surface (C(0,t)). When the scan rate for CV is raised, the expansion rate of diffusion layer does not change, whereas the surface concentration of analyte decreases faster. Therefore, the concentration gradient in diffusion layer increases leading to an increase in faradaic current. Based on its definition, non-faradaic current also increases with faster scan rate. Overall, the measured current in CV, the sum of faradaic and non-faradaic current, increases when faster scan rate is applied.

Since the Nernstian behavior is hardly expected for the Fe anodes in alkaline conditions and the obtained CV curves dynamically change every cycle, applying theoretical equations to this system does not give reliable or meaningful results. The adjustment on scan rate, however, can provide the information on the electrochemical behavior of Fe anodes under the different current density of charge-discharge because the scan rate is one of the factors controlling the current in voltammetry. By increasing the scan rate ten-fold, the high-rate property of Fe anodes was examined.

Adjustment: 0.5 mV/s → 5 mV/s

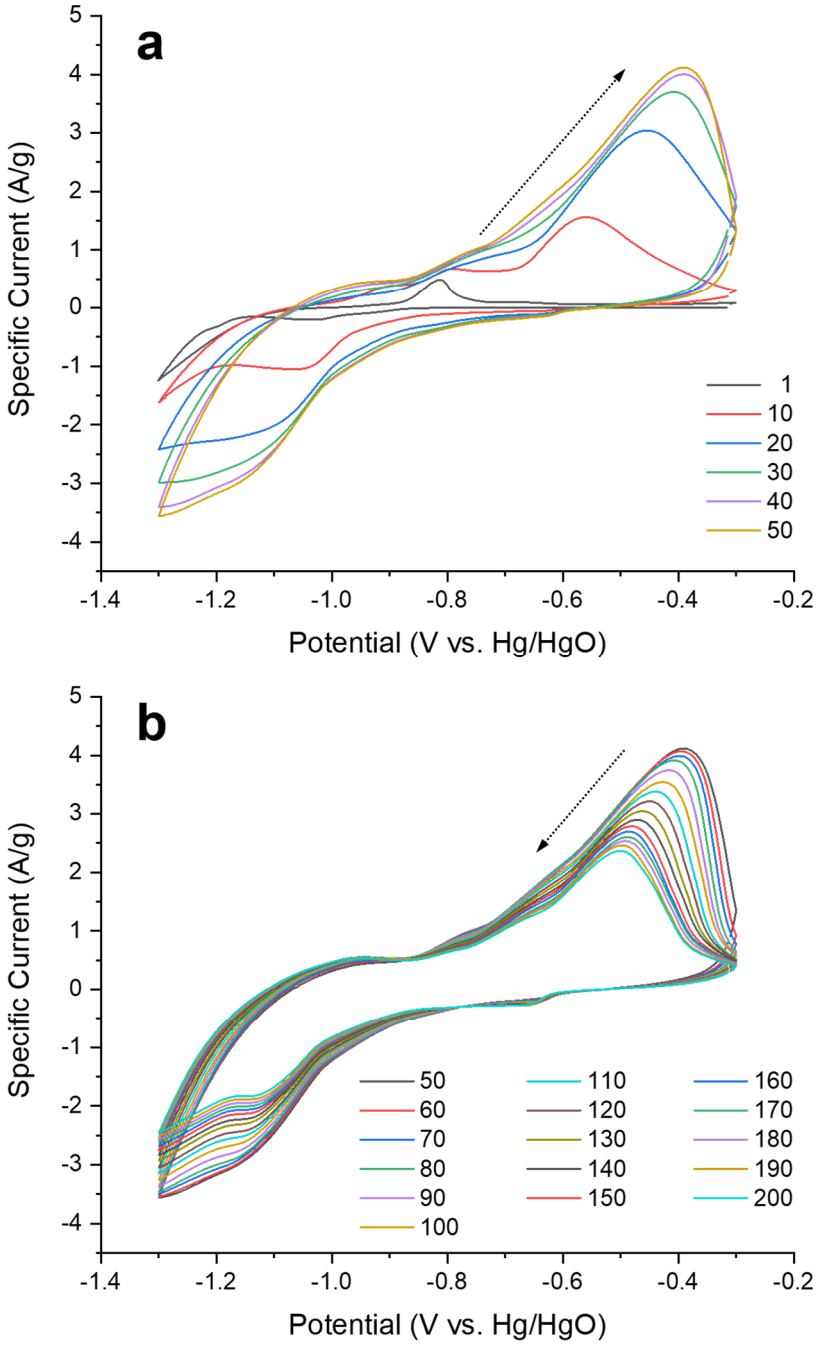

Figure 38. CV curves with 5 mV/s: (a) 1st – 50th and (b) 50th – 200th. The first and every tenth cycles were presented. The direction of arrows indicates the progress of cycling.

As expected, Figure 38 shows that the overall current of the fast-scanned sample increased from that of Ch3Ref (Figure 19). Similar to the sample with low electrolyte concentration (Figure 34), the fast-scanned sample exhibited remarkably suppressed Ox1 growth. This means that the Fe-to-Fe(II) oxidation reaction, which has a major contribution to capacity, takes place only at sufficiently low rates. If the sweet spot is assumed as 0.5 mV/s (≈ 30 min for charge or discharge), any current density faster than 2C would lose most of anode capacity though such estimation is highly rough.

Another notable difference of the fast-scanned sample from Ch3Ref is the reaction potentials. For example, a prominent Ox2 peak of the fast-scanned sample was placed at -0.4 V vs. Hg/HgO (Figure 38), whereas the corresponding peak of Ch3Ref stood at -0.6 V vs. Hg/HgO (Figure 17). In other words, ten times faster scan rate caused a discharge overpotential increase by 0.2 V. This is also true for the coupled reduction reaction, Red2. Such phenomena indicate that the charge-discharge reactions of Fe anodes are not highly reversible under alkaline conditions. According to the literature, the ion transfer in/at Fe anodes is a rate-limiting factor for their reactions in alkaline conditions, rather than charge transfer.[37]

Despite the overpotential increase, Ox2/Red2 delivered a certain amount of capacity under the high-rate conditions. This may suggest the capacitive behavior of iron(III) oxides in alkaline conditions, which were reported by a recent few articles.[36, 38]

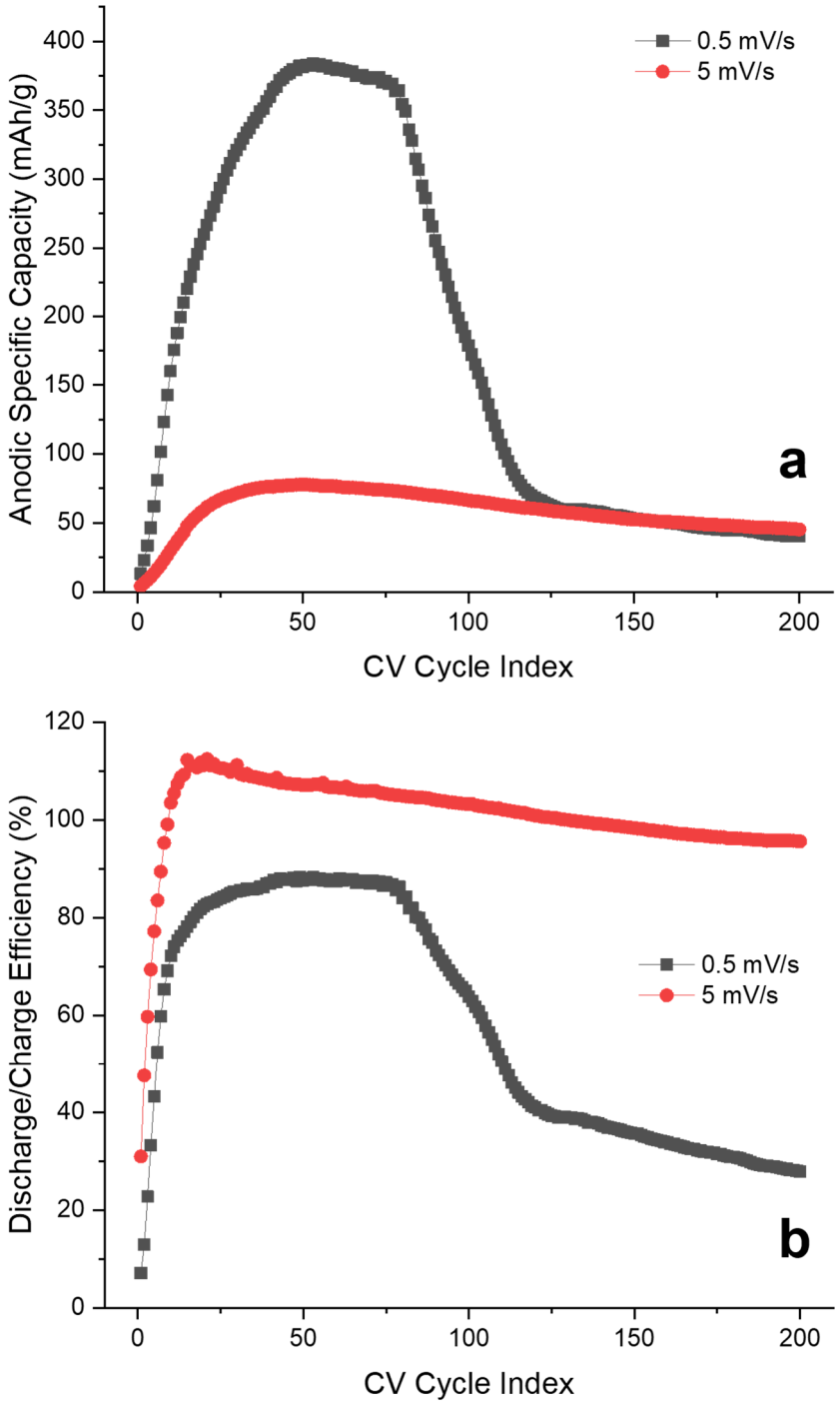

Figure 39. Effect of scan rate on (a) anodic specific capacity and (b) discharge/charge efficiency.

Although the fast-scanned sample exhibited high current in CV curves, the delivered capacity from it was small (Figure 39a) because of i) ten times higher scan rate ([mV/s] vs. [mAh/g]) and ii) the absence of Ox1. The dynamic capacity change of Ch3Ref originated from the rise and fall of Ox1.

It is noticeable that the fast-scanned sample presented the discharge/charge efficiency over 100% (Figure 39b), which means that HER was also affected by the change in scan rate. In the same manner as the charge overpotential increase for Red2, the HER overpotential was raised, which reduced the current loss taken by parasitic HER, eventually resulting in the improvement of charging efficiency. In addition, the discharge capacity delivered by Ox2 has significantly low reversibility (or irreversibility) so that the subsequent charge by Red2 could not make sufficient contribution to the charge capacity for next cycle. Then the discharge took place at another pristine (metallic) sites again, extracting relatively high discharge capacity compared to the charge capacity, simultaneously making them less-reversibly oxidized. Such "consuming" behavior led to high discharge/charge efficiency more than 100% which, however, gradually decreased as cycling progressed.

Due to low but irreversible consumption of electrode materials, relatively high amount of metallic Fe remained with the accumulation of γ-Fe_2O_3 after 200 cycles (Figure 40). SEM observations revealed the formation of amorphous particles at the surface of electrode (Figure 41). The characterization on phase and morphology tells that they are the iron oxides formed by the aggregation of minuscule primary particles via the dissolution-diffusion-precipitation route of Ox2. It is plausible that such a specific mechanism was activated by the high-rate circumstance originally induced by the fast scan rate.

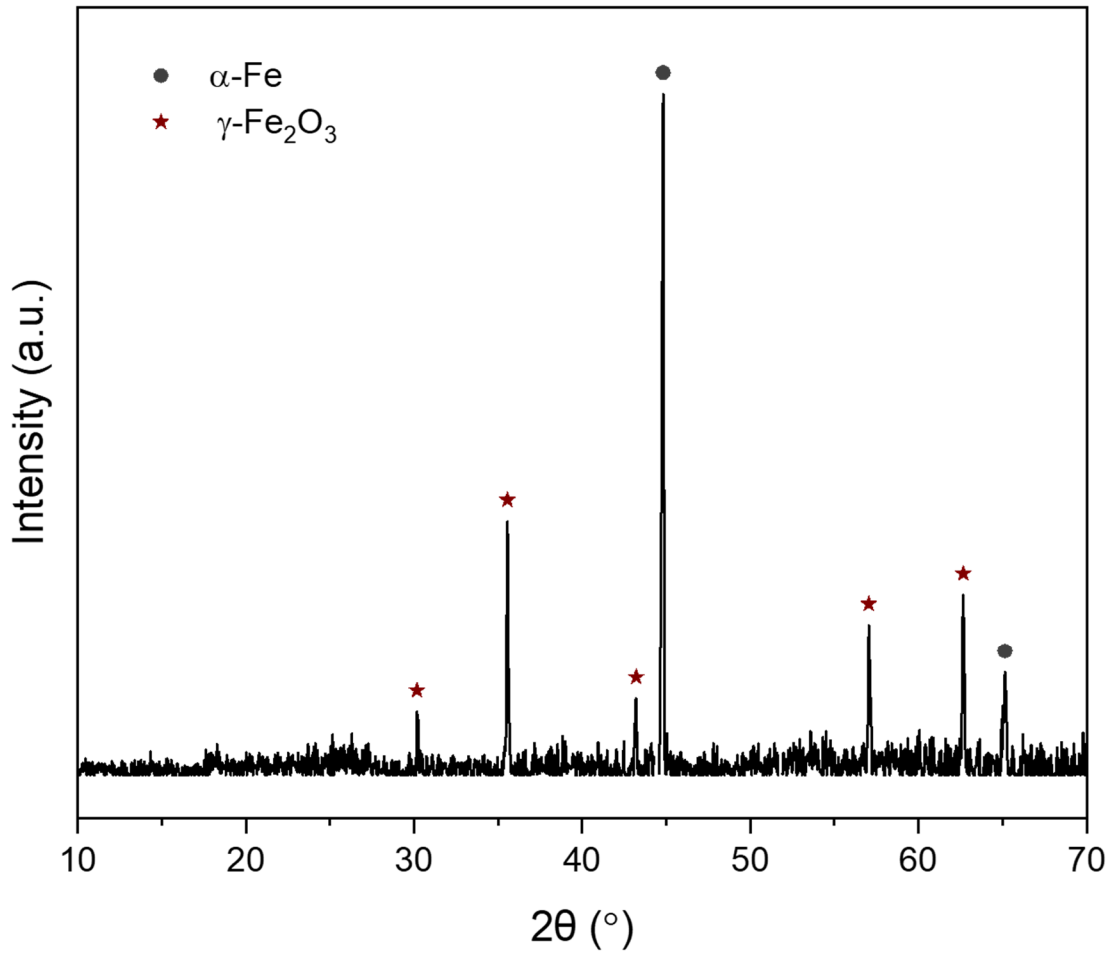

Figure 40. XRD spectra of cycled Fe anode with 5 mV/s after 200 cycles. Note that the spectra of Ni current collectors were removed to improve legibility.

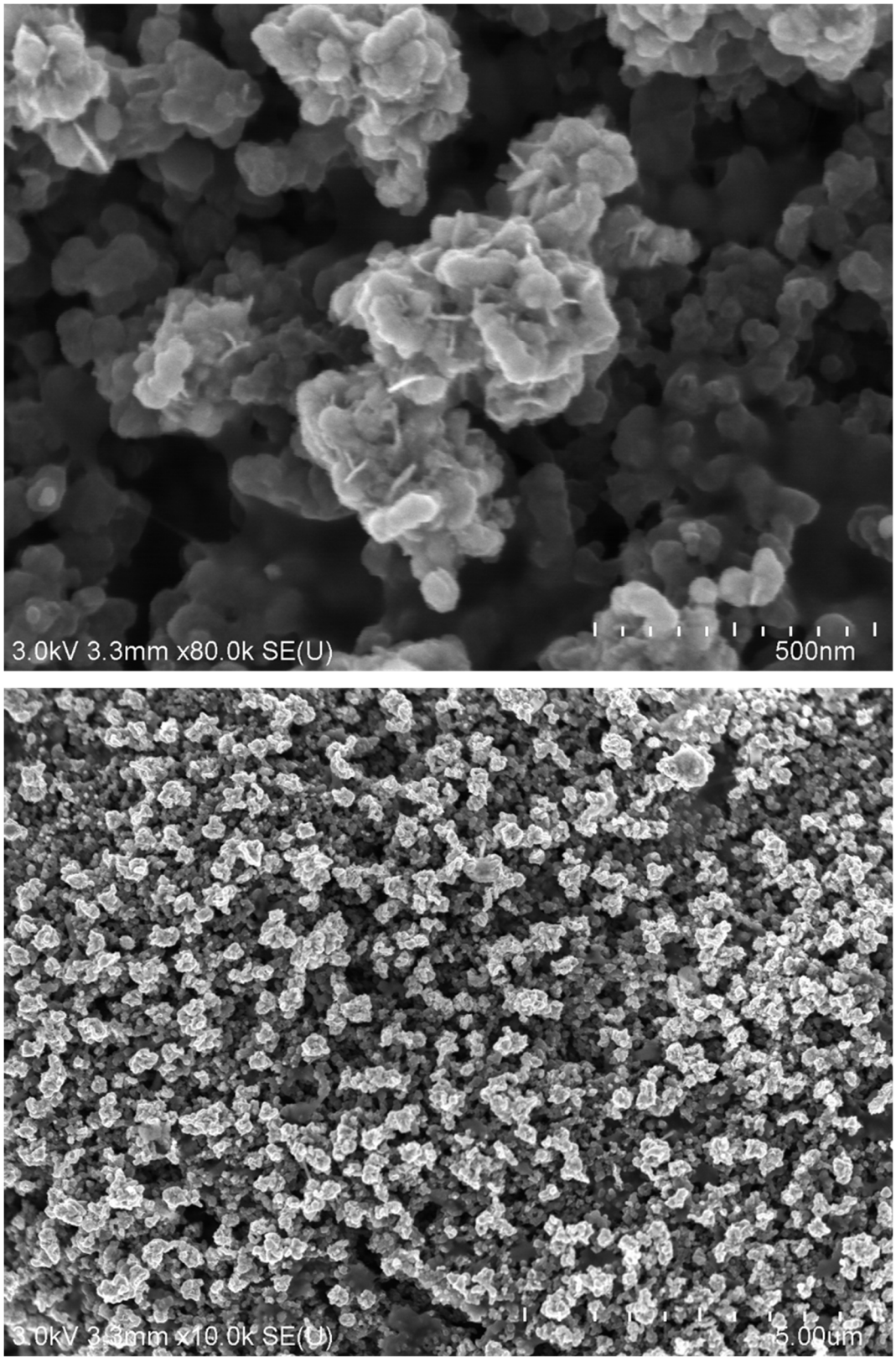

Figure 41. SEM images of cycled Fe anode with 5 mV/s after 200 cycles.

4.4 Additive Content

The effect of various additives including sulfides was previously discussed in Chapter 2.5. The erstwhile results were obtained consistently with 3 wt.% of bismuth sulfides (Bi_2S_3) added in electrodes in order to benefit from both bismuth and sulfides. In this chapter, the Fe anode with higher content of Bi_2S_3 was newly examined to investigate the electrochemical performance change. Since the carbon conducting agents occupy already high volume in the electrode matrix, the electrode composition adjustment was achieved by reducing the amount of PureBLACK to make more room for Bi_2S_3.

Adjustment: 70% of Fe, 17% of PureBLACK, 10% of PTFE and 3% of Bi_2S_3

→ 70% of Fe, 10% of PureBLACK, 10% of PTFE and 10% of Bi_2S_3

Note that this chapter does not cover the detailed mechanisms on the function of sulfide additives because it goes beyond the scope of the author's study in the aspect of experimental technique. As discussed in Chapter 2.5, they are still under discussion in academia and dependent on the systems the researchers design.

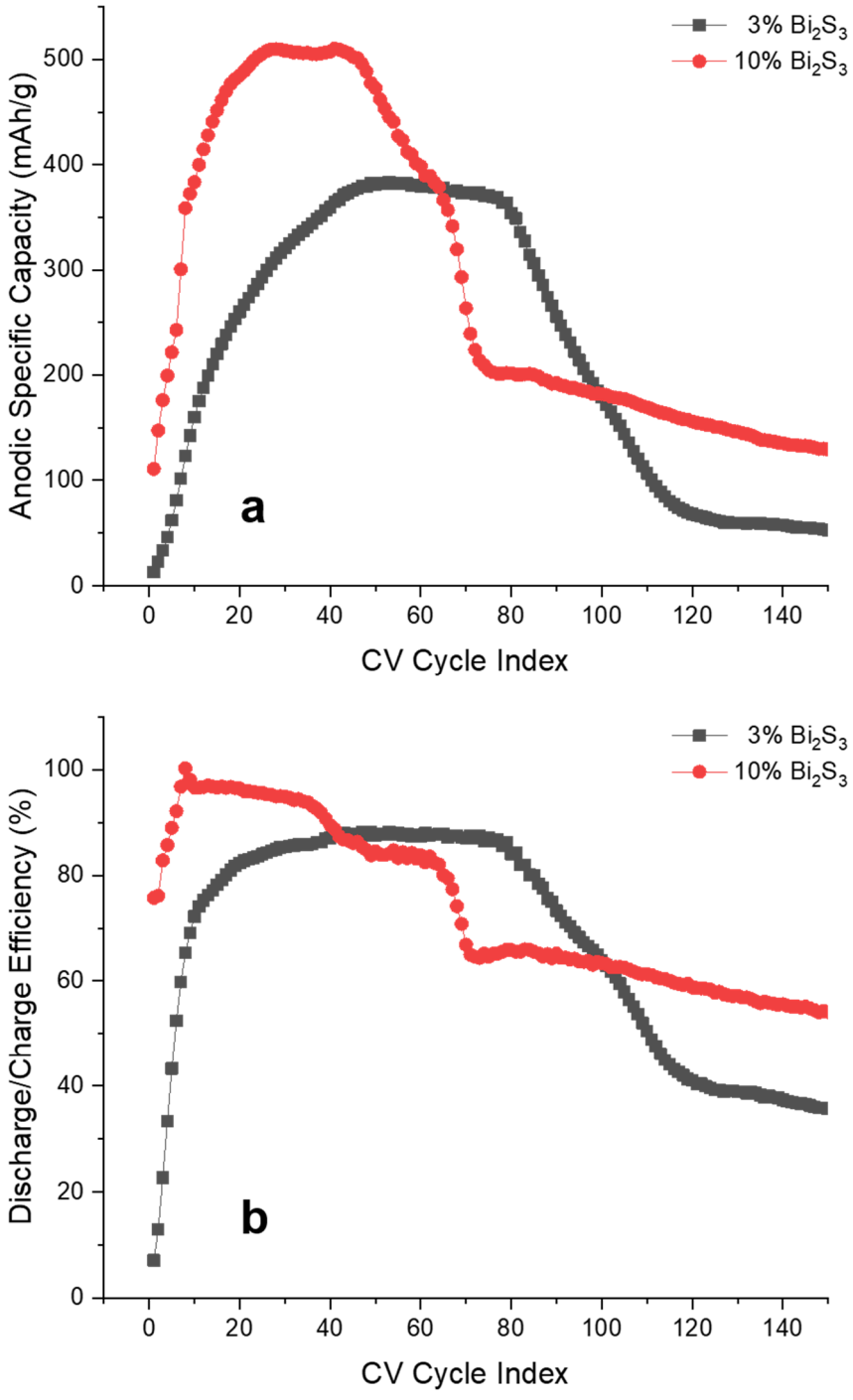

Figure 42. Effect of Bi_2S_3 content on (a) anodic specific capacity and (b) discharge/charge efficiency.

Figure 42 demonstrates that higher content of Bi_2S_3 brings benefit to the discharge capacity and discharge/charge efficiency of Fe anodes; the maxima in both were raised. The duration of such enhancement, however, becomes shorter compared to lower Bi_2S_3 content sample. The fading and failure stages came earlier (at the 50^{th} cycle) than Ch3Ref (at the 80^{th} cycle). Since Bi_2S_3 can boost the reactions of any iron species, the electrochemical behavior of Fe-to-Fe(II) and Fe(II)-to-Fe(III) transition reactions should be analyzed separately.

Except for the quantitative difference, the 10% Bi_2S_3 sample seems to well follow the model for Ch3Ref: development, retention, fading and failure (Figure 43). The retention stage in (Figure 43c), however, revealed a qualitative difference from that of Ch3Ref. The 3% Bi_2S_3 sample, Ch3Ref, maintained its capacity with no changes in both Ox1 and Ox2 during cycle 50 – 80 (Figure 19c), whereas the 10% Bi_2S_3 sample showed an increase in Ox1 with a simultaneous decrease in Ox2 during cycle 30 – 50 (Figure 43c). Although the overall anodic capacity was maintained the same, the evolution of each reaction was totally different. In the case of Ox1, it grew by the 50^{th} cycle, the same cycle by which Ch3Ref did. Higher additive content quantitatively facilitated Ox1, leading to the increase in deliverable capacity, but did not change its long-term behavior. While Ox2 also provided more capacity due to higher content of additives, it declined from the 30^{th} cycle which is fifty cycles earlier than the case of Ch3Ref. Such unexpected behavior of Ox2 may be attributed to its diffusion-involved irreversible precipitation process. Because of higher content of additives, the formation rate of γ-Fe_2O_3 augmented, which advanced its accumulation dozens of cycles. Such undesirably fast γ-Fe_2O_3 accumulation resulted in the early passivation of Fe anodes, presenting the fading stage from the 50^{th} cycle.

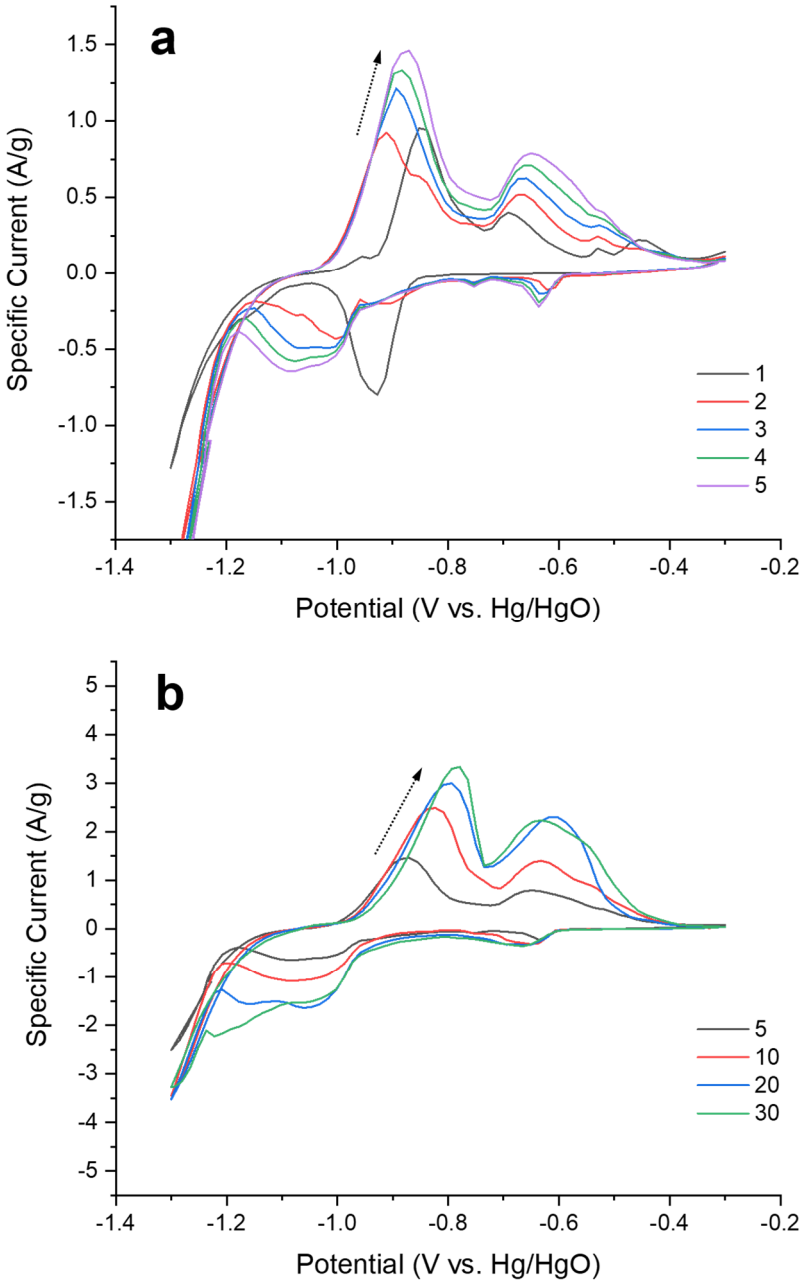

Figure 43. CV curves for Fe anode with 10% of Bi_2S_3: the (a) 1st – 5th and (b) 5th – 30th cycles. No significant change was shown in CV curves after the 80th cycle. Note that the scale of the current axis in panel a is smaller than that in the other panels. The direction of arrows indicates the progress of cycling.

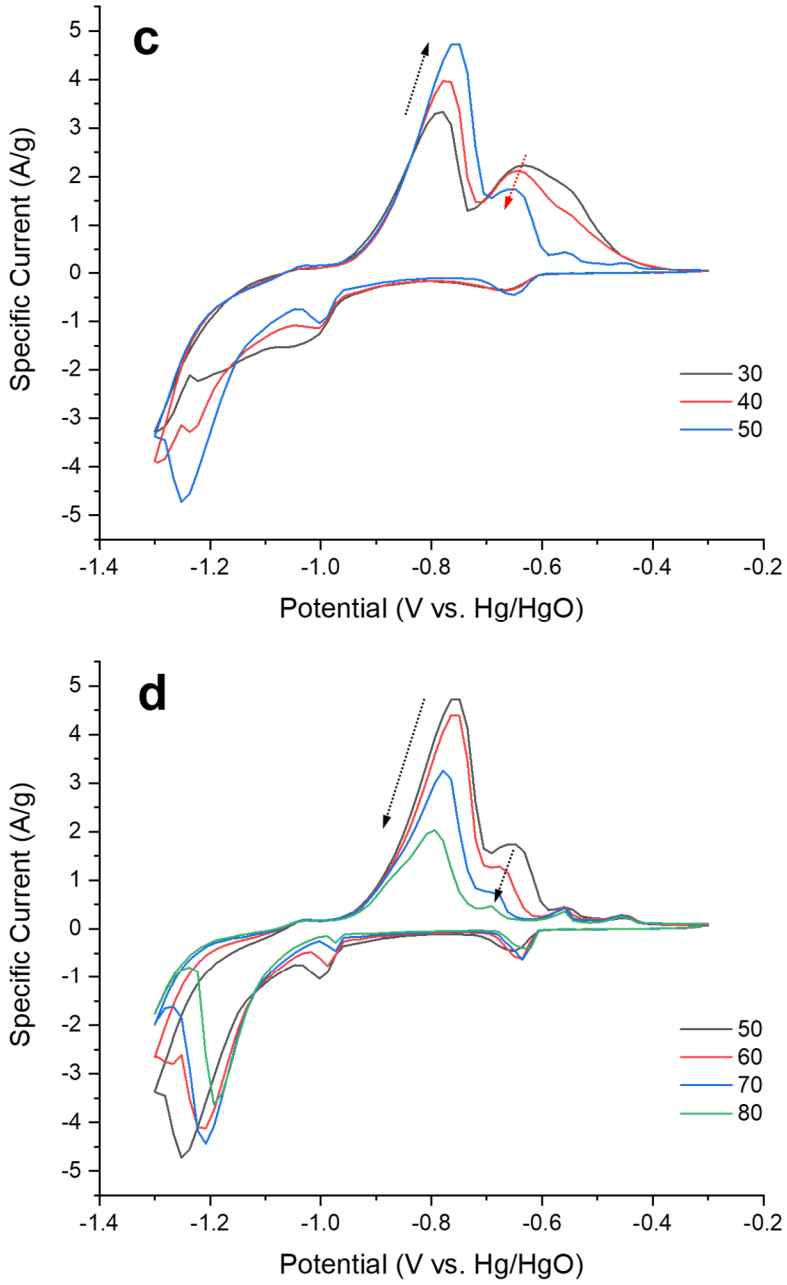

Figure 43 (ctnd.). CV curves for Fe anode with 10% of Bi_2S_3: the (c) 30th – 50th and (d) 50th – 80th cycles. No significant change was shown in CV curves after the 80th cycle. Note that the scale of the current axis in panel a is smaller than that in the other panels. The direction of arrows indicates the progress of cycling.

Compared to Figure 19a, Figure 43a presents a relatively strong reduction peak at -0.93 V vs. Hg/HgO. Considering the peak height and reaction potential, it is regarded as the bismuth reduction reaction from Bi_2S_3, rather than the Red2 in the 1st cycle.

$$Bi_2S_3 + 6e^- \leftrightarrow 2Bi + 3S^{2-} \qquad (E° = -0.92 \text{ V vs. Hg/HgO}) \quad (20)$$

This reduction peak nearly disappeared from the 2nd cycle, which means that the initiation of the sulfide supply was carried out by the above reaction that occurred at the 1st cycle. The same reaction could be expected for Ch3Ref, but the peak was not detected from the CV results (Figure 19a) because of its low content of Bi_2S_3.

Another reduction peak is confirmed at -0.65 V vs. Hg/HgO at every cycle except for the 1st cycle. Also, the peak height (area) is proportional to the content of Bi_2S_3. Since the standard reduction potential of Bi reduced from Bi_2S_3 is far more cathodic then -0.65 V (Reaction 20), this small peak can be attributed to the Bi reduction reaction from Bi_2O_3.

$$Bi_2O_3 + 3H_2O + 6e^- \leftrightarrow 2Bi + 6OH^- \qquad (E° = -0.56 \text{ V vs. Hg/HgO}) \quad (21)^{55}$$

Therefore, Bi_2S_3 provides Fe anodes with the sulfides anions at the 1st charge by Equation 20, but the remaining bismuth undergoes a reversible redox reaction according to Equation 21 during the rest of cycles. The corresponding oxidation could be hardly observed in CV because of the overlap with Ox2, but its buried peak was eventually disclosed at -0.56 V vs. Hg/HgO after Ox2 declined (Figure 43c,d).

CHAPTER 5. CONCLUSION AND RECOMMENDATION

5.1 Conclusion

This study correlated the changes in the electrochemical behavior of micro-scale Fe upon deep cycling in alkaline conditions with the changes in its morphology and phase. CV identified that Fe anodes undergo four stages classified by the capacity and efficiency changes during the charge-discharge cycling: development (Stage I), retention (Stage II), fading (Stage III) and failure (Stage IV). By conducting the analyses using SEM, XRD and Raman spectroscopy, it was found that each stage is associated with very specific changes in the morphology and phase of Fe anodes. From the initial cycles, we observed the Fe particle fragmentation caused by the surface-limited charge-discharge reactions. The gradual increase in surface area led to developing capacity, which was maximized at the end of Stage I. During Stage II, the capacity decay was very slow while we observed the initiated formation of γ-Fe_2O_3 octahedral monocrystalline particles. The accumulation and aggregation of γ-Fe_2O_3 led to the subsequent rapid capacity fading (Stage III) and eventual failure (Stage IV). Electrochemical tests confirmed low electrochemical activity of γ-Fe_2O_3 in alkaline media. The electrochemical reactions occurring at Fe anodes were composed of multi-step redox processes, involving the dissolution and precipitation of evolving phases as well as the diffusion of dissolved intermediates.

In addition to the base study on Fe anodes in alkaline conditions, the extended research observed how the individual factor in cell operation influences the electrochemical behavior, morphology evolution and phase transition of electrodes. On the basis of experimental conditions applied in the base study, a variety of components were

independently adjusted: potential range, electrolyte concentration, scan rate, and additive content. By analyzing the changes in CV results, SEM images and XRD spectra, the effect of each factor on cell operation was comprehensively examined. The author hopes that this study will be a cornerstone for both the fundamental understanding of Fe anodes in alkaline conditions and its performance improvement in rechargeable alkaline batteries.

5.2 Recommendation for Future Study

Although the formation of γ-Fe_2O_3 was discovered, the details of Fe(II)-to-Fe(III) transition need to be studied in depth, especially for its reaction pathways and intermediate species. Since those for Fe-to-Fe(II) transition were already known, this enables us to get a complete understanding of the full extent of Fe anode reactions in alkaline conditions. Also, it is highly possible that the different phenomena found between Fe-to-Fe(II) and Fe(II)-to-Fe(III) transitions, which was discussed in Chapter 4.1, originate from the difference of intermediates. The intermediates of Fe-to-Fe(II) transition are ferrite anions ($HFeO_2^-$) so that the research on those of Fe(II)-to-Fe(III) should consider complex ions and solvation, rather than simply treating Fe^{2+} anions as intermediates. Developing the experiment systems for in operando characterization is necessary to perform such type of research.

REFERENCES

[1] Yang, B.; Malkhandi, S.; Manohar, A. K.; Prakash, G. K. S.; Narayanan, S. R. Organo-Sulfur Molecules Enable Iron-Based Battery Electrodes to Meet the Challenges of Large-Scale Electrical Energy Storage. *Energy Environ. Sci.* **2014**, *7*, 2753-2763.

[2] Manohar, A. K.; Malkhandi, S.; Yang, B.; Yang, C.; Prakash, G. K. S.; Narayanan, S. R. A High-Performance Rechargeable Iron Electrode for Large-Scale Battery-Based Energy Storage. *J. Electrochem. Soc.* **2012**, *159*, A1209-A1214.

[3] Chaurey, A.; Deambi, S. Battery Storage for PV Power Systems: An Overview. *Renewable Energy* **1992**, *2*, 227-235.

[4] Birch, F. Density and Composition of Mantle and Core. *J. Geophys. Res.* **1964**, *69*, 4377-4388.

[5] Morard, G.; Siebert, J.; Andrault, D.; Guignot, N.; Garbarino, G.; Guyot, F.; Antonangeli, D. The Earth's Core Composition from High Pressure Density Measurements of Liquid Iron Alloys. *Earth. Planet. Sci. Lett.* **2013**, *373*, 169-178.

[6] Huang, C. L.; Vause, J.; Ma, H. W.; Li, Y.; Yu, C. P. Substance Flow Analysis for Nickel in Mainland China in 2009. *J. Cleaner Prod.* **2014**, *84*, 450-458.

[7] Oxley, A.; Barcza, N. Hydro-Pyro Integration in the Processing of Nickel Laterites. *Miner. Eng.* **2013**, *54*, 2-13.

[8] Shukla, A. K.; Venugopalan, S.; Hariprakash, B. Nickel-Based Rechargeable Batteries. *J. Power Sources* **2001**, *100*, 125-148.

[9] Vijayamohanan, K.; Balasubramanian, T. S.; Shukla, A. K. Rechargeable Alkaline Iron Electrodes. *J. Power Sources* **1991**, *34*, 269-285.

[10] Chakkaravarthy, C.; Periasamy, P.; Jegannathan, S.; Vasu, K. I. The Nickel Iron Battery. *J. Power Sources* **1991**, *35*, 21-35.

[11] McKerracher, R. D.; de Leon, C. P.; Wills, R. G. A.; Shah, A. A.; Walsh, F. C. A Review of the Iron-Air Secondary Battery for Energy Storage. *ChemPlusChem* **2015**, *80*, 323-335.

[12] Hertzberg, B. J.; Huang, A.; Hsieh, A.; Chamoun, M.; Davies, G.; Seo, J. K.; Zhong, Z.; Croft, M.; Erdonmez, C.; Meng, Y. S.; Steingart, D. Effect of Multiple Cation Electrolyte Mixtures on Rechargeable Zn-MnO_2 Alkaline Battery. *Chem. Mater.* **2016**, *28*, 4536-4545.

[13] Wikipedia Contributors, Nickel–Iron Battery. *Wikipedia, The Free Encyclopedia*, https://en.wikipedia.org/w/index.php?title=Nickel%E2%80%93iron_battery&oldid=828159552, **Accessed March 1, 2018**.

[14] Halpert, G. Past Developments and the Future of Nickel Electrode Cell Technology. *J. Power Sources* **1984**, *12*, 177-192.

[15] Periasamy, P.; Babu, B. R.; Iyer, S. V. Performance Characterization of Sintered Iron Electrodes in Nickel/Iron Alkaline Batteries. *J. Power Sources* **1996**, *62*, 9-14.

[16] Souza, C. A. C.; Carlos, I. A.; Lopes, M.; Finazzi, G. A.; de Almeida, M. R. H. Self-Discharge of Fe-Ni Alkaline Batteries. *J. Power Sources* **2004**, *132*, 288-290.

[17] Ojefors, L. Self-Discharge of Alkaline Iron Electrode. *Electrochim. Acta* **1976**, *21*, 263-266.

[18] Gu, W.; Yushin, G. Review of Nanostructured Carbon Materials for Electrochemical Capacitor Applications: Advantages and Limitations of Activated Carbon, Carbide-Derived Carbon, Zeolite-Templated Carbon, Carbon Aerogels, Carbon Nanotubes, Onion-Like Carbon, and Graphene. *WIREs Energy Environ.* **2014**, *3*, 424-473.

[19] Ojefors, L. Sem Studies of Discharge Products from Alkaline Iron Electrodes. *J. Electrochem. Soc.* **1976**, *123*, 1691-1696.

[20] Kalaignan, G. P.; Muralidharan, V. S.; Vasu, K. I. Triangular Potential Sweep Voltammetric Study of Porous Iron Electrodes in Alkali Solutions. *J. Appl. Electrochem.* **1987**, *17*, 1083-1092.

[21] Balasubramanian, T. S.; Vijayamohanan, K.; Shukla, A. K. Mechanisms of the Discharge of Porous-Iron Electrodes in Alkaline-Medium. *J. Appl. Electrochem.* **1993**, *23*, 947-950.

[22] Periasamy, P.; Babu, B. R.; Iyer, S. V. Cyclic Voltammetric Studies of Porous Iron Electrodes in Alkaline Solutions Used for Alkaline Batteries. *J. Power Sources* **1996**, *58*, 35-40.

[23] Micka, K.; Rousar, I. Theory of Porous Electrodes—XVIII. The Iron Electrode. *Electrochim. Acta* **1984**, *29*, 1411-1417.

[24] Dibrov, I. A.; Chervyakvoronich, S. M.; Grigoreva, T. V.; Kozlova, G. M. New Values of Thermodynamic Constants of Some Iron-Oxides. *Sov. Electrochem.* **1980**, *16*, 675-680.

[25] Tong, C. S.; Wang, S. D.; Wang, Y. Y.; Wan, C. C. A Study of the Iron Electrode Structure of Ni-Fe Cell. *J. Electrochem. Soc.* **1982**, *129*, 1173-1180.

[26] Silver, H. G.; Lekas, E. Products of Anodic Oxidation of an Iron Electrode in Alkaline Solution. *J. Electrochem. Soc.* **1970**, *117*, 5-8.

[27] Cerny, J.; Jindra, J.; Micka, K. Comparative-Study of Porous Iron Electrodes. *J. Power Sources* **1993**, *45*, 267-279.

[28] Teplinskaya, T. K.; Fedorova, N. N.; Rozentsveig, S. A. Nature of the Product of the 2nd Anodic Process on the Iron Electrode of an Alkaline Battery. *Zh. Fiz. Khim.* **1964**, *38*, 2176-2181.

[29] Salkind, A. J.; Venuto, C. J.; Falk, S. U. The Reaction at the Iron Alkaline Electrode. *J. Electrochem. Soc.* **1964**, *111*, 493-495.

[30] Andersson, B.; Ojefors, L. Slow Potentiodynamic Studies of Porous Alkaline Iron Electrodes. *J. Electrochem. Soc.* **1976**, *123*, 824-828.

[31] Ojefors, L. Temperature-Dependence of Iron and Cadmium Alkaline Electrodes. *J. Electrochem. Soc.* **1976**, *123*, 1139-1144.

[32] Demidov, A. I.; Kokhatskaya, M. S.; Chernovets, B. V. Thermodynamics of Discharge of the Negative Electrode of a Nickel-Iron Battery. *Russ. J. Appl. Chem.* **2006**, *79*, 677-679.

[33] Macdonald, D. D.; Owen, D. The Electrochemistry of Iron in 1M Lithium Hydroxide Solution at 22° and 200°C. *J. Electrochem. Soc.* **1973**, *120*, 317-324.

[34] Comisso, N.; Mengoli, G. Electrochemical Investigations on Composite Iron Electrodes. *J. Appl. Electrochem.* **2007**, *37*, 949-959.

[35] Casellato, U.; Comisso, N.; Mengoli, G. Effect of Li Ions on Reduction of Fe Oxides in Aqueous Alkaline Medium. *Electrochim. Acta* **2006**, *51*, 5669-5681.

[36] Sarkar, D.; Shukla, A.; Sarma, D. D. Substrate Integrated Nickel–Iron Ultrabattery with Extraordinarily Enhanced Performances. *ACS Energy Lett.* **2016**, *1*, 82-88.

[37] Wang, Q.; Wang, Y. Overcoming the Limiting Step of Fe_2O_3 Reduction Via In Situ Sulfide Modification. *ACS Appl. Mater. Interfaces* **2016**, *8*, 10334-10342.

[38] Liu, J. L.; Chen, M. H.; Zhang, L. L.; Jiang, J.; Yan, J. X.; Huang, Y. Z.; Lin, J. Y.; Fan, H. J.; Shen, Z. X. A Flexible Alkaline Rechargeable Ni/Fe Battery Based on Graphene Foam/Carbon Nanotubes Hybrid Film. *Nano Lett.* **2014**, *14*, 7180-7187.

[39] Kitamura, H.; Zhao, L. W.; Hang, B. T.; Okada, S.; Yamaki, J. Effect of Binder Materials on Cycling Performance of Fe_2O_3 Electrodes in Alkaline Solution. *J. Power Sources* **2012**, *208*, 391-396.

[40] Liu, Z. L.; Tay, S. W.; Li, X. Rechargeable Battery Using a Novel Iron Oxide Nanorods Anode and a Nickel Hydroxide Cathode in an Aqueous Electrolyte. *Chem. Commun.* **2011**, *47*, 12473-12475.

[41] Lemos, V. P.; da Costa, M. L.; Lemos, R. L.; de Faria, M. S. G. Vivianite and Siderite in Lateritic Iron Crust: An Example of Bioreduction. *Quim. Nova* **2007**, *30*, 36-40.

[42] Li, R. Z.; Wang, Y. M.; Zhou, C.; Wang, C.; Ba, X.; Li, Y. Y.; Huang, X. T.; Liu, J. P. Carbon-Stabilized High-Capacity Ferroferric Oxide Nanorod Array for Flexible Solid-State Alkaline Battery-Supercapacitor Hybrid Device with High Environmental Suitability. *Adv. Funct. Mater.* **2015**, *25*, 5384-5394.

[43] Kao, C. Y.; Tsai, Y. R.; Chou, K. S. Synthesis and Characterization of the Iron/Copper Composite as an Electrode Material for the Rechargeable Alkaline Battery. *J. Power Sources* **2011**, *196*, 5746-5750.

[44] Huang, K. C.; Chou, K. S. Microstructure Changes to Iron Nanoparticles During Discharge/Charge Cycles. *Electrochem. Commun.* **2007**, *9*, 1907-1912.

[45] Kao, C. Y.; Chou, K. S. Iron/Carbon-Black Composite Nanoparticles as an Iron Electrode Material in a Paste Type Rechargeable Alkaline Battery. *J. Power Sources* **2010**, *195*, 2399-2404.

[46] Manohar, A. K.; Yang, C. G.; Malkhandi, S.; Yang, B.; Prakash, G. K. S.; Narayanan, S. R. Understanding the Factors Affecting the Formation of Carbonyl Iron Electrodes in Rechargeable Alkaline Iron Batteries. *J. Electrochem. Soc.* **2012**, *159*, A2148-A2155.

[47] Micka, K.; Zabransky, Z. Study of Iron-Oxide Electrodes in an Alkaline Electrolyte. *J. Power Sources* **1987**, *19*, 315-323.

[48] Armstrong, R. D.; Baurhoo, I. Dissolution of Iron in Concentrated Alkali. *J. Electroanal. Chem.* **1972**, *40*, 325-338.

[49] Vijayamohanan, K.; Shukla, A. K.; Sathyanarayana, S. Kinetics of Electrode-Reactions Occurring on Porous Iron Electrodes in Alkaline Media. *J. Electroanal. Chem.* **1990**, *295*, 59-70.

[50] Vijayamohanan, K.; Shukla, A. K.; Sathyanarayana, S. Formation Mechanism of Porous Alkaline Iron Electrodes. *J. Power Sources* **1990**, *32*, 329-339.

[51] Vijayamohanan, K.; Shukla, A. K.; Sathyanarayana, S. Role of Sulfide Additives on the Performance of Alkaline Iron Electrodes. *J. Electroanal. Chem.* **1990**, *289*, 55-68.

[52] Balasubramanian, T. S.; Shukla, A. K. Effect of Metal-Sulfide Additives on Charge Discharge Reactions of the Alkaline Iron Electrode. *J. Power Sources* **1993**, *41*, 99-105.

[53] Caldas, C. A.; Lopes, M. C.; Carlos, I. A. The Role of FeS and $(NH_4)_2CO_3$ Additives on the Pressed Type Fe Electrode. *J. Power Sources* **1998**, *74*, 108-112.

[54] Posada, J. O. G.; Hall, P. J. Towards the Development of Safe and Commercially Viable Nickel-Iron Batteries: Improvements to Coulombic Efficiency at High Iron Sulphide Electrode Formulations. *J. Appl. Electrochem.* **2016**, *46*, 451-458.

[55] Manohar, A. K.; Yang, C. G.; Malkhandi, S.; Prakash, G. K. S.; Narayanan, S. R. Enhancing the Performance of the Rechargeable Iron Electrode in Alkaline Batteries with Bismuth Oxide and Iron Sulfide Additives. *J. Electrochem. Soc.* **2013**, *160*, A2078-A2084.

[56] Manohar, A. K.; Yang, C. G.; Narayanan, S. R. The Role of Sulfide Additives in Achieving Long Cycle Life Rechargeable Iron Electrodes in Alkaline Batteries. *J. Electrochem. Soc.* **2015**, *162*, A1864-A1872.

[57] Posada, J. O. G.; Abdalla, A. H.; Oseghale, C. I.; Hall, P. J. Multiple Regression Analysis in the Development of NiFe Cells as Energy Storage Solutions for Intermittent Power Sources Such as Wind or Solar. *Int. J. Hydrogen Energy* **2016**, *41*, 16330-16337.

[58] Posada, J. O. G.; Hall, P. J. Post-Hoc Comparisons among Iron Electrode Formulations Based on Bismuth, Bismuth Sulphide, Iron Sulphide, and Potassium Sulphide under Strong Alkaline Conditions. *J. Power Sources* **2014**, *268*, 810-815.

[59] Posada, J. O. G.; Hall, P. J. Multivariate Investigation of Parameters in the Development and Improvement of NiFe Cells. *J. Power Sources* **2014**, *262*, 263-269.

[60] Posada, J. O. G.; Hall, P. J. The Effect of Electrolyte Additives on the Performance of Iron Based Anodes for NiFe Cells. *J. Electrochem. Soc.* **2015**, *162*, A2036-A2043.

[61] Malkhandi, S.; Yang, B.; Manohar, A. K.; Prakash, G. K. S.; Narayanan, S. R. Self-Assembled Monolayers of N-Alkanethiols Suppress Hydrogen Evolution and

Increase the Efficiency of Rechargeable Iron Battery Electrodes. *J. Am. Chem. Soc.* **2013**, *135*, 347-353.

[62] Hang, B. T.; Watanabe, T.; Egashira, M.; Watanabe, I.; Shigeto, O.; Yamaki, J. The Effect of Additives on the Electrochemical Properties of Fe/C Composite for Fe/Air Battery Anode. *J. Power Sources* **2006**, *155*, 461-469.

[63] Kitamura, H.; Zhao, L. W.; Hang, B. T.; Okada, S.; Yamaki, J. Effect of Charge Current Density on Electrochemical Performance of Fe/C Electrodes in Alkaline Solutions. *J. Electrochem. Soc.* **2012**, *159*, A720-A724.

[64] Hang, B. T.; Thang, D. H.; Kobayashi, E. Fe/Carbon Nanofiber Composite Materials for Fe-Air Battery Anodes. *J. Electroanal. Chem.* **2013**, *704*, 145-152.

[65] Hang, B. T.; Yoon, S. H.; Okada, S.; Yamaki, J. Effect of Metal-Sulfide Additives on Electrochemical Properties of Nano-Sized Fe_2O_3-Loaded Carbon for Fe/Air Battery Anodes. *J. Power Sources* **2007**, *168*, 522-532.

[66] Cerny, J.; Micka, K. Voltammetric Study of an Iron Electrode in Alkaline Electrolytes. *J. Power Sources* **1989**, *25*, 111-122.

[67] El Haleem, S. M. A.; El Aal, E. E. A. Effect of Sulphide Ions on Corrosion Behaviour of Iron in Alkaline Solutions. *Corros. Eng., Sci. Technol.* **2008**, *43*, 225-230.

[68] Bockris, J. O. Modern Aspects of Electrode Kinetics. *Annu. Rev. Phys. Chem.* **1954**, *5*, 477-500.

[69] Trasatti, S. Work Function, Electronegativity, and Electrochemical Behavior of Metals: III. Electrolytic Hydrogen Evolution in Acid Solutions. *J. Electroanal. Chem.* **1972**, *39*, 163-&.

[70] Wang, H. L.; Liang, Y. Y.; Gong, M.; Li, Y. G.; Chang, W.; Mefford, T.; Zhou, J. G.; Wang, J.; Regier, T.; Wei, F.; Dai, H. J. An Ultrafast Nickel-Iron Battery from Strongly Coupled Inorganic Nanoparticle/Nanocarbon Hybrid Materials. *Nat. Commun.* **2012**, *3*, 1-8.

[71] Wu, X.; Wu, H. B.; Xiong, W.; Le, Z.; Sun, F.; Liu, F.; Chen, J.; Zhu, Z.; Lu, Y. Robust Iron Nanoparticles with Graphitic Shells for High-Performance Ni-Fe Battery. *Nano Energy* **2016**, *30*, 217-224.

[72] Giles, R. D.; Hampson, N. A.; Marshall, A.; Latham, R. J. Electrode Impedance of Iron in a Borate Buffer Solution. *J. Electroanal. Chem.* **1973**, *47*, 535-538.

[73] Hampson, N. A.; Latham, R. J.; Marshall, A.; Giles, R. D. Some Aspects of Electrochemical Behavior of Iron Electrode in Alkaline-Solutions. *Electrochim. Acta* **1974**, *19*, 397-401.

[74] Hills, S. Beneficial Effect of Lithiated Electrolyte on Iron Battery Electrodes. *J. Electrochem. Soc.* **1965**, *112*, 1048-1049.

[75] Guzman, R. S. S.; Vilche, J. R.; Arvia, A. J. The Voltammetric Detection of Intermediate Electrochemical Processes Related to Iron in Alkaline Aqueous-Solutions. *J. Appl. Electrochem.* **1981**, *11*, 551-562.

[76] Chernyshova, I. V.; Hochella, M. F.; Madden, A. S. Size-Dependent Structural Transformations of Hematite Nanoparticles. 1. Phase Transition. *Phys. Chem. Chem. Phys.* **2007**, *9*, 1736-1750.

[77] Vereda, F.; de Vicente, J.; Morales, M. D. P.; Rull, F.; Hidalgo-Alvarez, R. Synthesis and Characterization of Single-Domain Monocrystalline Magnetite Particles by Oxidative Aging of $Fe(OH)_2$. *J. Phys. Chem. C* **2008**, *112*, 5843-5849.

[78] Hanesch, M. Raman Spectroscopy of Iron Oxides and (Oxy)hydroxides at Low Laser Power and Possible Applications in Environmental Magnetic Studies. *Geophys. J. Int.* **2009**, *177*, 941-948.

[79] Jubb, A. M.; Allen, H. C. Vibrational Spectroscopic Characterization of Hematite, Maghemite, and Magnetite Thin Films Produced by Vapor Deposition. *ACS Appl. Mater. Interfaces* **2010**, *2*, 2804-2812.

[80] Griffete, N.; Lamouri, A.; Herbst, F.; Felidj, N.; Ammar, S.; Mangeney, C. Synthesis of Highly Soluble Polymer-Coated Magnetic Nanoparticles Using a Combination of Diazonium Salt Chemistry and the Iniferter Method. *RSC Adv.* **2012**, *2*, 826-830.

[81] El Hajj, H.; Abdelouas, A.; El Mendili, Y.; Karakurt, G.; Grambow, B.; Martin, C. Corrosion of Carbon Steel under Sequential Aerobic-Anaerobic Environmental Conditions. *Corros. Sci.* **2013**, *76*, 432-440.

[82] Dar, M. I.; Shivashankar, S. A. Single Crystalline Magnetite, Maghemite, and Hematite Nanoparticles with Rich Coercivity. *RSC Adv.* **2014**, *4*, 4105-4113.

[83] Leon, Y.; Saheb, M.; Drouet, E.; Neff, D.; Foy, E.; Leroy, E.; Dynes, J. J.; Dillmann, P. Interfacial Layer on Archaeological Mild Steel Corroded in Carbonated Anoxic Environments Studied with Coupled Micro and Nano Probes. *Corros. Sci.* **2014**, *88*, 23-35.

[84] Drozdov, A. S.; Ivanovski, V.; Avnir, D.; Vinogradov, V. V. A Universal Magnetic Ferrofluid: Nanomagnetite Stable Hydrosol with No Added Dispersants and at Neutral pH. *J. Colloid Interface Sci.* **2016**, *468*, 307-312.

[85] Ammar, I. A. Prediction of Pathways for Dissolution of Iron. *Corros. Sci.* **1977**, *17*, 583-591.

[86] Domingo, C.; Rodriguez-Clemente, R.; Blesa, M. A. Kinetics of Oxidative Precipitation of Iron-Oxide Particles. *Colloids Surf., A* **1993**, *79*, 177-189.

[87] Stagi, L.; De Toro, J. A.; Ardu, A.; Cannas, C.; Casu, A.; Lee, S. S.; Ricci, P. C. Surface Effects under Visible Irradiation and Heat Treatment on the Phase Stability of γ-Fe_2O_3 Nanoparticles and γ-Fe_2O_3-SiO_2 Core-Shell Nanostructures. *J. Phys. Chem. C* **2014**, *118*, 2857-2866.

[88] Grau-Crespo, R.; Al-Baitai, A. Y.; Saadoune, I.; De Leeuw, N. H. Vacancy Ordering and Electronic Structure of γ-Fe_2O_3 (Maghemite): A Theoretical Investigation. *J. Phys.: Condens. Matter* **2010**, *22*, 255401.

[89] Wu, W.; Xiao, X. H.; Zhang, S. F.; Li, H.; Zhou, X. D.; Jiang, C. Z. One-Pot Reaction and Subsequent Annealing to Synthesis Hollow Spherical Magnetite and Maghemite Nanocages. *Nanoscale Res. Lett.* **2009**, *4*, 926-931.

[90] Yuan, S. M.; Zhou, Z.; Li, G. Structural Evolution from Mesoporous α-Fe_2O_3 to Fe_3O_4@C and γ-Fe_2O_3 Nanospheres and Their Lithium Storage Performances. *CrystEngComm* **2011**, *13*, 4709-4713.

[91] Zhang, X.; Niu, Y. G.; Meng, X. D.; Li, Y.; Zhao, J. P. Structural Evolution and Characteristics of the Phase Transformations between α-Fe_2O_3, Fe_3O_4 and γ-Fe_2O_3 Nanoparticles under Reducing and Oxidizing Atmospheres. *CrystEngComm* **2013**, *15*, 8166-8172.

[92] Wang, L.; Shi, Y. T.; Zhang, H.; Bai, X. G.; Wang, Y. X.; Ma, T. L. Iron Oxide Nanostructures as Highly Efficient Heterogeneous Catalysts for Mesoscopic Photovoltaics. *J. Mater. Chem. A* **2014**, *2*, 15279-15283.

[93] Kumar, H.; Shukla, A. K. Fabrication Fe/Fe_3O_4/Graphene Nanocomposite Electrode Material for Rechargeable Ni/Fe Batteries in Hybrid Electric Vehicles. *Int. Lett. Chem., Phys. Astron.* **2013**, *19*, 15-25.

[94] Sugimoto, T.; Matijevic, E. Formation of Uniform Spherical Magnetite Particles by Crystallization from Ferrous Hydroxide Gels. *J. Colloid Interface Sci.* **1980**, *74*, 227-243.

[95] Nikumbh, A. K.; Sayanekar, P. L.; Chaskar, M. G. Magnetic and Electrical-Properties of γ-Fe_2O_3 Prepared from Ferrous Malonate Dihydrate. *J. Magn. Magn. Mater.* **1991**, *97*, 119-125.

[96] Venkataraman, A. Some Electrical and Magnetic-Properties of γ-Fe_2O_3. *Bull. Mater. Sci.* **1993**, *16*, 51-54.

[97] Imada, M.; Fujimori, A.; Tokura, Y. Metal-Insulator Transitions. *Rev. Mod. Phys.* **1998**, *70*, 1039-1263.

[98] Draine, B. T.; Hensley, B. Magnetic Nanoparticles in the Interstellar Medium: Emission Spectrum and Polarization. *Astrophys. J.* **2013**, *765*, 159.